

2010

Assessment of Benthic Flux of Dissolved Organic Carbon in Estuaries Using the Eddy Correlation Technique

Michael P. Swett

University of Maine - Main

Follow this and additional works at: <http://digitalcommons.library.umaine.edu/etd>



Part of the [Environmental Engineering Commons](#)

Recommended Citation

Swett, Michael P, "Assessment of Benthic Flux of Dissolved Organic Carbon in Estuaries Using the Eddy Correlation Technique" (2010). *Electronic Theses and Dissertations*. 13.
<http://digitalcommons.library.umaine.edu/etd/13>

This Open-Access Thesis is brought to you for free and open access by DigitalCommons@UMaine. It has been accepted for inclusion in Electronic Theses and Dissertations by an authorized administrator of DigitalCommons@UMaine.

**ASSESSMENT OF BENTHIC FLUX OF DISSOLVED ORGANIC CARBON IN
ESTUARIES USING THE EDDY CORRELATION TECHNIQUE**

By

Michael P. Swett

B.S. University of Maine, 2008

A THESIS

Submitted in Partial Fulfillment of the

Requirements for the Degree of

Master of Science

(in Civil Engineering)

The Graduate School

The University of Maine

May, 2010

Advisory Committee:

Aria Amirbahman, Professor of Civil & Environmental Engineering, Advisor

Emmanuel Boss, Professor of Oceanography

Tsutomu Ohno, Professor of Soil Chemistry

THESIS
ACCEPTANCE STATEMENT

On behalf of the Graduate Committee for Michael P. Swett, I affirm that this manuscript is the final and accepted thesis. Signatures of all committee members are on file with the Graduate School at the University of Maine, 42 Stodder Hall, Orono, Maine.

Dr. Aria Amirbahman,
Professor of Civil & Environmental Engineering

Committee chair's signature, name, and title

(Date)

LIBRARY RIGHTS STATEMENT

In presenting this thesis in partial fulfillment of the requirements for an advanced degree at The University of Maine, I agree that the Library shall make it freely available for inspection. I further agree that permission for “fair use” copying of this thesis for scholarly purposes may be granted by the Librarian. It is understood that any copying or publication of this thesis for financial gain shall not be allowed without my written permission.

Signature:

Date:

**ASSESSMENT OF BENTHIC FLUX OF DISSOLVED ORGANIC CARBON IN
ESTUARIES USING THE EDDY-CORRELATION TECHNIQUE**

By: Michael P. Swett

Thesis Advisor: Dr. Aria Amirbahman

An Abstract of the Thesis Presented
in Partial Fulfillment of the Requirements for the
Degree of Master of Science
(in Civil Engineering)
May, 2010

Dissolved organic carbon (DOC) is a water quality concern in estuarine environments, as DOC facilitates mobilization of metals and organics in sediments and leads to toxic disinfection byproducts during water treatment. Export of DOC from sediments can vary with changing environmental conditions, including wetland restoration and rising sea levels. Therefore, it is important to quantify flux of DOC across the sediment-water interface (SWI). Existing DOC flux measurement techniques, such as equilibrium dialysis, porewater extraction, and benthic chamber measurement, are intrusive to the sediment environment and underestimate flux by only capturing certain flux contributions.

In this research, methods for estimating benthic DOC flux using the eddy correlation technique (also known as the eddy covariance technique) were developed and implemented at three estuarine mudflats and one freshwater wetland throughout Maine and New Hampshire. The eddy correlation technique, first developed for use in

atmospheric sciences and later applied to aquatic O₂ and groundwater flux measurement, is a non-intrusive, *in situ* method based on measurement of turbulent fluctuations of properties such as fluid velocity, solute concentration, and temperature. The methods employed here utilized vertical velocity vectors obtained with an acoustic Doppler velocimeter (ADV) and DOC concentrations approximated with a chromophoric dissolved organic matter (CDOM) fluorometer. Both linear regression and moving average techniques were investigated for isolation of turbulent fluctuations in the velocity and concentration data, and spectral analysis was used to analyze flux contribution in the frequency series.

DOC flux values obtained using eddy correlation were compared with results from porewater extraction. Eddy flux values were typically an order of magnitude higher than the diffusive fluxes calculated from porewater gradients, which are thought to underestimate flux, as turbulent eddy diffusion dominates vertical transport in these aquatic systems. Reasonable flux estimates are a function of adequate trend removal to separate turbulent fluctuations from mean flows and wave-induced fluctuations. This can be difficult in heterogeneous environments such as the ones studied here. In addition, spectral analysis shows that DOC flux estimates can be compromised by high-frequency noise caused by particle attenuation of the CDOM fluorometer measurements.

ACKNOWLEDGEMENTS

I have many people to thank for their assistance on my research project. Jim Loftin and Wayne Slade of the Oceanography Department provided equipment expertise and software support. Tim Ellis, a private landowner, helped us access his land many times for instrument deployment. Lauren Brown, a fellow graduate student, allowed me to get my feet wet (both literally and figuratively!) on her project, which provided me with excellent experience that I could then apply to my own research. Greg Gerbi of the Institute of Marine & Coastal Sciences at Rutgers University provided knowledgeable insight on modeling and data analysis. John Peckenham and Clive Devoy loaned equipment, and Tiffany Wilson was very helpful in the lab.

I am grateful to Eric Landis and the Civil & Environmental Engineering Department, as well as the Graduate School for providing me with Teaching Assistant positions, which allowed me to continue my research after project funding was cut due to the trying economic times. Summer 2009 funding for this project was provided by the Maine Sea Grant, #NA06OAR4170108. I would also like to thank NortekUSA for providing funding for me to present a portion of this research at the 2009 American Geophysical Union Fall Meeting in San Francisco.

Many thanks to the faculty, staff, and fellow students in Civil Engineering and the College of Engineering, who have had a positive influence on my studies and my work for the past six years. An extra thank you to Mary Burton and Pam Oakes for all of their help along the way.

I would like to acknowledge Stom Ohno of the Soil Chemistry Department and Emmanuel Boss of the School of Marine Sciences, for serving on my thesis committee. Emmanuel was also very helpful throughout the project, offering data analysis assistance and recommendations. I would like to thank my committee chair and advisor, Aria Amirbahman, Professor of Civil Engineering. Throughout this project, his office door was always open, and he was always willing to hear my ideas and offer advice. Additionally, I don't think it is every advisor who will tromp around in the mud and labor through field work right along with his students.

Lastly, I would like to thank my parents, Paul and Nancy Swett, and my sister, Lauren Swett, for their endless support of me in all of my endeavors.

TABLE OF CONTENTS

ACKNOWLEDGEMENTS	iii
LIST OF TABLES	viii
LIST OF FIGURES	ix
CHAPTER	
1. INTRODUCTION	1
2. BACKGROUND	3
2.1 DOC production and benthic flux measurement.....	3
2.1.1. Peepers.....	5
2.1.2. Porewater extraction	6
2.1.3. Benthic chambers	8
2.2. Eddy correlation.....	11
2.2.1. Eddy correlation in atmospheric sciences	12
2.2.2. Eddy correlation in aquatic environments.....	14
3. MATERIALS AND METHODS.....	23
3.1. Acoustic Doppler velocimeter.....	23
3.2. Fluorometer	24
3.3. Deployment setup.....	27
3.4. Project sites	29
3.4.1. Frankfort Flats	29
3.4.2. Squamscott River.....	31

3.4.3. Piscataqua River	33
3.4.4. Burton Bog	35
3.5. Data Analysis	36
3.5.1. Velocity vector rotation.....	37
3.5.2. Averaging window selection	38
3.5.3. Trend removal.....	39
3.5.4. Flux calculation	40
3.5.5. Spectral analysis	41
4. RESULTS AND DISCUSSION.....	42
4.1. Data processing	42
4.1.1. DOC concentration	42
4.1.2. Velocity vectors.....	43
4.2. Data selection	44
4.3. Averaging windows.....	46
4.4. Flux calculation	48
4.5. Spectral analysis.....	59
5. SUMMARY AND CONCLUSIONS	70
REFERENCES	73
APPENDICES	78
Appendix A: MATLAB code.....	79
Appendix B: Water depth, DOC concentration, and velocity data	83
Appendix C: CDOM calibration points	91
Appendix D: Correlation coefficient vs. filter length	92

Appendix E: Velocity and concentration with trends	95
Appendix F: Noise distributions	131
Appendix G: Normalized cumulative cospectra of fluctuations of vertical velocity and concentration at 1 Hz	134
BIOGRAPHY OF THE AUTHOR.....	150

LIST OF TABLES

Table 2.1.	Summary of eddy correlation studies and deployment characteristics for measurement of benthic flux.....	15
Table 3.1.	Porewater profile data obtained from sediment cores collected at Squamscott River mudflat.....	32
Table 3.2.	Porewater profile data obtained from sediment cores collected at Kittery mudflat.....	34
Table 4.1.	Correlation of C with uncorrected and corrected w	43
Table 4.2.	Bursts of data selected for flux analysis.....	44
Table 4.3.	Optimum averaging window lengths and resulting number of blocks for each burst.....	48
Table 4.4.	Average daily DOC flux estimates determined using eddy correlation.....	54
Table 4.5.	Values of average daily flux calculated from data at original sampling frequency and lower frequencies.....	65

LIST OF FIGURES

Figure 2.1.	Comparison of O ₂ flux.....	17
Figure 2.2.	Example of cumulative spectra.....	18
Figure 2.3.	Plots illustrating the relation between turbulent velocities and O ₂ flux.....	21
Figure 2.4.	Example cospectrum and comparison of O ₂ flux.....	22
Figure 3.1.	Vector acoustic Doppler velocimeter held in bracket.....	24
Figure 3.2.	ECO-FL CDOM fluorometer mounted on bracket at 45°.....	25
Figure 3.3.	CDOM fluorometer calibration curve.....	27
Figure 3.4.	Instrument setup in laboratory and deployed in field.....	28
Figure 3.5.	Frankfort Flats deployment site.....	30
Figure 3.6.	Squamscott River deployment site.....	32
Figure 3.7.	Kittery deployment site.....	34
Figure 3.8.	Burton Bog deployment site.....	36
Figure 4.1.	Typical plots of filter length vs. correlation.....	47
Figure 4.2.	Plots of cumulative flux for Frankfort burst 1.....	49
Figure 4.3.	Plots of cumulative flux for Frankfort burst 2.....	50
Figure 4.4.	Plots of cumulative flux for Squamscott burst.....	51
Figure 4.5.	Plots of cumulative flux for Kittery flow period burs.....	52
Figure 4.6.	Plots of cumulative flux for Kittery ebb period burst.....	53
Figure 4.7.	Sediment cores collected in Kittery.....	55

Figure 4.8.	Cumulative flux for Kittery flow period burst calculated using linear regression.....	56
Figure 4.9.	Typical distribution of high-frequency noise and Gaussian fit.....	58
Figure 4.10.	Typical normalized cumulative cospectrum.....	60
Figure 4.11.	Typical spectra for C' and w'	61
Figure 4.12.	Power spectral density of w and power cospectral density of w and C	63
Figure 4.13.	Smoothed power spectral density of w and normalized cumulative cospectrum of w and C	64
Figure 4.14	Plot of cumulative flux for Frankfort burst 1 at 1 Hz calculated using linear regression.....	67
Figure 4.15	Plot of cumulative flux for Frankfort burst 2 at 1 Hz calculated using linear regression.....	67
Figure 4.16	Plot of cumulative flux for Squamscott burst at 1 Hz calculated using linear regression.....	68
Figure 4.17	Plot of cumulative flux for Kittery flow period burst at 1 Hz calculated using linear regression.....	68
Figure 4.18	Plot of cumulative flux for Kittery ebb period burst at 1 Hz calculated using linear regression.....	69
Figure B.1.	Water depth over time for entire Frankfort deployment.....	83
Figure B.2.	DOC concentration over time for entire Frankfort deployment.....	83
Figure B.3.	Vertical velocity over time for entire Frankfort deployment.....	84

Figure B.4.	Absolute horizontal velocity over time for entire Frankfort deployment.....	84
Figure B.5.	Water depth over time for entire Squamscott deployment.....	85
Figure B.6.	DOC concentration over time for entire Squamscott deployment.....	85
Figure B.7.	Vertical velocity over time for entire Squamscott deployment.....	86
Figure B.8.	Absolute horizontal velocity over time for entire Squamscott deployment.....	86
Figure B.9.	Water depth over time for entire Kittery deployment.....	87
Figure B.10.	DOC concentration over time for entire Kittery deployment.....	87
Figure B.11.	Vertical velocity over time for entire Kittery deployment.....	88
Figure B.12.	Absolute horizontal velocity over time for entire Kittery deployment.....	88
Figure B.13.	DOC concentration over time for entire Burton Bog deployment.....	89
Figure B.14.	Vertical velocity over time for entire Burton Bog deployment.....	90
Figure B.15.	Absolute horizontal velocity over time for entire Burton Bog deployment.....	90
Figure C.1.	All points obtained in laboratory DOC calibration of ECO-FL.....	91
Figure D.1.	Correlation coefficient vs. filter length for Frankfort burst 1, shown with optimum averaging window.....	92
Figure D.2.	Correlation coefficient vs. filter length for Frankfort burst 2, shown with optimum averaging window.....	92

Figure D.3.	Correlation coefficient vs. filter length for Squamscott burst, shown with optimum averaging window.....	93
Figure D.4.	Correlation coefficient vs. filter length for Kittery tidal ebb burst, shown with optimum averaging window.....	93
Figure D.5.	Correlation coefficient vs. filter length for Kittery tidal flow burst, shown with optimum averaging window.....	94
Figure D.6.	Second derivative of Fig. D.4 showing initial inflection point.....	94
Figure E.1.	Vertical velocity and corresponding linear trend for Frankfort burst 1, block 77300-78100.....	95
Figure E.2.	DOC concentration and corresponding linear trend for Frankfort burst 1, block 77300-78100.....	95
Figure E.3.	Vertical velocity and corresponding linear trend for Frankfort burst 1, block 78100-78900.....	96
Figure E.4.	DOC concentration and corresponding linear trend for Frankfort burst 1, block 78100-78900.....	96
Figure E.5.	Vertical velocity and corresponding linear trend for Frankfort burst 1, block 78900-79700.....	97
Figure E.6.	DOC concentration and corresponding linear trend for Frankfort burst 1, block 78900-79700.....	97
Figure E.7.	Vertical velocity and corresponding linear trend for Frankfort burst 1, block 79700-80500.....	98
Figure E.8.	DOC concentration and corresponding linear trend for Frankfort burst 1, block 79700-80500.....	98

Figure E.9.	Vertical velocity and corresponding linear trend for Frankfort burst 1, block 80500-81300.....	99
Figure E.10.	DOC concentration and corresponding linear trend for Frankfort burst 1, block 80500-81300.....	99
Figure E.11.	Vertical velocity and corresponding moving average trend for Frankfort burst 1.....	100
Figure E.12.	DOC concentration and corresponding moving average trend for Frankfort burst 1.....	100
Figure E.13.	Vertical velocity and corresponding linear trend for Frankfort burst 2, block 88828-90484.....	101
Figure E.14.	DOC concentration and corresponding linear trend for Frankfort burst 2, block 88828-90484.....	101
Figure E.15.	Vertical velocity and corresponding moving average trend for Frankfort burst 2.....	102
Figure E.16.	DOC concentration and corresponding moving average trend for Frankfort burst 2.....	102
Figure E.17.	Vertical velocity and corresponding linear trend for Squamscott burst, block 103680-105040.....	103
Figure E.18.	DOC concentration and corresponding linear trend for Squamscott burst, block 103680-105040.....	103
Figure E.19.	Vertical velocity and corresponding linear trend for Squamscott burst, block 105040-106400.....	104

Figure E.20.	DOC concentration and corresponding linear trend for Squamscott burst, block 105040-106400.....	104
Figure E.21.	Vertical velocity and corresponding moving average trend for Squamscott burst.....	105
Figure E.22.	DOC concentration and corresponding moving average trend for Squamscott burst.....	105
Figure E.23.	Vertical velocity and corresponding linear trend for Kittery tidal flow burst, block 9396-10788.....	106
Figure E.24.	DOC concentration and corresponding linear trend for Kittery tidal flow burst, block 9396-10788.....	106
Figure E.25.	Vertical velocity and corresponding linear trend for Kittery tidal flow burst, block 10788-12180.....	107
Figure E.26.	DOC concentration and corresponding linear trend for Kittery tidal flow burst, block 10788-12180.....	107
Figure E.27.	Vertical velocity and corresponding linear trend for Kittery tidal flow burst, block 12180-13572.....	108
Figure E.28.	DOC concentration and corresponding linear trend for Kittery tidal flow burst, block 12180-13572.....	108
Figure E.29.	Vertical velocity and corresponding linear trend for Kittery tidal flow burst, block 13572-14964.....	109
Figure E.30.	DOC concentration and corresponding linear trend for Kittery tidal flow burst, block 13572-14964.....	109

Figure E.31.	Vertical velocity and corresponding linear trend for Kittery tidal flow burst, block 14964-16356.....	110
Figure E.32.	DOC concentration and corresponding linear trend for Kittery tidal flow burst, block 14964-16356.....	110
Figure E.33.	Vertical velocity and corresponding linear trend for Kittery tidal flow burst, block 16356-17748.....	111
Figure E.34.	DOC concentration and corresponding linear trend for Kittery tidal flow burst, block 16356-17748.....	111
Figure E.35.	Vertical velocity and corresponding linear trend for Kittery tidal flow burst, block 17748-19140.....	112
Figure E.36.	DOC concentration and corresponding linear trend for Kittery tidal flow burst, block 17748-19140.....	112
Figure E.37.	Vertical velocity and corresponding linear trend for Kittery tidal flow burst, block 19140-20532.....	113
Figure E.38.	DOC concentration and corresponding linear trend for Kittery tidal flow burst, block 19140-20532.....	113
Figure E.39.	Vertical velocity and corresponding linear trend for Kittery tidal flow burst, block 20532-21924.....	114
Figure E.40.	DOC concentration and corresponding linear trend for Kittery tidal flow burst, block 20532-21924.....	114
Figure E.41.	Vertical velocity and corresponding linear trend for Kittery tidal flow burst, block 21924-23316.....	115

Figure E.42.	DOC concentration and corresponding linear trend for Kittery tidal flow burst, block 21924-23316.....	115
Figure E.43.	Vertical velocity and corresponding linear trend for Kittery tidal flow burst, block 23316-24708.....	116
Figure E.44.	DOC concentration and corresponding linear trend for Kittery tidal flow burst, block 23316-24708.....	116
Figure E.45.	Vertical velocity and corresponding linear trend for Kittery tidal flow burst, block 24708-26100.....	117
Figure E.46.	DOC concentration and corresponding linear trend for Kittery tidal flow burst, block 24708-26100.....	117
Figure E.47.	Vertical velocity and corresponding linear trend for Kittery tidal flow burst, block 26100-27492.....	118
Figure E.48.	DOC concentration and corresponding linear trend for Kittery tidal flow burst, block 26100-27492.....	118
Figure E.49.	Vertical velocity and corresponding linear trend for Kittery tidal flow burst, block 27492-28884.....	119
Figure E.50.	DOC concentration and corresponding linear trend for Kittery tidal flow burst, block 27492-28884.....	119
Figure E.51.	Vertical velocity and corresponding linear trend for Kittery tidal flow burst, block 28884-30276.....	120
Figure E.52.	DOC concentration and corresponding linear trend for Kittery tidal flow burst, block 28884-30276.....	120

Figure E.53.	Vertical velocity and corresponding linear trend for Kittery tidal flow burst, block 30276-31668.....	121
Figure E.54.	DOC concentration and corresponding linear trend for Kittery tidal flow burst, block 30276-31668.....	121
Figure E.55.	Vertical velocity and corresponding linear trend for Kittery tidal flow burst, block 31688-33060.....	122
Figure E.56.	DOC concentration and corresponding linear trend for Kittery tidal flow burst, block 31688-33060.....	122
Figure E.57.	Vertical velocity and corresponding linear trend for Kittery tidal flow burst, block 33060-34452.....	123
Figure E.58.	DOC concentration and corresponding linear trend for Kittery tidal flow burst, block 33060-34452.....	123
Figure E.59.	Vertical velocity and corresponding linear trend for Kittery tidal flow burst, block 34452-35844.....	124
Figure E.60.	DOC concentration and corresponding linear trend for Kittery tidal flow burst, block 34452-35844.....	124
Figure E.61.	Vertical velocity and corresponding moving average trend for Kittery tidal flow burst.....	125
Figure E.62.	DOC concentration and corresponding moving average trend for Kittery tidal flow burst.....	125
Figure E.63.	Vertical velocity and corresponding linear trend for Kittery tidal ebb burst, block 128348-131044.....	126

Figure E.64.	DOC concentration and corresponding linear trend for Kittery tidal ebb burst, block 128348-131044.....	126
Figure E.65.	Vertical velocity and corresponding linear trend for Kittery tidal ebb burst, block 131044-133740.....	127
Figure E.66.	DOC concentration and corresponding linear trend for Kittery tidal ebb burst, block 131044-133740.....	127
Figure E.67.	Vertical velocity and corresponding linear trend for Kittery tidal ebb burst, block 133740-136436.....	128
Figure E.68.	DOC concentration and corresponding linear trend for Kittery tidal ebb burst, block 133740-136436.....	128
Figure E.69.	Vertical velocity and corresponding linear trend for Kittery tidal ebb burst, block 136436-139132.....	129
Figure E.70.	DOC concentration and corresponding linear trend for Kittery tidal ebb burst, block 136436-139132.....	129
Figure E.71.	Vertical velocity and corresponding moving average trend for Kittery tidal ebb burst.....	130
Figure E.72.	DOC concentration and corresponding moving average trend for Kittery tidal ebb burst.....	130
Figure F.1.	Frankfort burst 1 noise distributions.....	131
Figure F.2.	Frankfort burst 2 noise distributions.....	131
Figure F.3.	Squamscott burst noise distributions.....	132
Figure F.4.	Kittery tidal flow period noise distributions.....	133
Figure F.5.	Kittery tidal ebb period noise distributions.....	133

Figure G.1.	Normalized cumulative cospectrum of w' and C' for Frankfort burst 1, block 77300-78100.....	134
Figure G.2.	Normalized cumulative cospectrum of w' and C' for Frankfort burst 1, block 78100-78900.....	135
Figure G.3.	Normalized cumulative cospectrum of w' and C' for Frankfort burst 1, block 78900-79700.....	135
Figure G.4.	Normalized cumulative cospectrum of w' and C' for Frankfort burst 1, block 79700-80500.....	136
Figure G.5.	Normalized cumulative cospectrum of w' and C' for Frankfort burst 1, block 80500-81300.....	136
Figure G.6.	Normalized cumulative cospectrum of w' and C' for Frankfort burst 2, block 88828-90484.....	137
Figure G.7.	Normalized cumulative cospectrum of w' and C' for Squamscott burst, block 103680-105040.....	137
Figure G.8.	Normalized cumulative cospectrum of w' and C' for Squamscott burst, block 105040-106400.....	138
Figure G.9.	Normalized cumulative cospectrum of w' and C' for Kittery tidal flow burst, block 9396-10788.....	138
Figure G.10.	Normalized cumulative cospectrum of w' and C' for Kittery tidal flow burst, block 10788-12180.....	139
Figure G.11.	Normalized cumulative cospectrum of w' and C' for Kittery tidal flow burst, block 12180-13572.....	139

Figure G.12.	Normalized cumulative cospectrum of w' and C' for Kittery tidal flow burst, block 13572-14964.....	140
Figure G.13.	Normalized cumulative cospectrum of w' and C' for Kittery tidal flow burst, block 14964-16356.....	140
Figure G.14.	Normalized cumulative cospectrum of w' and C' for Kittery tidal flow burst, block 16356-17748.....	141
Figure G.15.	Normalized cumulative cospectrum of w' and C' for Kittery tidal flow burst, block 17748-19140.....	141
Figure G.16.	Normalized cumulative cospectrum of w' and C' for Kittery tidal flow burst, block 19140-20532.....	142
Figure G.17.	Normalized cumulative cospectrum of w' and C' for Kittery tidal flow burst, block 20532-21924.....	142
Figure G.18.	Normalized cumulative cospectrum of w' and C' for Kittery tidal flow burst, block 21924-23316.....	143
Figure G.19.	Normalized cumulative cospectrum of w' and C' for Kittery tidal flow burst, block 23316-24708.....	143
Figure G.20.	Normalized cumulative cospectrum of w' and C' for Kittery tidal flow burst, block 24708-26100.....	144
Figure G.21.	Normalized cumulative cospectrum of w' and C' for Kittery tidal flow burst, block 26100-27492.....	144
Figure G.22.	Normalized cumulative cospectrum of w' and C' for Kittery tidal flow burst, block 27492-28884.....	145

Figure G.23.	Normalized cumulative cospectrum of w' and C' for Kittery tidal flow burst, block 28884-30276.....	145
Figure G.24.	Normalized cumulative cospectrum of w' and C' for Kittery tidal flow burst, block 30276-31668.....	146
Figure G.25.	Normalized cumulative cospectrum of w' and C' for Kittery tidal flow burst, block 31688-33060.....	146
Figure G.26.	Normalized cumulative cospectrum of w' and C' for Kittery tidal flow burst, block 33060-34452.....	147
Figure G.27.	Normalized cumulative cospectrum of w' and C' for Kittery tidal flow burst, block 34452-35844.....	147
Figure G.28.	Normalized cumulative cospectrum of w' and C' for Kittery tidal ebb burst, block 128348-131044.....	148
Figure G.29.	Normalized cumulative cospectrum of w' and C' for Kittery tidal ebb burst, block 131044-133740.....	148
Figure G.30.	Normalized cumulative cospectrum of w' and C' for Kittery tidal ebb burst, block 133740-136436.....	149
Figure G.31.	Normalized cumulative cospectrum of w' and C' for Kittery tidal ebb burst, block 136436-139132.....	149

Chapter 1

INTRODUCTION

Dissolved organic carbon (DOC) is a water quality concern in coastal environments, as estuarine sediments release significant amounts of DOC due to high levels of microbial activity. DOC complexes with toxic metals and organics, and flux of DOC from sediments can then transport these contaminants into the water column. In addition, DOC in source waters can lead to toxic disinfection byproducts during the drinking water treatment process. There is a potential for increases in DOC export from wetland and estuarine sediments due to wetland restoration, dam removal, and rising sea levels. These factors can facilitate exposure of sediments high in organic content to tidal flow, thus increasing DOC production. Therefore, it is essential to be able to reliably quantify DOC flux from estuarine sediments.

Various methods are currently used to measure DOC flux. Some methods, such as equilibrium dialysis and porewater extraction, rely on porewater concentration gradients to estimate solute flux. These techniques, however, only capture flux due to molecular diffusion, thus underestimating net flux. Alternatively, benthic chambers rely on temporal measurement of properties in the overlying water, but do not adequately replicate physical aquatic conditions that facilitate turbulent transport. In addition, these methods are intrusive and result in disturbance of the sediment environment.

The eddy correlation technique provides a non-invasive, *in situ* method for measuring flux and monitoring changes over time. This technique has been used in atmospheric sciences for many years and more recently has been adopted to measure

solute flux across the sediment-water interface (SWI) in aquatic systems. Eddy correlation principles involve the separation of turbulent fluctuations from mean flow. Turbulent fluctuations of velocity and those of a scalar, such as heat, O₂, or DOC concentration, can be correlated to estimate the vertical benthic flux due to turbulent eddy diffusion, which is expected to dominate vertical transport through the water column, provided that there is no significant vertical advective flow.

The research presented here illustrates the first known attempt to quantify benthic DOC flux using the eddy correlation technique. Eddy correlation instrumentation was deployed at three estuarine mudflats and one freshwater wetland in northern New England in August and September of 2009. An acoustic Doppler velocimeter (ADV), which utilizes acoustic backscattering of suspended particles as a proxy for water velocity, was used to measure three-dimensional velocity vectors. A chromophoric dissolved organic matter (CDOM) fluorometer was used to estimate DOC concentration. The data collected with these two instruments were processed and correlated to obtain estimates of vertical DOC flux across the SWI. The following report will include an outline of background theories and prior research in benthic flux measurement and eddy correlation. A comprehensive method for assessing benthic DOC flux in estuarine environments based on field studies and data analysis will be presented, and the results of this research will be discussed. Lastly, conclusions and recommendations for future work will be made.

Chapter 2

BACKGROUND

2.1 DOC production and benthic flux measurement

The benthic boundary layer is the zone of marine sediment and overlying water that is directly affected by the SWI. Carbon cycling in this boundary layer involves complex biogeochemistry. DOC in aquatic environments can originate from a variety of sources and accumulate in the benthic zone (Carlson, 2002). For instance, particulate organic carbon (POC) from plant matter, dead marine organisms, and other detritus accumulates in the sediment, and POC suspended in the water column flocculates and settles on the sediment surface (Cauwet, 2002). These organic compounds are broken down into dissolved form and then cycled by benthic macrofauna and by sediment bacteria via extracellular enzyme-mediated hydrolysis (Burdige, 2006). Another source of DOC in sediment and in the water column is cell lysis. It is estimated that as much as 26% of carbon fixed during primary production is released as marine DOC by viral lysis (Maier et al., 2009). DOC in turn can be remineralized by bacteria, or it can be consumed and transformed, resulting in lower molecular weight, more refractory forms of DOC. This leads to net accumulation of DOC in benthic sediment porewaters (Burdige, 2006).

Upon its release from porewater into the water column in estuarine environments, DOC may be consumed by prokaryotic bacterioplankton or by other marine organisms. DOC is also susceptible to abiotic removal via photoirradiation or particle sorption (Carlson, 2002). DOC flux is of concern because DOC is known to complex with metals

and other contaminants (e.g., Kalbitz et al., 1997). Therefore, DOC has the potential to transport contaminants such as mercury from the sediment into the water column. DOC also has an effect on the bioavailability of mercury, and environments with high DOC production may have increased rates of mercury methylation, leading to higher concentrations of toxic methylmercury (Benoit et al., 2003). In addition, DOC in source waters can lead to reactions during disinfection in the water treatment process, resulting in harmful disinfection byproducts, such as trihalomethanes (Fleck et al., 2007).

Total benthic flux of a solute across the SWI has been described as the sum of fluxes due to diffusion, bioturbation, bioirrigation, porewater advection, and sediment resuspension (Burdige, 2006):

$$J_{\text{tot}} = J_{\text{diff}} + J_{\text{biot}} + J_{\text{irr}} + J_{\text{adv}} + J_{\text{rsp}} \quad (2.1)$$

Since, in many sediments, porewater DOC concentrations are an order of magnitude higher than concentrations in the overlying water, the sediments can serve as a DOC source to the water column via diffusive transport (Burdige, 2006). In turbulent systems, eddy diffusion dominates molecular diffusion as the dominant transport process of solutes from the diffusive boundary layer at the SWI to the water column (Crusius et al., 2008). In order to effectively quantify vertical flux between sediment porewaters and the water column, all of the processes in Equation 2.1 should be accounted for.

Various methods exist to quantify DOC concentrations and flux across the SWI, and they capture flux components from Equation 2.1 with varying success. Multi-chambered equilibrium dialysis samplers, or “peepers,” and sediment core centrifugation can be used to measure porewater DOC concentration gradients, from which flux can be calculated. *In situ* benthic chambers are used to measure temporal release of DOC from

sediments into the overlying surface water. The following sections will provide a brief explanation of these techniques and their applications in measuring organic carbon, as well as potential shortfalls in using these methods for DOC flux measurement.

2.1.1. Peepers

Peepers can be used to measure porewater concentrations of various analytes, including DOC. The concentration gradients obtained can in turn be used to calculate flux across the SWI. First introduced by Hesslein (1976) for measurement of methane and phosphate profiles in river sediments, peepers are typically characterized by a sheet of acrylic securing a dialysis membrane over multiple DI-water- or gel-filled chamber cells hollowed out of another sheet of acrylic. The peepers are driven into sediments, where they are allowed to equilibrate with surrounding porewaters via diffusion of dissolved compounds across the permeable membrane, which occurs due to concentration gradients between the DI water and surrounding porewater.

Merritt and Amirbahman (2007, 2008) used peepers to study mercury and methylmercury dynamics in estuarine sediments at Frankfort Flats, one of the sites also investigated in the eddy correlation research presented here. DOC porewater concentrations were measured using peepers at 1.5 cm (2007) and 0.75 cm (2008) resolution, and profiles were reported. Methylmercury flux was calculated using Fick's First Law and a diffusion coefficient obtained from the literature.

There are limitations to using peepers to obtain flux. Due to long equilibration times (e.g., 30 d by Merritt and Amirbahman, 2008; 32 d by Merritt and Amirbahman, 2007; 16 d by Carignan et al., 1994), peepers cannot be used to examine short-scale

temporal variations in flux. Peepers provide only an average flux over the period of equilibration. This raises concerns about effectively capturing short-term changes in solute transport caused by bioturbation, bioirrigation, and sediment resuspension. Sediments are also subject to disturbance during peeper installation. When driven into the sediment, the peeper can carry material from the sediment surface and overlying water down through the sediment profile. The soil structure along the face of the peeper is also altered, which could result in changes in porewater diffusion characteristics. When peepers are to be deployed in anoxic sediment environments, they must be deoxygenated, and extensive care must be taken to ensure they maintain anoxia prior to deployment (Carignan, 1994). In addition, peepers are not entirely an *in situ* technique, as they must be removed from the environment for chemical analysis.

2.1.2. Porewater extraction

Porewater extraction from sediment cores via centrifugation or squeezing has been used extensively to quantify concentrations of various porewater analytes. In addition, syringe extraction can be used to obtain porewater samples directly from the sediment. The following section will briefly describe a few studies involving porewater extraction, as well as potential deficiencies to using these methods for DOC flux calculations.

Lahajnar et al. (2005) measured deep-ocean benthic DOC flux using sediment core centrifugation. Cores 10 cm in diameter were collected, extruded, and sliced into 0.5-cm or 1-cm sections. Each sediment section was centrifuged at 2000 rpm for 20 min, and the resulting porewater was filtered. Flux was calculated from DOC concentrations

using Fick's First Law. Diffusion coefficients were calculated based on DOC molecular weights from the literature. Benthic DOC flux for all study sites ranged from 47.2 to 223.9 $\mu\text{mol m}^{-2} \text{d}^{-1}$ (Lahajnar et al., 2005).

Carignan et al. (1985) used sediment core centrifugation, producing porewater profiles for comparison with peeper results. Cores 8 cm in diameter were sliced into sections 1 cm thick and centrifuged for 20 min at 5000 rpm. Resulting porewater was passed through filters corresponding with the filter pore sizes utilized in the peepers. When 0.45- μm filters were used, centrifugation produced higher concentrations of DOC than did peepers. When 0.03 μm filters were used, centrifugation and peepers produced similar DOC profiles. However, the authors noted that there is potential for contamination from sediment colloids during porewater extraction by centrifugation (Carignan et al., 1985).

Burdige and Homstead (1994) used two methods of porewater extraction from sediment cores in a Chesapeake Bay study comparing porewater gradient flux to measurements obtained using benthic chambers. In one method, 3.5-in. diameter sediment subcores obtained from a larger box core were sectioned, and porewater was removed using low-pressure sediment squeezers. In the other method, 2.25-in. diameter sediment cores were obtained using a special core tube with sampling ports that collected porewater when gas pressure was applied to the core, eliminating the need for sectioning. Porewater samples were filtered through 0.45- μm filters to remove any particulate matter. A total of seven data sets were obtained from two study sites over the course of one year. The study found that flux values calculated from porewater gradients were generally similar to values produced in a laboratory flux chamber (Burdige & Homstead, 1994).

Calculating flux from porewater gradients relies heavily on diffusion coefficients, which depend on DOC molecular weight and sediment porosity, two factors that may vary considerably with temperature, season, and from site to site and may be difficult to accurately estimate (Alperin et al., 1994). Another potential source of error in calculating flux based on porewater gradients lies in the variability of what is chosen for Δz , the change in depth over which the change in concentration occurs. Burdige (2006) describes Δz as being calculated utilizing the porewater concentration from the sample collected closest to the SWI. It is noted, however, that this may not always capture the most accurate porewater gradients. For instance, Lahajnar et al. (2005) used Δz value of 1.5 cm or 1.75 cm, but DOC concentrations were often higher in samples from closer to the SWI and decreased sharply with depth. In this study with deep-ocean sediments, the higher values at the SWI were considered to be due to extraction artifact; i.e., lysis of cell biomass during porewater DOC extraction.

2.1.3. Benthic chambers

Benthic chambers, which can be installed *in situ* or in the laboratory, involve trapping a finite volume of overlying water over a finite surface area of sediment to measure solute flux across the SWI. Benthic chambers have been described as advantageous because they measure flux due to both molecular diffusion and advection (Reimers et al., 2001). A detailed review by Tengberg et al. (1995) describes various chamber technologies. The following section briefly describes three studies involving benthic chambers. Some of the potential problems with using these systems for DOC flux measurement will also be discussed.

Burdige and Homstead (1994) used laboratory incubation chambers to quantify DOC flux for comparison with flux calculated from gradients obtained by porewater extraction, as described previously. 3.5-in diameter chamber tubes were used to collect sediment cores. Overlying water heights of 9-13 cm were maintained, and the water was mixed using a glass stirring rod. Filtered air was pumped into the water to replicate *in situ* oxygen concentrations, which would be depleted in the closed-system chambers due to consumption by benthic organisms. Samples of the overlying water were extracted over time, and DOC concentrations were measured. The change in concentration over time was used to estimate benthic DOC flux, and fluxes ranged from -0.12 ± 0.27 to 3.08 ± 0.21 mmol m⁻² d⁻¹ (Burdige & Homstead, 1994).

Janssen et al. (2005) deployed an *in situ* chamber in sandy sediments, where porewater advection would likely contribute to benthic flux. The chamber, which was constructed of stainless steel and had a 200-mm diameter, was lowered through the water and into the sediment until the top of the chamber was positioned approximately 120 mm above the SWI. A stirring disk positioned at the top of the chamber provided circulation of the water in the chamber, resulting in a pressure gradient. The authors suggest that their instrumentation can be adjusted to replicate *in situ* pressure conditions (Janssen et al., 2005).

In a study to measure O₂ flux using the eddy correlation technique, Berg et al. (2003) deployed ten benthic chambers at two locations for comparison with results obtained with other methods. The chambers were 19 cm in diameter and were inserted into the sediment such that approximately 12 cm of overlying water was trapped in each chamber. Mixing in the chamber was achieved by a 15-cm diameter rotating disk located

approximately 7 cm above the SWI. Water was collected from the chambers through a sampling port for O₂ analysis. Benthic flux estimates from the chambers at one project site, which were deployed in sediments described as “fine-grained marine mud,” were compared to diffusive flux obtained by measuring O₂ sediment profiles with a microelectrode. The average flux of the four chambers at this site was found to be nearly 1.5 times greater than the average flux calculated from three porewater profile gradients (Fig. 2.1.b). More discussion about this study’s eddy correlation findings will be presented later in this chapter.

Benthic flux chambers attempt to capture a more comprehensive flux than do porewater gradients. However, there are still some issues that can lead to artifact in flux measurement using chambers. While both laboratory and *in situ* benthic chambers do attempt to reproduce advective flow using stirring rods or disks, these chambers do not take into account the same turbulent flow induced by horizontal currents present in tidal or riverine systems. The lack of wave- and current-driven flow may also lead to underestimation of porewater pressure-induced pumping in coarser sediments (Huettel and Webster, 2002). As noted by Janssen et al. (2005), the circular chamber and stirring disk resulted in a radial pressure gradient. In addition, advection from rotational mixing can lead to an increase in sediment resuspension as compared to true *in situ* conditions (Janssen et al., 2005). Chambers also can lead to underestimates in diffusive flux by maintaining higher concentrations in the overlying water than would exist under true *in situ* conditions, leading to less of a gradient between porewater and surface waters.

2.2. Eddy correlation

Eddy correlation, sometimes referred to as eddy covariance, is a process by which flux of a variable across a plane can be estimated from the covariance of two variables, i.e. vertical velocity and a scalar or horizontal velocity (Glickman, 2000). This correlation can be employed to calculate flux of variables such as momentum, heat, chemical species, particles, or other passive contaminants (Tennekes & Lumley, 1972). In benthic systems, eddy correlation provides a method by which vertical solute flux can be estimated by measuring properties in the water column (e.g., Berg et al., 2003; Kuwae et al., 2006).

Eddy correlation measurement is facilitated by the Reynolds decomposition, in which fluid velocities or passive contaminant concentrations can be broken down into mean and fluctuating values (Tennekes & Lumley, 1972). Reynolds (1896) first presented the mathematical separation of mean and relative motions of matter, which, in the aquatic systems studied here, can be applied to vertical water velocity (w) and solute concentration (C):

$$w = \bar{w} + w' \quad (2.2)$$

$$C = \bar{C} + C' \quad (2.3)$$

where \bar{w} and \bar{C} represent mean values, and w' and C' represent turbulent fluctuations.

The correlation between velocity and concentration can be established by the covariance, or the product of the fluctuating components averaged over a length of time, $\overline{w'C'}$ (Everitt, 2006). If this product does not equal zero, the two variables are considered correlated (Tennekes & Lumley, 1972). The product when applied to momentum is referred to as the Reynold's stress, and when applied to solute transport can be referred to

as eddy flux. Turbulent fluctuations are extracted from the data by manipulating Equations 2.2 and 2.3 to remove the mean:

$$w' = w - \bar{w} \quad (2.4)$$

$$C' = C - \bar{C} \quad (2.5)$$

Total vertical diffusive flux of a solute is described by the following equation (Boudreau, 2001):

$$j = -D \frac{\partial C}{\partial z} + \overline{w' C'} \quad (2.6)$$

where the first term is representative of molecular diffusion, and the second term is representative of eddy diffusion due to turbulent fluctuations. Since vertical transport in the water column is dominated by turbulent fluctuations (Berg et al., 2003), the molecular diffusion term can be neglected such that the covariance of vertical velocity and solute concentration is representative of the total vertical flux:

$$\text{Flux} = \overline{w' C'} \quad (2.7)$$

In this research, flux will be calculated from the turbulent fluctuations of vertical velocity and DOC concentration measured in the water column a short distance above the SWI.

2.2.1. Eddy correlation in atmospheric sciences

The eddy correlation technique has been utilized in atmospheric sciences since the mid-twentieth century to measure fluxes of properties such as energy and mass transfer. Eddy correlation is applicable to these types of measurements because atmospheric turbulence is the driving force behind transfer in the lower atmosphere (Dyer & Maher, 1965). These fluxes are of interest in the agriculture, forestry, hydrology, and ocean

science fields. The first direct method of measuring vertical eddy flux was developed by Swinbank (1951) to quantify vertical heat and water vapor fluxes induced by turbulent wind eddies over open grasslands in Australia. Swinbank's eddy correlation apparatus made use of a hot wire anemometer to measure wind speed and thermocouples to measure temperature and humidity.

Eddy correlation measurements were initially difficult due to complicated data collection and processing. In addition, a major concern regarding instrumentation was ensuring that sensor response times were fast enough to capture the smallest eddies that contribute to turbulent flux. Dyer (1961) successfully employed the use of an automatic instrument, known as the Evapotron, which simplified the required measurements. The accuracy of eddy flux measurements obtained using this instrument was verified by comparison with surface energy balance, including evaporation and radiation measurements made using different instruments (Dyer & Pruitt, 1962). The Evapotron was improved upon with the creation of the Fluxatron, which filtered out non-turbulent eddies that do not influence eddy flux (Dyer et al., 1967). The instrument was then advanced further so that it could measure Reynolds stress (Hicks, 1970).

It was recognized that the use of fast response chemical sensors would allow eddy correlation to measure real-time, instantaneous flux of various analytes in the atmosphere. Eastman and Stedman (1977) used eddy correlation with a chemiluminescent ozone meter and achieved good correlation between ozone and momentum flux. Eddy correlation was also used to quantify particulate flux near an oil refinery (Wesely et al., 1977). Such applications illustrate the capability of eddy correlation to monitor flux of pollutants into the atmosphere. In addition, a fast response

CO₂ sensor was developed for atmospheric eddy correlation measurements to study ocean-atmosphere exchange (Jones et al., 1978).

2.2.2. Eddy correlation in aquatic environments

The eddy correlation technique utilized for atmospheric measurements has been adapted for in situ application in aquatic environments. For example, West and Oduyemi (1989) measured turbulent velocity fluctuations with an electromagnetic current meter and measured suspended solids concentration with a siltmeter to determine Reynolds stresses and suspended solids flux in two estuaries. Similarly, van der Ham et al. (1998) determined Reynolds stresses and vertical sediment flux in an estuary. Fiber optic turbidity meters operating at 20 Hz were used to quantify suspended sediment concentration. In another study, energy and momentum fluxes between water and ice were determined from measurements made using an ultrasonic current meter and a fast-response temperature-conductivity meter (Shirasawa et al., 1997). More recently, studies have used eddy correlation to measure solute flux across the SWI (Table 2.1). The following section briefly describes some of the deployment characteristics and data analysis associated with these studies.

Table 2.1. Summary of eddy correlation studies and deployment characteristics for measurement of benthic flux.

	Flux Analyte	Location	Water Depth (m above SWI)	Measuring Height (cm above SWI)	Bottom Characteristics	Time Series	Averaging Window	Freq. (Hz)	Validation	Avg. Daily Flux ($\text{mmol m}^{-2} \text{d}^{-1}$)
Berg et al., 2003	O ₂	River Wümm, Germany	1	15, 20, 40, 55	sandy	10 min	moving average, e.g. 148 s	25	-	-210 ± 16
		Aarhus Bay, Denmark	12	15	fine-grained marine mud	10 min		25	O ₂ microprofiles, <i>in situ</i> chambers	~ -38
		Limfjorden Sound, Denmark	8	40	fine-grained marine mud	10 min		25	<i>in situ</i> chambers	~ -46
Kuwae et al., 2006	O ₂	Banzu intertidal sand flat, Tokyo Bay, Japan	0.37-0.65	7-17	well-sorted fine sand	12-40 min	block average, 2 min	20	core-incubation	~ -311 to +122
Crusius et al., 2008	ground-water	Salt Pond Channel, Cape Cod, MA, USA	0.6-0.8	5-15	estuarine sediment	15 min (3.5 hr)	-	16-64	seepage meters, ²²² Rn tracer	+16.9 ± 2.9 to +20.7 ± 2.9*
McGinnis, et al., 2008	O ₂	Lake Wohlen, Switzerland	3	15	lake sediment	15-60 min (18 hr)	multiple methods	32	O ₂ microprofiles	-40 ± 11
Brand et al., 2008	O ₂	Lake Alpnach, Switzerland	27	11	lake sediment	15 min (12 hr)	linear detrending	8	O ₂ microprofiles	-13.9 ± 6.8 to +0.3 ± 0.1
Berg et al., 2009	O ₂	Sagami Bay, Japan	1450	5-30	fine-grained marine mud	13.5 min (30 hr)	least square linear fit	64	O ₂ microprofiles, <i>in situ</i> chambers	-1.62 ± 0.23

*units: cm d^{-1}

In the first use of eddy correlation to quantify flux of a dissolved species in water, Berg et al. (2003) coupled a fast response Clark-type O₂ microelectrode with an ADV to capture O₂ uptake by marine sediments. Berg recognized that “vertical transport of O₂ through the water column toward the sediment surface is facilitated by turbulent motion” (Berg et al., 2003). Instrumentation was deployed at three study sites (Table 2.1). At one site, the measurement volume was varied from 15 cm to 55 cm above the SWI in order to compare the effects of measurement volume height on the resulting O₂ flux measurements. At the other two sites, eddy correlation flux values were compared with flux calculated using O₂ microprofiles and benthic chambers (Fig. 2.1). The differences in flux between each of the three methods at the Aarhus Bay site and the two methods at the Limfjorden Sound site were attributed to each method’s varying ability to capture flux due to macrofaunal influence. The results of the study illustrated the potential for eddy correlation to be used for O₂ flux measurement, as well as for other dissolved analytes for which fast-response sensors exist. Trend removal was performed using a moving average, and optimum averaging window was established by plotting O₂ flux against varying averaging window. The averaging window length where O₂ flux leveled off was chosen for use in trend removal. Spectral analysis showed that the frequencies contributing to vertical O₂ flux were less than 1 Hz (Berg et al., 2003).

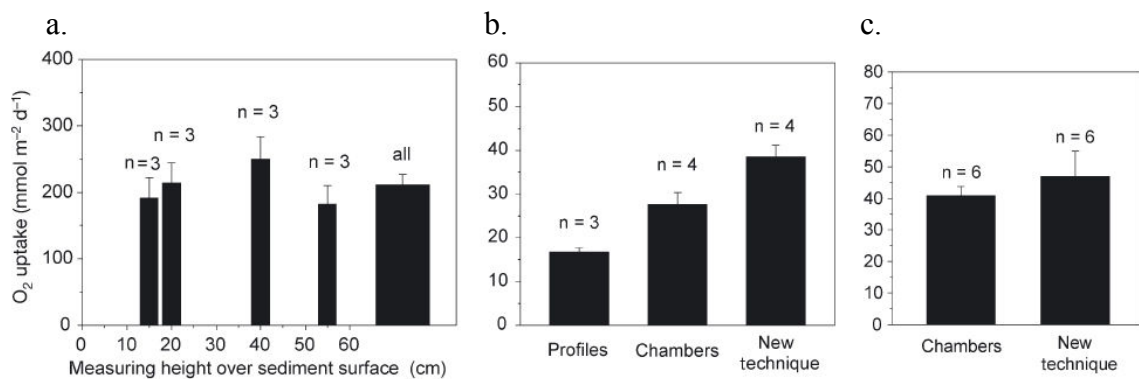


Figure 2.1. Comparison of O₂ flux: (a.) O₂ eddy correlation flux estimates at varying measurement volume heights collected at River Wümme; (b.) Comparison of O₂ flux using different methods at Aarhus Bay; and (c.) Comparison of O₂ flux using different methods at Limfjorden Sound (*reproduced from Berg et al., 2003*).

Kuwae et al. (2006) expanded upon the methods developed by Berg et al. (2003) for measuring sediment O₂ flux. An ADV and a Clark-type O₂ sensor were deployed over fine, sandy sediments in a tidal flat in Tokyo Bay, Japan. The authors examined the effects of high-frequency components of w' and C' , and found that frequencies > 5 Hz had an effect of $< 7\%$ on total flux. They also found that the O₂ sensor's response time of < 0.3 s was sufficient to capture turbulent fluctuations contributing to flux. Kuwae et al. (2006) also investigated the implications of detrending to remove the effects of long-term changes in concentration. Trends were removed using linear regression over 2-min blocks, and flux data showed that detrending was necessary during periods in which concentration varied with time. Eddy correlation flux produced similar results to flux obtained in previous studies using sediment core incubation. The authors found a high degree of variability, which was attributed to either actual variations in flux or artifact in the eddy correlation measurements. By studying spectral analysis, the authors concluded that wave-induced vertical fluctuations between frequencies of 0.3 and 1.4 Hz were the dominant process controlling O₂ flux (Fig. 2.2) (Kuwae et al., 2006).

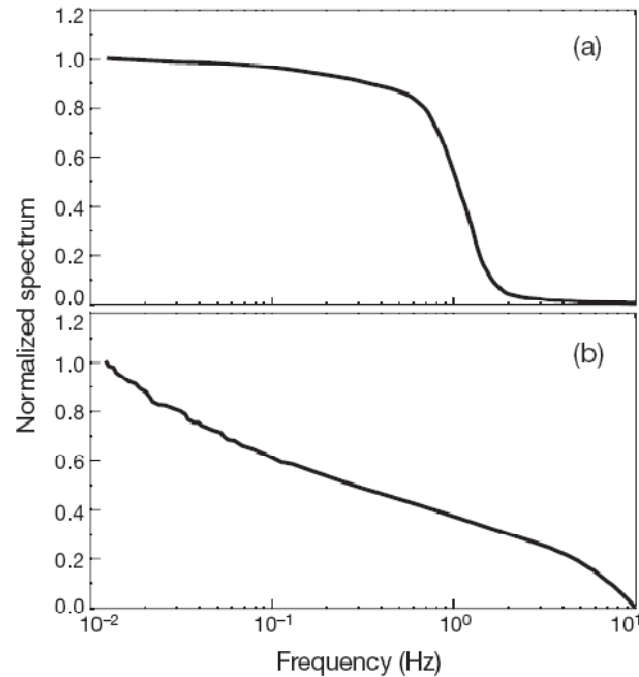


Figure 2.2. Example of cumulative spectra for (a.) w' and (b.) C' , cumulated from the high-frequency end (*reproduced from Kuwae et al., 2006*).

Berg et al. (2007) used mathematical modeling to investigate and develop equations for determining the size and orientation of the footprint, or sediment surface area contributing to benthic flux as calculated by eddy correlation. The footprint depends on factors including water depth, sediment surface roughness, and current velocity (Berg et al., 2007).

Crusius et al. (2008) expanded on the previous aquatic eddy correlation methods and applied the technique to the measurement of groundwater discharge into surface waters. Salinity and temperature, measured by rapid response sensors, were used as tracers for groundwater input, since these two characteristics differ for groundwater and the overlying surface water. The sensor, coupled with an ADV, was deployed in a tidal channel at the Cape Cod National Seashore. Eddy correlation measurements were taken at night, so solar radiation would not affect temperature measurements in the shallow

water. Cumulative heat and salt fluxes were calculated using eddy correlation methods and were converted to groundwater specific discharge. The two tracers produced similar discharge rates. In addition, values compared well with flux obtained using traditional seepage meters and ^{222}Rn modeling (Crusius et al., 2008).

McGinnis et al. (2008) utilized the techniques developed by Berg et al. (2003) to measure O_2 flux over a 38-hr period in Lake Wohlen, a shallow freshwater environment in Switzerland. An O_2 sensor with a 2.25-s response time was coupled with an ADV, and the O_2 sensor lag led to an error in total flux of $< 5\%$. Different flux calculations were done using a program that used mean removal, linear detrending, and a moving average to determine turbulent fluctuations in velocity and concentration. Eddy correlation flux values were comparable to results from O_2 microprofiles. Differences in contributing eddy sizes were observed between daytime and nighttime deployment periods, and optimum averaging window lengths were 60 s and 250 s, respectively. The authors recognized the importance of trend removal to separate turbulent fluctuations from large-scale advective flow, but noted that uncertainty exists due to the lack of a distinct spectral shift to distinguish the two processes (McGinnis et al., 2008).

Brand et al. (2008) used eddy correlation to measure O_2 flux in Lake Alpnach, Switzerland, a water body that experiences highly-variable flow characteristics as a result of varying wind energy inputs. The study aimed to examine relationships between bottom boundary layer dynamics and benthic exchange processes. A fast-response Clark-type O_2 sensor was coupled with an ADV for eddy correlation measurements. Temperature profiles in the bottom 4 m of the water column were also collected during the deployment to model hydrodynamics resulting from internal lake seiching. Trend

removal of velocity and concentration data was performed on 15-min bursts of data using linear detrending. Flux results showed high temporal variation due to the hydrodynamics in the lake. Eddy correlation flux was compared with flux obtained from sediment microprofiling, and in some cases, eddy correlation produced values three times larger than the traditional profile method. Extensive spectral analysis and studies of changes in velocity and turbulent conditions were done to examine flux variability. Periods of negligible flux occurred when both horizontal velocities and vertical turbulent velocities were small, while net flux occurred when the Reynolds number was above 1700 (Fig. 2.3). When the bottom boundary layer was completely mixed, the O₂ concentration gradient was low, and thus flux was also negligible. The authors note that previous aquatic eddy correlation studies were done in environments where steady state conditions could be assumed. In the highly-variable hydrodynamic conditions of Lake Alpnach, however, turbulent O₂ transport between the bottom boundary layer and the lake's interior is not necessarily indicative of flux across the SWI (Brand et al., 2008).

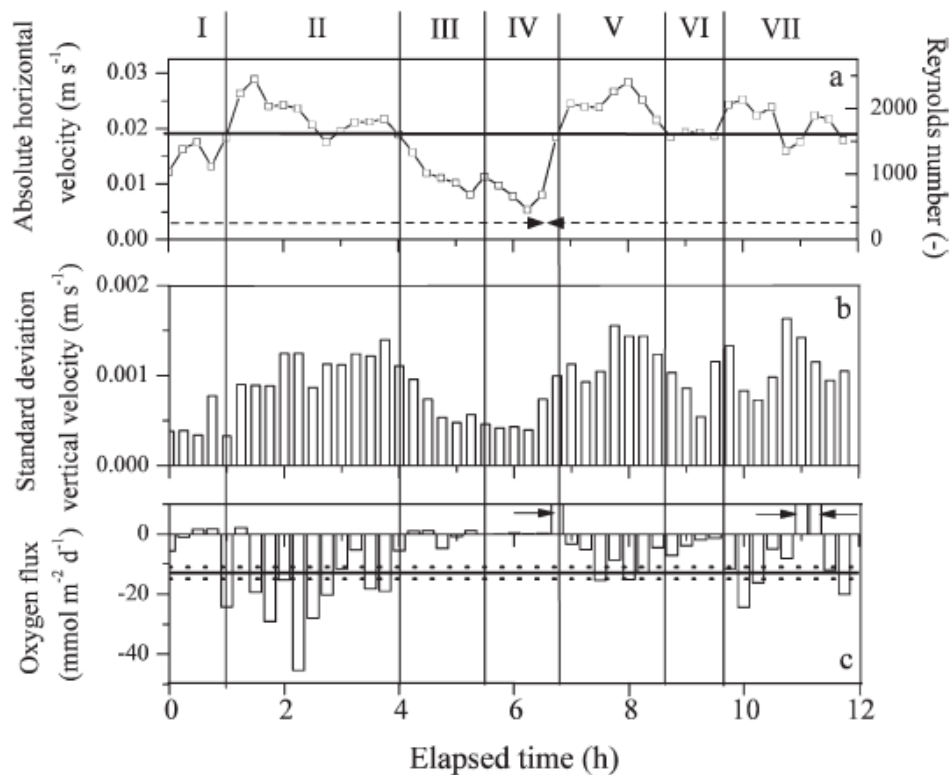


Figure 2.3. Plots illustrating the relation between turbulent velocities and O_2 flux. Positive flux occurred during some transitions between highly-turbulent and less turbulent flow (*reproduced from Brand et al., 2008*).

Berg et al. (2009) revisited the eddy correlation technique to measure small O_2 sediment fluxes in deep ocean waters. A fast-response Clark-type O_2 sensor and ADV were deployed at the sediment surface in 1450-m-deep water using a free-falling lander, and adjustments were made using a remotely operated vehicle. The study also detailed O_2 microprofiling and benthic chamber deployments used for verification of the eddy correlation technique. The deep ocean site was characterized by lower horizontal and vertical velocities and lower concentrations of suspended particulate matter than in estuarine sites, which led to greater high-frequency noise in velocity measurements. The noise was described as being “randomly distributed around the mean,” so the presence of noise did not lead to contamination of flux estimates. According to the authors, the

environmental conditions actually produced a “strong eddy flux signal,” indicating nearly steady state conditions (Berg et al., 2009). Least-square linear fits were used to remove trends from velocity and concentration data. Using spectral analysis, the authors determined that eddies contributing to flux were in the frequency range of 0.0025 Hz to 0.62 Hz (Fig. 2.4.a). Eddy correlation flux estimates were very similar to values obtained using chambers and profiling (Fig. 2.4.b) (Berg et al., 2009).

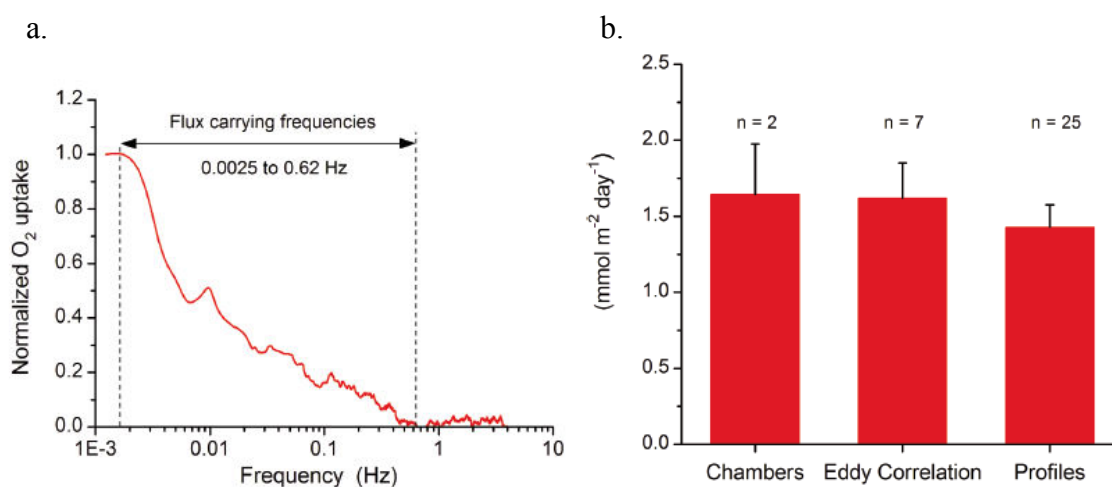


Figure 2.4. Example cospectrum and comparison of O_2 flux: (a.) Example normalized cumulative cospectrum showing frequency range of eddies contributing to flux; (b.) Comparison of flux estimates (O_2 uptake) from three techniques (*reproduced from* Berg et al., 2009).

Chapter 3

MATERIALS AND METHODS

3.1. Acoustic Doppler velocimeter

A Vector acoustic Doppler velocimeter (ADV) (Nortek AS, Rud, Norway) was used to obtain water velocity measurements. The ADV (Fig. 3.1) uses Doppler principles to measure particle velocities in three dimensions via acoustic backscattering. The particle velocity measured by the ADV is used as a proxy for water velocity. Velocity measurements are taken within a cylindrical volume 14 mm in diameter by 14 mm in height, located 15.7 cm from the instrument's transmit transducer. A sonic pulse is emitted from the transmit transducer, and echoes are returned to the three receive transducers. In turn, the instrument converts the change in frequency of the sonic pulse into three-dimensional particle velocity. The ADV has a maximum sampling rate of 64 Hz, but 8 Hz was used throughout this project due to the limitations of the fluorescence sensor, as described in the next section.

The ADV construction includes a titanium probe and receiver arms, which hold the epoxy-coated transducers. The probe is attached to a Delrin[®] pressure casing, which contains the onboard data collection and storage system. Also contained in the pressure casing is an internal battery pack. The internal pack used on this project utilized NiMH rechargeable batteries (total maximum voltage of 13.1 V) and was used either alone or as a backup for a 15 V external marine battery.

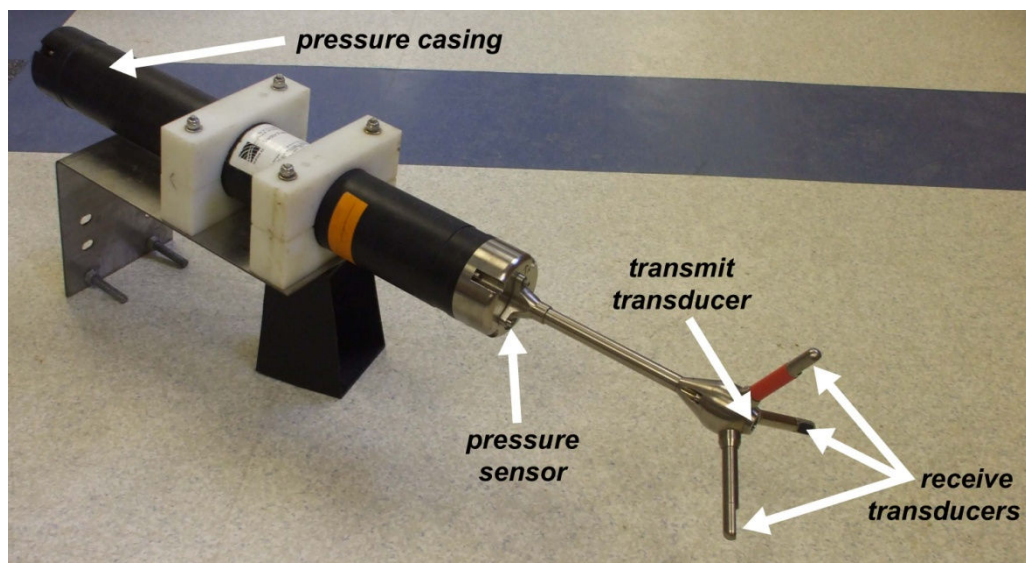


Figure 3.1. Vector acoustic Doppler velocimeter held in bracket.

The onboard data acquisition system stores data in a binary format that can be converted to ASCII files using the appropriate software. The ADV records x-, y-, and z-direction velocity vectors and additional information such as signal-to-noise ratio and signal strength. In addition, the pressure casing has built-in pressure, temperature, compass, and tilt sensors. The ADV can also accept and record data from up to two analog inputs.

3.2. Fluorometer

An ECO-FL chromophoric dissolved organic matter (CDOM) fluorometer (WETLabs, Philomath, OR, USA) was used to measure in situ CDOM concentration, which is an indicator of DOC concentration (Blough & Del Vecchio, 2002) (Fig. 3.2). The instrument is housed in an acetal copolymer pressure casing measuring 6.3 cm in diameter and 12.7 cm in length. The ECO-FL operates at a maximum sampling rate of 8 Hz. The ECO-FL utilizes excitation and emission wavelengths of 370 nm and 460 nm,

respectively, corresponding to the fluorescence characteristics of CDOM. The fluorometer measures CDOM concentration at approximately 2 cm from the face of the optics head. Unlike some other fluorometers, the ECO-FL is not a flow-through device, thus reducing the chance of contaminating velocity measurements.

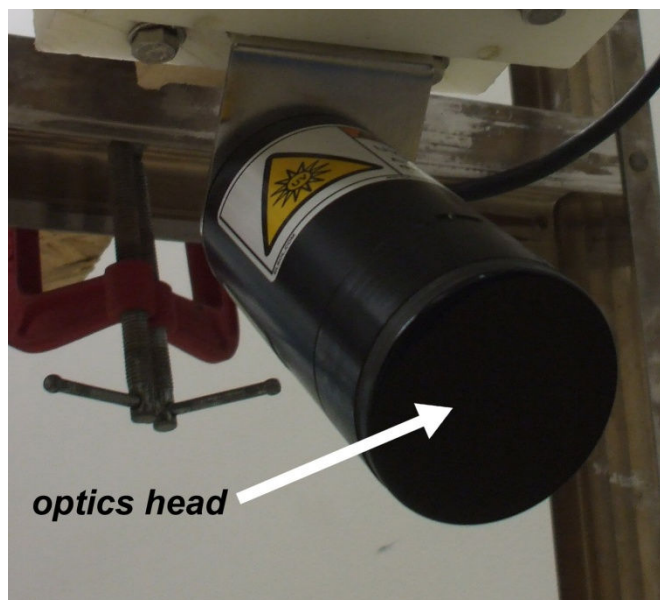


Figure 3.2. ECO-FL CDOM fluorometer mounted on bracket at 45°.

This particular fluorometer has an analogue output voltage range of 0.025 V to 4.96 V, with a resolution of 1.6 mV. This is converted to a digital signal ranging from 64 counts to 16327 counts, with a resolution of 2 counts. The minimum value of 64 counts, or dark current, is the output when the optics head is covered with black tape and submerged in clean water, as determined by the manufacturer.

The ECO-FL was calibrated in the laboratory using multiple concentrations of water collected from Burton Bog, one of the project field sites. The ECO-FL was connected as an analog through the ADV, and both were powered by an external marine

battery with a backup internal battery pack to emulate the power and data collection conditions used in the field. During calibration, the ECO-FL was placed in an acid-washed plastic tank, which was entirely concealed with aluminum foil to prevent light from entering the system.

For each dilution, the ECO-FL collected 3 min of data. Each 3-min set of data was then averaged to obtain a single mean fluorescence count for each dilution. Immediately following each data collection period, a 120-mL sample of water was collected in an acid-washed plastic bottle. Each sample was filtered through 0.45- μm filter paper and preserved with 4 drops of a 1:1 18M sulfuric acid and DI water solution. Samples were stored at 4°C until DOC concentration measurement.

Samples were run through a 1010 Total Organic Carbon (TOC) Analyzer (OI Analytical, College Station, TX, USA) to measure DOC concentration. Calibration standards were prepared using potassium hydrogen phthalate for concentrations ranging from 0 to 30 ppm. The standard curve produced $R^2 = 0.9993$. The collected samples from the ECO-FL calibration were then run through the TOC analyzer within 24 hr of collection, and the resulting concentrations were plotted against the fluorometer digital counts to obtain a calibration curve. The curve was fit to a linear function with $R^2=0.98$, (Fig. 3.3).

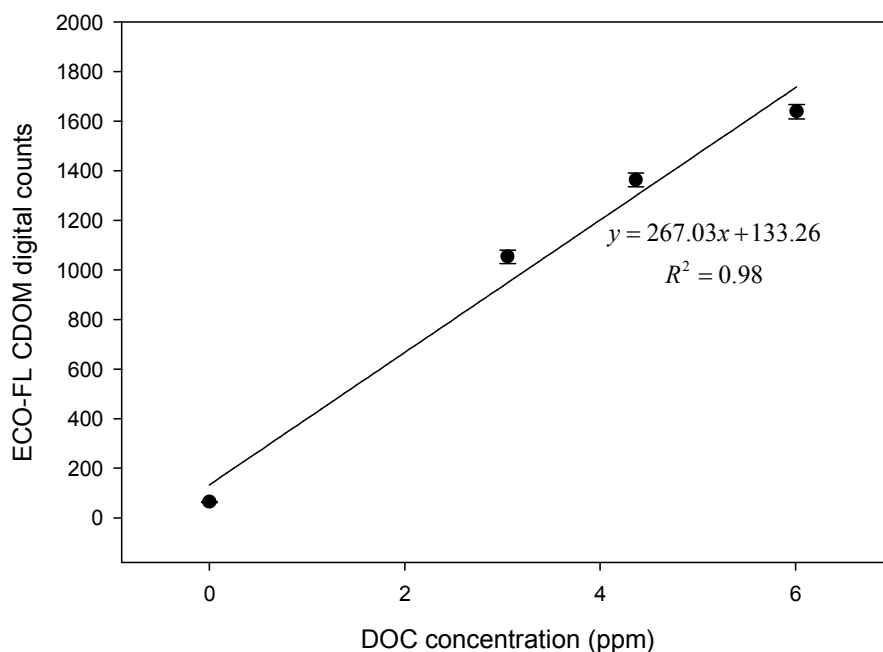


Figure 3.3. CDOM fluorometer calibration curve based on diluted Burton Bog sample water and dark current value.

3.3. Deployment setup

For deployments, the two instruments were attached to an A-frame aluminum step ladder (Fig. 3.4), similar to the setup previously used by Kuwae et al. (2006). The ADV was mounted vertically and held in place by an acrylic and stainless steel bracket that was clamped to a ladder rung. The ADV was easily adjustable to the desired measuring height, and the bracket's rigidity prevented excessive wind and wave-induced movement of the instrument. The ECO-FL was mounted to a lower ladder rung using a different acrylic and stainless steel bracket that allowed the instrument to be oriented pointing downward at a 45 degree angle to reduce the instrument's influence on water flow through the ADV's measurement volume. The 6-pin fluorometer was connected by a water-tight cable to the analog receiver of the ADV.

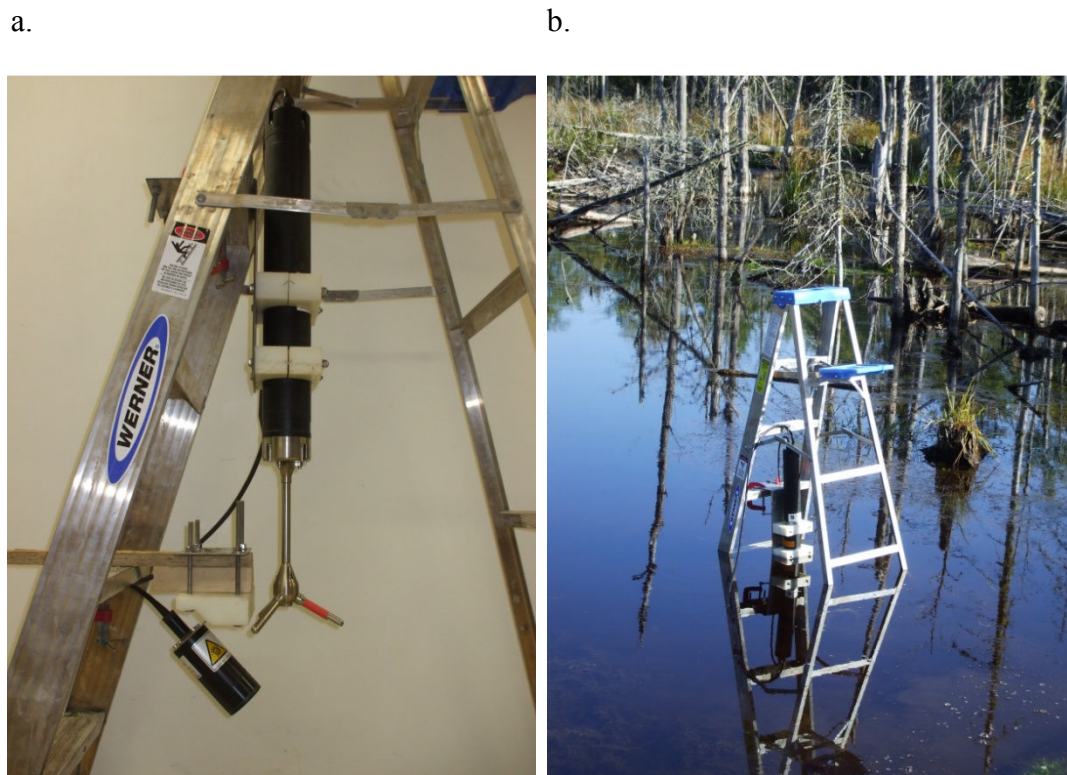


Figure 3.4. Eddy correlation instrumentation setup: (a.) Instrument setup in laboratory and (b.) deployed in field to measure 12 cm above the SWI at Burton Bog (right).

Due to restrictions of the instruments' sizes and orientations, the two instruments did not share exactly the same measurement volume. For a typical field deployment, the ADV and fluorometer measurement volumes were located as much as 2 cm apart. This distance was acceptable, however, since smaller eddies that would not be captured due to the difference in measurement volumes, do not contribute significantly to momentum and solute transport compared with larger eddies (Tennekes and Lumley, 1972). The ladder was positioned so that the primary direction of flow occurred between the ladder's legs and orthogonal to the face of the fluorometer.

Data can be monitored real-time on a computer, but for autonomous field deployments, the data collection specifications were set in the field using a laptop

computer, which was then disconnected during deployment. For each of the four project sites studied in this research, data were collected continuously at 8 Hz for the duration of the deployment time.

3.4. Project sites

Four study sites were chosen for deployments: (1) Frankfort Flats, Frankfort, ME; (2) Squamscott River, Stratham, NH; (3) Piscataqua River, Kittery, ME; and (4) Burton Bog, Old Town, ME. Sites were chosen based on accessibility and availability to monitor a deployment for several hours. The first three sites, which are all intertidal mudflats, were the subject of concurrent and prior research, and the sediments at these sites are well-characterized, including the DOC porewater gradients.

3.4.1. Frankfort Flats

Frankfort Flats (Fig. 3.5) is located in the Lower Penobscot watershed at the mouth of Marsh Stream in Frankfort, ME. The intertidal mudflat, characterized by fine-grained, cohesive marine sediments, is adjacent to an estuarine salt marsh dominated by *Spartina* spp. The site has been the subject of mercury studies that have also characterized porewater DOC concentrations at various depths in the estuarine sediment (Merritt, 2007; Merritt & Amirbahman 2007a & b). In a previous study, LOI ranged from 3-9%, and approximately 80% of the sediment was $< 0.63 \mu\text{m}$ (Merritt, 2007).



Figure 3.5. Frankfort Flats deployment site (●) near the confluence of Marsh Stream and the Penobscot River (photo from NAIP, 2009).

The eddy-correlation instrumentation was deployed on August 19, 2009 for approximately 1.7 hr during high tide. Previous test deployments at this site were done with the measurement volume positioned as low as 10 cm from the sediment surface, but sediment resuspension resulted in the face of the fluorometer becoming covered with a film of sediment. Therefore, the final measurement height used for data collection was 35 cm. The instrumentation was placed on the mudflat at low tide, and data collection was initiated when the water depth reached 2.66 m above the SWI. The water depth, calculated from pressure sensor readings, ranged from 2.54 m to 2.76 m during deployment, with an average of 2.68 m. Average DOC concentration in the measurement volume during the deployment was 3.51 ± 0.17 ppm (mean \pm SD). Average horizontal velocity was 2.1 ± 1.0 cm/s (mean \pm SD).

Due to the lateral extent of tidal inundation at this site, use of an external battery on adjacent dry land was not feasible, so power for this deployment was provided by the internal battery only. The initial battery voltage was 13.1 V and decreased steadily throughout the deployment until it reached 10 V at approximately 1.7 hr after the initiation of data collection. The voltage then dropped quickly to 8 V, and the ADV subsequently entered a power-conservation mode, leading to discontinuous data collection. Therefore, data obtained at a voltage of less than 10 V was discarded.

3.4.2. Squamscott River

The instrumentation was deployed on September 2, 2009 near the mouth of the Squamscott River in Stratham, NH. The Squamscott River (Fig. 3.6) drains into Great Bay, and the tidal portion of the river where this research was conducted is part of the Great Bay Estuary. As part of concurrent research on porewater and sediment mercury geochemistry (Brown, 2010), sediment cores were extracted from the mudflat during low tide and sectioned, producing the porewater profile data shown in Table 3.1.



Figure 3.6. Squamscott River deployment site (•) in Great Bay Estuary (photo from NAIP, 2009).

Table 3.1. Porewater profile data obtained from sediment cores collected at Squamscott River mudflat (Brown, 2010). Average porosity from a different core collected in August 2008 was 0.81.

September 2009			
Depth (cm)	DOC (ppm)	Fe (II) (μm)	%LOI
0.5	10.5	201.7	6.3
1.5	13.6	383.8	9.5
2.5	10.0	401.8	9.1
3.5	22.8	413.4	9.6
4.5	13.2	335.1	8.8
5.5	18.4	389.5	8.8
6.5	16.6	303.5	8.5
7.5	19.6	140.5	8.2
8.5	11.2	97.4	7.3
9.5	18.2	98.6	7.6
Average =			8.4

The eddy-correlation instrumentation was deployed on a narrow intertidal mudflat, directly adjacent to a large salt marsh inhabited by *Spartina* spp. The mudflat was characterized by fine-grained cohesive sediments. The instrument measurement volume was situated 25 cm above the SWI. The instruments were powered by an external marine battery. An internal battery pack was installed as backup but was not needed during the deployment. The water depth above the SWI ranged from 0.96 m to 1.78 m, with an average depth of 1.44 m. The average DOC concentration in the measurement volume was 5.36 ± 0.63 ppm (mean \pm SD). The site was nearby to a popular public boat launch. Boating occurred in the channel during the deployment and created wakes, which may have led to increased velocity measurements. Average horizontal velocity was 6.5 ± 3.9 cm/s (mean \pm SD).

3.4.3. Piscataqua River

The Kittery, ME deployment site was on a mud flat in a sheltered tidal inlet of the Piscataqua River near Portsmouth Naval Shipyard. The inlet (Fig. 3.7) was characterized by a small freshwater stream flowing into the river. Compared to the previous two estuarine sites, the surface sediments at the Kittery site were lighter in color and were less cohesive. There was less organic matter in the sediments at this site, as indicated by the lower loss on ignition (LOI). The site also had considerably more benthic macrofauna throughout the sediment column. Sediment cores were extracted during low tide, and Table 3.2 shows porewater profile data for some geochemical properties.



Figure 3.7. Kittery deployment site (•) on the Piscataqua River (photo from NAIP, 2009).

Table 3.2. Porewater profile data obtained from sediment cores collected at Kittery mudflat (Brown, 2010). A core collected at the same site in August 2008 yielded an average porosity of 0.67 and an average LOI of 5.6%.

September 2009		
Depth (cm)	DOC (ppm)	Fe (II) (μm)
0.5	3.5	107.6
1.5	2.7	171.6
2.5	2.8	245.0
3.5	4.4	180.5
4.5	6.0	224.9
5.5	18.4	180.1
6.5	10.8	211.1
7.5	18.2	55.9
8.5	20.0	70.5
9.5	27.7	53.8

Instrumentation at the Piscataqua River site was deployed on September 3, 2009 for 5.8 hrs. Again, power was provided by an external marine battery. Water depth ranged from 0.98 m to 2.26 m, with an average depth of 1.87 m. The measuring height was 30 cm above the SWI. The overlying water at this site had a low DOC concentration, averaging 1.28 ± 0.19 ppm (mean \pm SD) over the entire length of the deployment. Average horizontal velocity was 2.9 ± 1.9 cm/s (mean \pm SD).

3.4.4. Burton Bog

Burton Bog (Fig. 3.8) consists of a series of tiered beaver ponds located on private lands in the Lower Penobscot watershed. The wetland area ultimately drains into a tributary of the Penobscot River north of Orson Island. Advective flow is driven primarily by wind at this freshwater site, as there is no tidal-induced current or significant gravity flow. Large algal mats were suspended in the water column. The sediments at this site have not been characterized. Data were collected during an 8-hr deployment on September 9, 2009, and the instruments were powered by an external marine battery. The ADV's pressure sensor was not properly calibrated for this deployment, but the water depth was measured as 60 cm above the SWI. The deployment measuring volume was 12 cm above the SWI. DOC concentrations were higher at this site than at the other three project sites and did not fall within the linear range of the CDOM calibration curve. A water sample from the site had a DOC concentration of 28.5 ppm, as measured using a TOC analyzer. Due to the long retention time of this multi-pond system, DOC tends to accumulate. As expected, horizontal velocity was slowest at this site, averaging 0.7 ± 0.5 cm/s (mean \pm SD).



Figure 3.8. Burton Bog deployment site (•) in the Lower Penobscot watershed (photo from NAIP, 2009).

3.5. Data Analysis

Data analysis was performed using the MATLAB programming environment. Text versions of the code developed and used for this project are provided in Appendix A. The ASCII files discussed in section 3.1, which include velocity measurements and analog CDOM counts, were imported into MATLAB for data manipulation. CDOM counts provided by the ECO-FL were converted to concentration of DOC in ppm using the equation presented in Figure 3.3.

The ADV provides continuous pressure measurement, indicating the depth of water above the pressure sensor on the instrument. This pressure reading, given in meters, was filtered down to 1 Hz to improve clarity. Each pressure reading was added to the measured height of the sensor above the SWI in order to obtain the total water depth at any given time during the deployment. Plots showing the change in water depth over time are shown in Appendix B.

Sections of data for preliminary analysis were selected by visual inspection. Bursts of data at least 10 min in length that were relatively stationary in w and C in comparison to the rest of the data were selected, as mean flow must be statistically stationary in order to facilitate adequate trend removal (Tennekes & Lumley, 1972).

3.5.1. Velocity vector rotation

Since the ADV is not mounted perfectly orthogonal to the sediment surface, the three-dimensional velocity vectors require transformation to represent true horizontal and vertical velocities. The ADV provides measurements of pitch and roll, which could be used to translate the velocity vectors (West & Oduyemi, 1989). However, translations would be dependent on the accuracy of the tilt sensor. Therefore, another approach was used. By assuming that variance is minimized in the z -direction, the following relationships were used to develop angles of rotation and transform each velocity vector:

$$\phi = \frac{1}{2} \tan^{-1} \left(\frac{\sum 2u_1 u_2}{\sum u_1^2 - \sum u_2^2} \right) \quad (3.1)$$

$$u_{1_{new}} = u_1 \cos \phi + u_2 \sin \phi$$

$$u_{2_{new}} = -u_1 \sin \phi + u_2 \cos \phi$$

where u_1 and u_2 are velocity vectors (Emery & Thomson, 2004). This two-dimensional rotation is performed three times to correct all three velocity vectors, as detailed in the code (Appendix A). The validity of these transformations was tested by comparing the correlation between C and both the corrected and uncorrected values of w .

3.5.2. Averaging window selection

It is necessary to determine an averaging window size for velocity and concentration trend removal such that the turbulent eddies that contribute to flux are captured in the flux calculations. To accomplish this, blocks of data ranging in length from 10 min to 60 min were analyzed for correlation between w and C at varying filter lengths ranging from 3 s to 10 min. Digital filtering was performed using the *filtfilt* function in MATLAB. This function provides a zero-phase filter by filtering in both forward and reverse directions. The *corrcoef* function was used to calculate the correlation coefficient R at varying filter lengths:

$$R(y) = \left| \frac{\text{cov}\{w(y), C(y)\}}{[\text{var}\{w(y)\} \text{var}\{C(y)\}]^{1/2}} \right| \quad (3.2)$$

where y corresponds to the filter length, and $0 \leq R \leq 1$.

The technique used here is similar to the method used by Berg et al. (2003) and McGinnis et al. (2008) in which flux was calculated directly for varying averaging windows. In this DOC study, however, the correlation is based on the covariance of wC rather than $w'C'$. In order to analyze $w'C'$, trends must first be removed from w and C . The goal of examining correlation in this study is to directly determine from velocity and concentration the window lengths over which to establish these trends.

The optimum window sizes for block or running trend removal were determined by examining the change in correlation plotted over the change in filter length. Optimum window size was established as the filter length at the first local maxima on the correlation plot, indicating a likely shift from small-scale turbulent eddy-induced flux to large-scale advective flux. In cases where local maxima or minima did not exist due to continuously increasing correlation with filter length, the optimum window size was taken as the filter length at the first inflection point of correlation plot. Inflection points were determined by taking the second derivative of a polynomial fit ($R^2 > 0.999$) to the correlation plot. The plot was smoothed prior to fitting to reduce the influence of possible abrupt changes not representative of the overall curve. Smoothing did not significantly affect R^2 values.

3.5.3. Trend removal

Once an optimum averaging window was determined for a burst of data, two different methods were used to establish the trends, \bar{w} and \bar{C} : (1) moving average and (2) linear regression. The moving average technique has been used by Berg et al. (2003) and McGinnis et al. (2008). The moving average was carried out using the *filtfilt* function in MATLAB. The beginning and end portions of each burst corresponding to one half the length of the averaging window were used in calculating the moving average, but were not included in flux calculations, as the data used to calculate the trend for these portions were outside the initial burst. The resulting \bar{w} and \bar{C} values were subtracted from w and C to obtain w' and C' .

Block averaging using the statistical mean of w and C has been utilized previously to establish trends over a burst of data (e.g., Kuwae et al., 2006). The statistical mean, however, does not provide an adequate trend if there is noticeable long-term change or drift in the velocity or concentration over the length of the averaging window. Such conditions were observed in the data collected for this research. Therefore, a linear regression technique, which has been used previously by Brand et al. (2008) and Berg et al. (2009), was adopted. Each burst of data from a particular deployment site was broken down into smaller blocks corresponding to the size of that burst's optimum averaging window. The total number of blocks per burst ranged from 1 to 19. Least squares linear regression was applied to a block of data, producing a "best-fit" line, and the resulting trend was removed to obtain w' and C' .

3.5.4. Flux calculation

Following trend removal of both w and C , instantaneous flux was calculated by multiplying w' and C' . As shown by Kuwae et al. (2006), large variations in w' and C' can be reduced by eliminating values greater than three standard deviations above or below the mean for a given block or averaging window. This method was applied to the data in this study, but it was found that despite the removal, large variations in $w'C'$ over a block of time still existed, leading to possible artifact in cumulative flux over the given period. Therefore, rather than remove the variations prior to correlation, variations greater than three standard deviations were removed from $w'C'$.

The basis of using three standard deviations was also investigated. According to Laws (1997), data falling within a certain number of standard deviations from the mean

can be removed as outliers. Based on a t distribution function, 95% percent of the data should fall within a certain standard deviation range, which varies with sample size. Following this methodology, a data set of only 50 points would require use of a three standard deviation cutoff. Therefore, the use of three standard deviations provides a conservative analysis, since the smallest averaging window used in this study included 1440 data points.

Once instantaneous flux was obtained for a burst of data, the cumulative flux over the entire burst was calculated using a trapezoidal numerical integration method. The cumulative flux over a given period can be extrapolated to estimate average daily flux.

3.5.5. Spectral analysis

Spectral analysis was performed on all blocks of flux data to examine the behavior of the data in the frequency domain. This representation shows the distribution of eddy sizes that contribute to the total flux. The MATLAB *periodogram* function was used to obtain power spectral densities for each burst of data. The resulting spectra were cumulated, normalized, and plotted against the log of frequency (Kuwaie et al., 2006). Spectra were also produced for flux calculated using uncorrected velocity and for flux calculated with no removal of bad data in order to examine the potential effects of these transformations on the data.

Chapter 4

RESULTS AND DISCUSSION

4.1. Data processing

4.1.1. DOC concentration

The CDOM to DOC calibration curve presented in Section 3.2 utilizes the fluorometer's dark current value and the first three data points obtained from the calibration. These four points were fit with a linear trend allowing conversion to DOC concentrations up to 6 ppm. Data at higher concentrations deviated from this trend, as CDOM counts began to level off with increasing DOC concentration. This deviation from linearity is likely due to attenuation in the 4-cm light path length between the source and detector. Absorption and scattering interactions can be attributed to bulk optical properties, including chlorophyll, suspended solids, and dissolved organics. For instance, suspended particulate minerals are known to have an effect on volume reflectance across the CDOM emission wavelength (Bukata et al., 1995). Additional measurements of absorption and backscatter would be required to correct for these issues (e.g. Chen et al., 2004). All data points obtained in the calibration are shown in a plot in Appendix C.

Since CDOM can be affected by site-specific and deployment characteristics, such as temperature, salinity, particles, and depth, laboratory DOC calibrations should ideally be performed on samples collected *in situ* during the deployment (e.g. Downing et al., 2009). For the purposes of this study, all CDOM data were converted to DOC using a single laboratory calibration obtained using water collected from one of the project sites.

This may have led to some bias in DOC concentrations, since laboratory conditions did not replicate field conditions, and the sample water was from a freshwater system, which has considerably lower salinity than the three estuarine sites.

4.1.2. Velocity vectors

The validity of the velocity vector rotations was tested by comparing the correlation between C and both the corrected and uncorrected values of w . Correlation was calculated and plotted as a function of filter length, as described for the averaging window determination in Section 3.5.2. The maximum correlation coefficients obtained in this comparison are shown in Table 4.1, and plots of correlation coefficient vs. filter length are shown in Appendix D.

Table 4.1. Correlation of C with uncorrected and corrected w .

Project Site	Time Range (counts)	Maximum Correlation Coefficient	
		Uncorrected w	Corrected w
Frankfort	76900-81700	0.44	0.45
Frankfort	88000-92800	0.11	0.48
Squamscott	103000-107800	0.06	0.47
Kittery	8700-37500	0.28	0.61
Kittery	127000-141400	0.61	0.45
Burton Bog	no acceptable range	-	-

The corrected velocity vector was more correlated with concentration for all but one of the deployment bursts. The ADV pitch and roll data were examined for the Kittery data set to determine if there were any anomalies that led to a less correlated corrected velocity for the second burst. However, the mean and standard deviation of the angle of

rotation determined from pitch and roll were similar for both bursts from the Kittery deployment. The correlation coefficient of 0.45 from the second Kittery burst is similar to coefficients obtained from other bursts, so the vector rotation was still utilized.

The pressure readings from the ADV, which were converted into the depth of water above the SWI, showed that periods of tidal flow, high tide, and tidal ebb were captured during each estuarine deployment.

4.2. Data selection

DOC concentration and vertical velocity are plotted for the entire collection periods at each project site in Appendix B. Visual inspection yielded a total of five bursts from three of the sites for further analysis, as detailed in Table 4.2.

Table 4.2. Bursts of data selected for flux analysis.

Project Site	Time Range (counts)	Burst Length (min)	Tidal Period
Frankfort	76900-81700	10	Ebb
Frankfort	88000-92800	10	Ebb
Squamscott	103000-107800	10	Ebb
Kittery	8700-37500	60	Flow
Kittery	127000-141400	30	Ebb
Burton Bog	No acceptable range	-	-

The selected bursts account for only 10% of the total data collected during the four deployments. This low percentage of quality data reflects the overall variability in the CDOM concentration as measured with the fluorometer with time in a given measurement volume. High DOC variability over scales shorter than 10 min was typically the controlling factor in eliminating data from further analysis. Frankfort

yielded only two 10-min bursts for analysis, both occurring within a 33-min period, while the Squamscott deployment resulted in only one selected 10-min burst. The Kittery deployment produced the longest periods of steady DOC concentration, which accounted for 28% of that deployment.

The Frankfort and Squamscott deployments took place directly in river channels, where the flow was subject to both tidal influence and continuous current flow. In Kittery the instruments were deployed in a sheltered tidal inlet, and the actual input of freshwater was small in relation to tidal inundation, so riverine currents were not as prevalent as at the other two estuarine sites. There was also no vegetation in the tidal range at the Kittery site, while the banks at the other two estuarine sites were heavily populated by *Spartina* spp., which became inundated at high tide.

DOC concentration remained steady at 1.53 ppm in the initial part of the Kittery deployment during tidal flow. As the tide peaked and subsequently began to ebb, DOC decreased steadily at a rate of 0.15 ppm/hr for about 3 hr until reaching a concentration of 1.06 ppm, where it remained steady for the rest of the deployment.

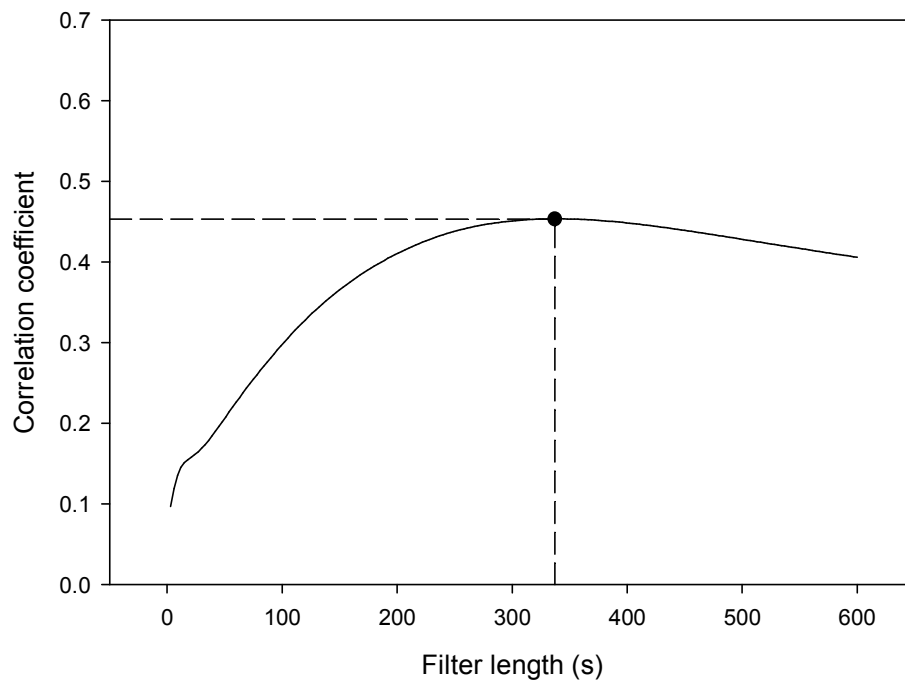
The Burton Bog deployment site was characterized by very low horizontal velocities. Low-velocity deep ocean systems have been studied with success (Berg et al., 2009), but these systems exhibited stationary O₂ concentration, which made establishing trends and calculating O₂ flux feasible. At Burton Bog, DOC concentration was highly variable, suggesting that DOC was controlled by factors other than release from sediment.

4.3. Averaging windows

By examining the correlation between w and C at different filter window lengths, the window length that will adequately capture turbulent eddies can be estimated. Since the eddy-correlation technique depends on the correlation between the two parameters, the correlation coefficient is an indicator of flux contribution, and the filter window length is an indicator of the size of eddies contributing to flux (Tennekes & Lumley, 1972).

Figure 4.1 shows two typical plots of correlation coefficient vs. filter length. In Figure 4.1.a, correlation reaches a local maximum and then begins to decrease with increasing filter length. In Figure 4.1.b, a local maximum is never reached, so the first inflection point was taken as the optimum filter length. The only data set that required use of the inflection point method was the Kittery tidal flow burst. We hypothesize that the inflection point is indicative of a shift in flux contribution from small-scale turbulent eddies to large-scale advective flow. The increase in correlation coefficient at longer filtering lengths beyond the inflection point is likely due to large-scale advection contributing to positive correlation. Similarly, correlation plots that reach a local maximum and then begin to decline illustrate a negative correlation contribution by large-scale advection. By choosing the filter length at the inflection point or local maximum, we attempt to preclude this large-scale influence from the calculation of turbulent eddy flux. We anticipate that in some instances, an inflection point as determined by the second derivative may not exist, so an alternative cutoff method would need to be established.

a.



b.

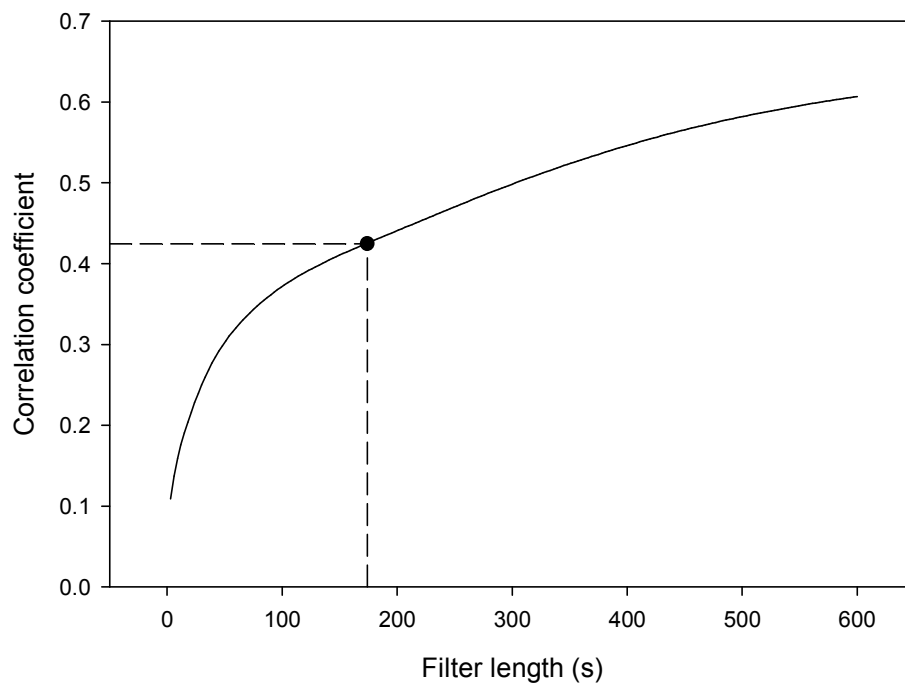


Figure 4.1. Typical plots of filter length vs. correlation: (a.) Plot for Kittery tidal ebb burst showing local maximum (•) at filter length of 337 s; (b.) Plot for Kittery tidal flow burst showing inflection point (•) at filter length of 174 s.

The resulting optimum averaging window lengths for each of the five bursts are reported in Table 4.3. Lengths ranged from 100 s to 337 s, averaging 198 ± 87 s (mean \pm SD), indicating high variability between bursts in the size of eddies contributing to flux.

Table 4.3. Optimum averaging window lengths and resulting number of blocks for each burst.

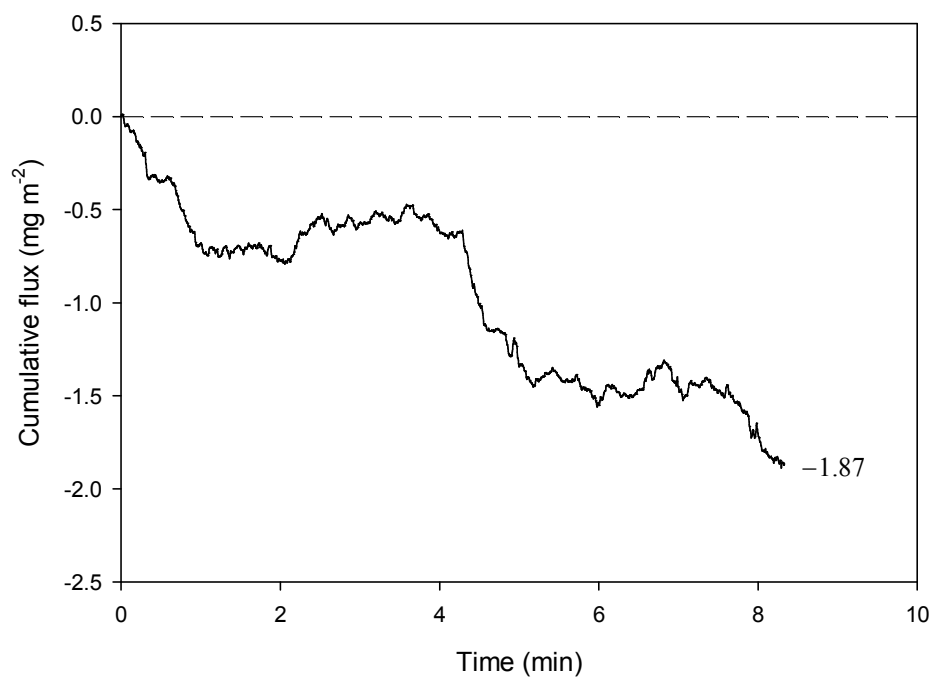
Project Site	Time Range (counts)	Window Length (s)	# of Blocks	Length of Analysis (min)
Frankfort	76900-81700	100	5	8.3
Frankfort	88000-92800	207	1	3.5
Squamscott	103000-107800	170	2	5.7
Kittery	8700-37500	174	19	55.1
Kittery	127000-141400	337	4	22.5

The averaging windows obtained for each burst were utilized to remove trends using linear regression and moving averages, as described in Section 3.5. Plots of velocity and concentration, along with their corresponding trends are available in Appendix E.

4.4. Flux calculation

Following trend removal, cumulative flux was calculated for each data set. Figures 4.2-4.6 show cumulative fluxes calculated using linear regression and moving average techniques for each of the five bursts.

a.



b.

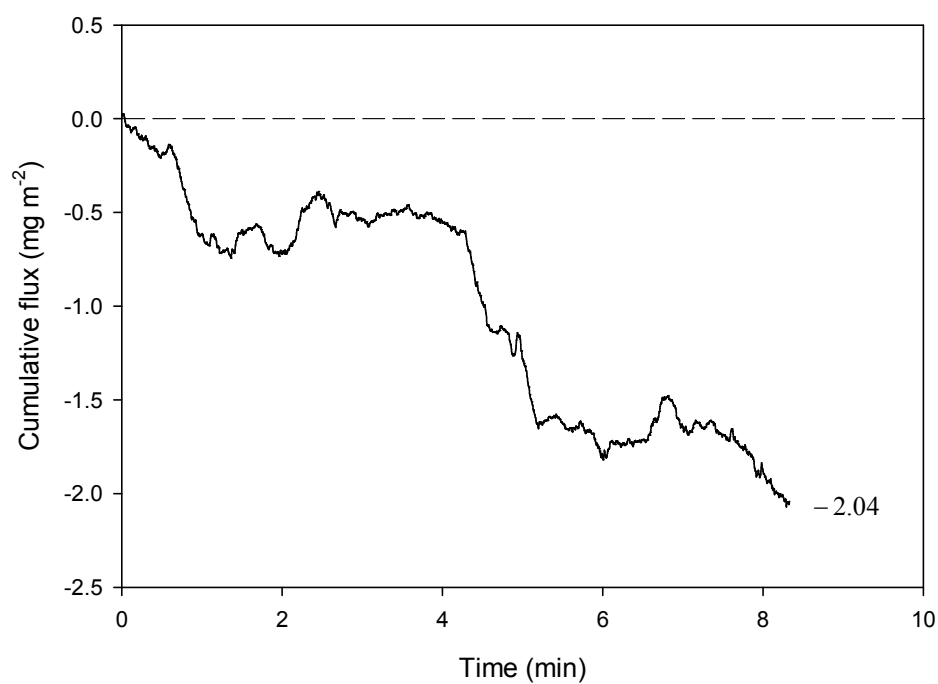
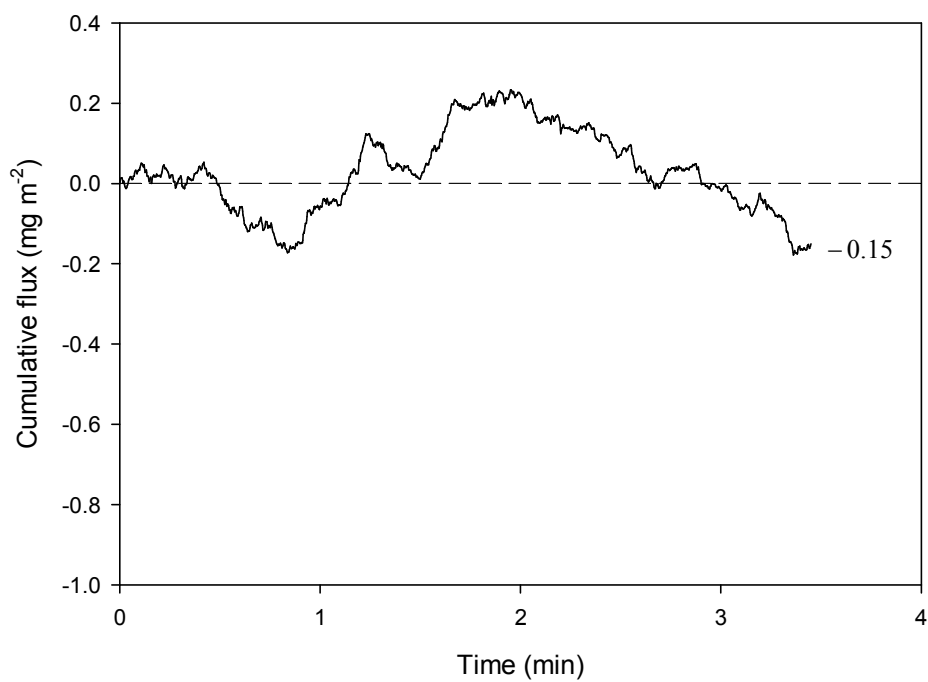


Figure 4.2. Plots of cumulative flux for Frankfort burst 1. Flux is calculated using (a.) linear regression and (b.) moving average techniques. The value reported at the end of each plot is the cumulative flux (mg m⁻²) for the duration of the burst.

a.



b.

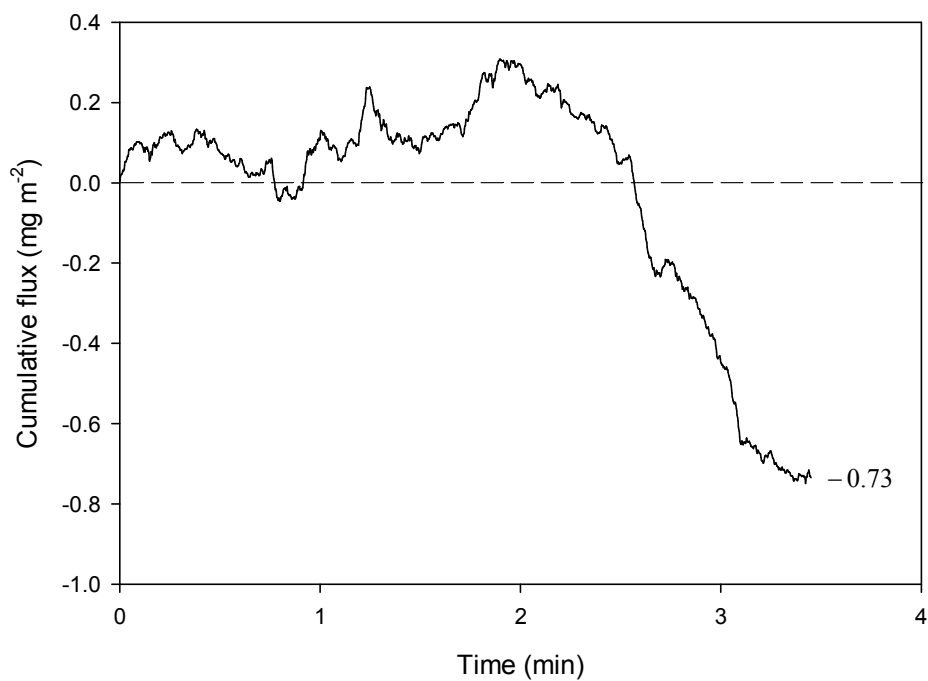
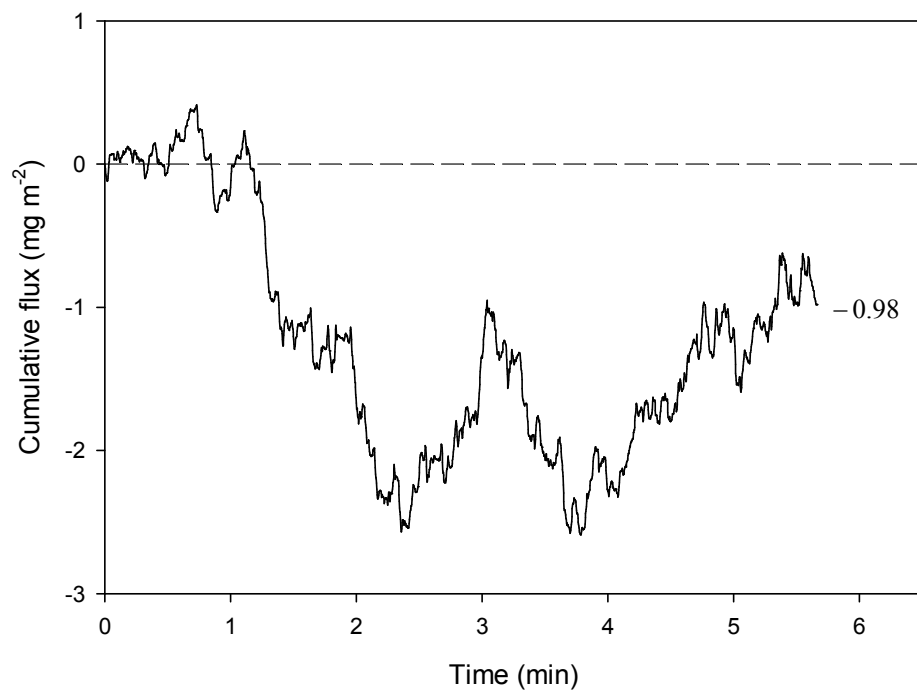


Figure 4.3. Plots of cumulative flux for Frankfort burst 2. Flux is calculated using (a.) linear regression and (b.) moving average techniques. The value reported at the end of each plot is the cumulative flux (mg m⁻²) for the duration of the burst.

a.



b.

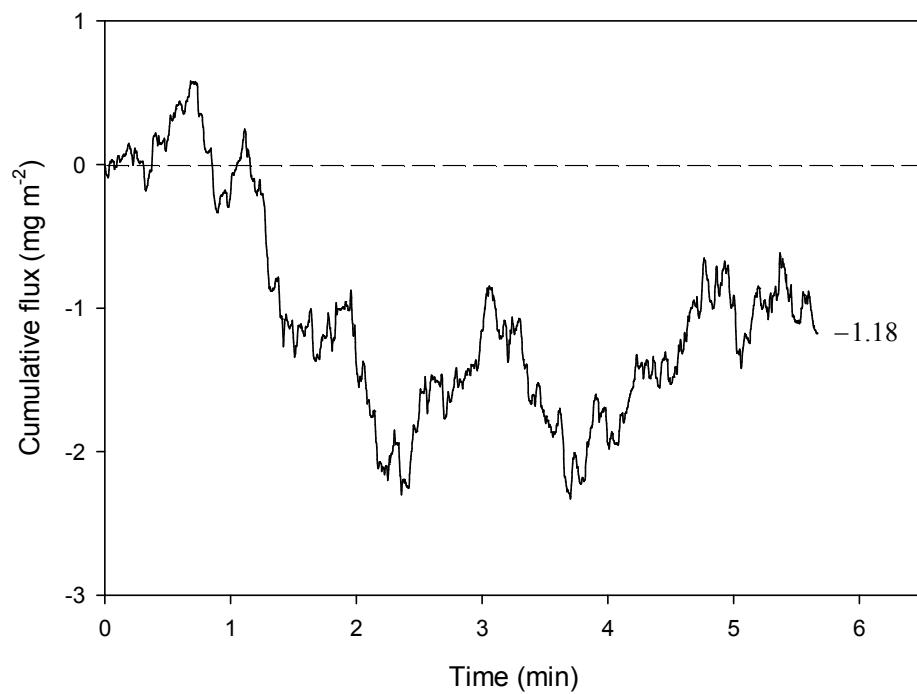
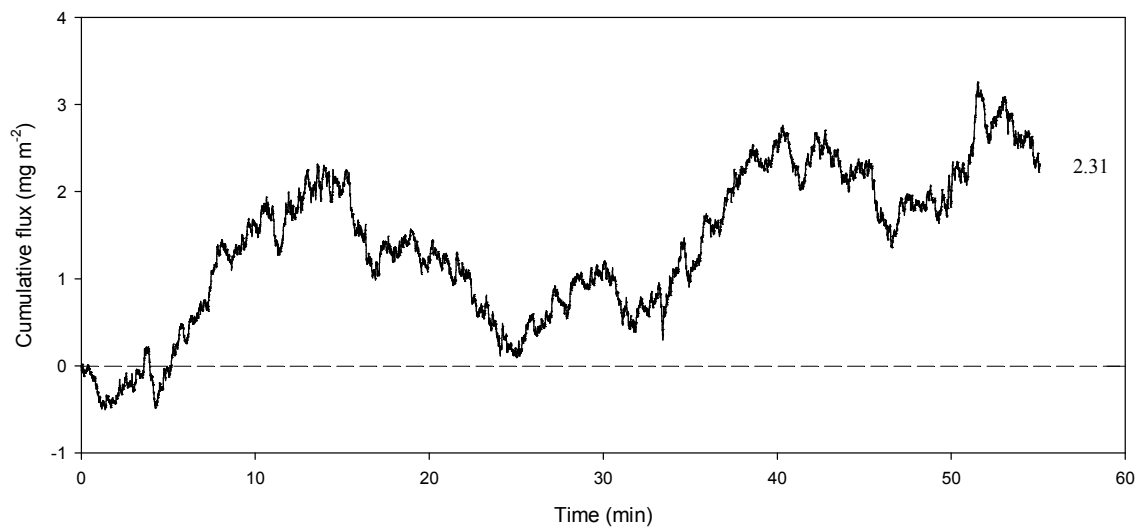


Figure 4.4. Plots of cumulative flux for Squamscott burst. Flux is calculated using (a.) linear regression and (b.) moving average techniques. The value reported at the end of each plot is the cumulative flux (mg m⁻²) for the duration of the burst.

a.



b.

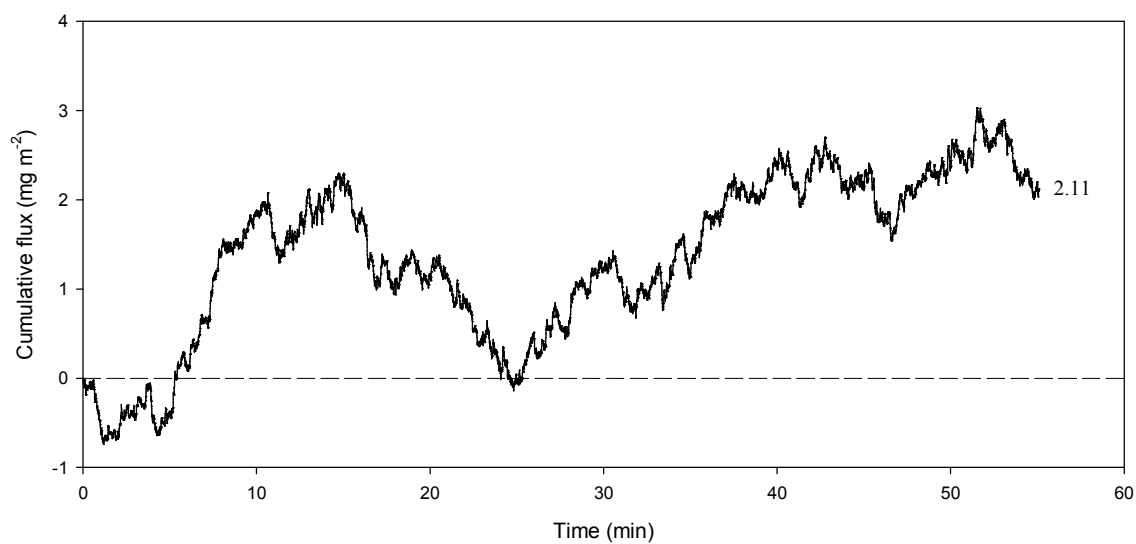
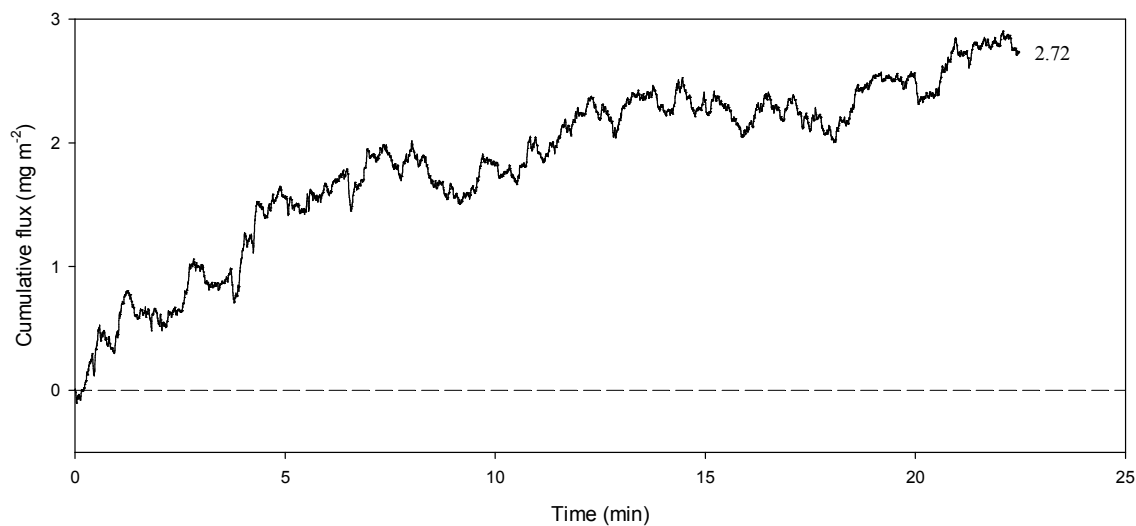


Figure 4.5. Plots of cumulative flux for Kittery flow period burst. Flux is calculated using (a.) linear regression and (b.) moving average techniques. The value reported at the end of each plot is the cumulative flux (mg m⁻²) for the duration of the burst.

a.



b.

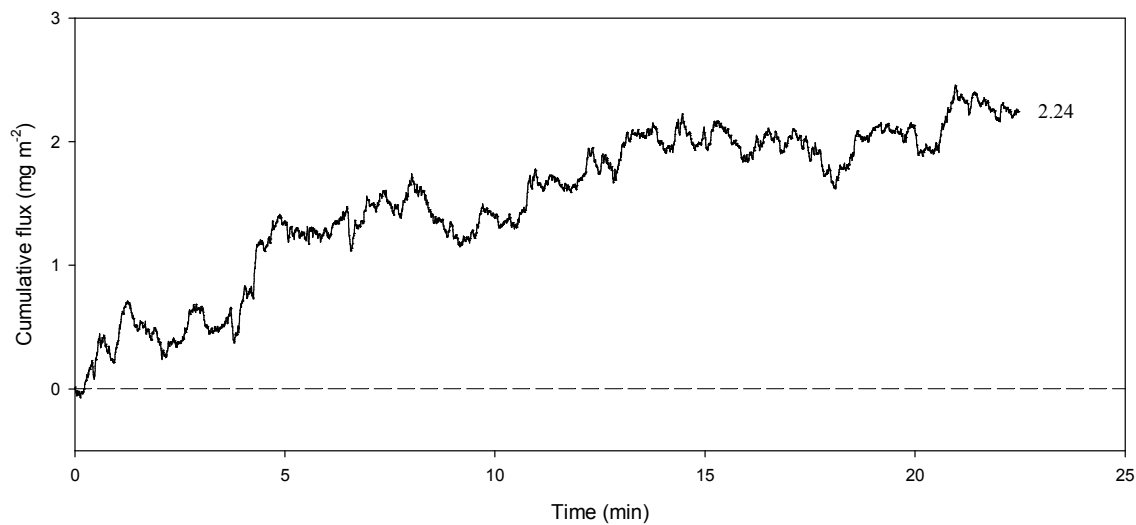


Figure 4.6. Plots of cumulative flux for Kittery ebb period burst. Flux is calculated using (a.) linear regression and (b.) moving average techniques. The value reported at the end of each plot is the cumulative flux (mg m⁻²) for the duration of the burst.

The cumulative flux values from each burst were extrapolated to obtain values of average daily flux, as reported in Table 4.4.

Table 4.4. Average daily DOC flux estimates determined using eddy correlation.

Project Site	Time Range (counts)	Window Length (s)	Average Daily Flux ($\text{mg m}^{-2} \text{d}^{-1}$)	
			Linear Regression	Moving Average
Frankfort	76900-81700	100	-323.3	-352.7
Frankfort	88000-92800	207	-62.6	-304.7
Squamscott	103000-107800	170	-248.9	-299.7
Kittery	8700-37500	174	60.4	55.1
Kittery	127000-141400	337	174.3	143.6
Burton Bog	no acceptable range	-	-	-

With the exception of the second Frankfort burst, the flux values calculated for each site using linear regression and moving average techniques are within about 20% agreement with one another. In all cases, trend removal using the moving average technique led to lower flux estimates, either underestimating positive flux or overestimating the magnitude of negative flux. Kuwae et al. (2006) noted that block averaging techniques can also lead to errors in flux by omitting low-frequency contributions. The large discrepancy between values for the second Frankfort burst illustrates the inability of the moving average technique to adequately model trends over short blocks of data.

The bursts from Frankfort and Squamscott resulted in net negative flux (Table 4.4). Negative flux, indicating transport of DOC from the water column into the sediment, could be indicative of a DOC sink at the sediment surface. A potential mechanism for exchange of DOC from the water column into the sediment is adsorption to sediment iron oxide. The data from Brown (2010) in Tables 3.1 and 3.2 show that iron

oxide was present at Kittery and Squamscott at the sediment surface and at depth. Cores collected at Frankfort in 2006 by Merritt (2007) also showed iron oxide at the surface and at depth. The photos in Figure 4.7 show the presence of iron oxide lining the burrows of macrofauna throughout the sediment profile.



Figure 4.7. Sediment cores collected in Kittery showing rust-colored iron oxide throughout the core and in the burrows of macrofauna.

It is evident from the plots of w and C in Appendix E that even though the three bursts of data from Frankfort and Squamscott were selected by visual inspection, they are not as stationary as the data from the two Kittery bursts. This could lead to artifacts in the flux calculations if trends were not adequately calculated. High variability of the measured DOC concentrations from these two sites exists directly before and after the selected bursts as well.

As mentioned previously, the Frankfort and Squamscott deployment sites were characterized by a high degree of heterogeneity. Extensive vegetation in the intertidal zone was inundated at high tide, releasing DOC into the water column. Riverine flow

likely carried terrestrial DOC from upstream sources not indicative of sediment release. In addition, the Frankfort and Squamscott sites are characterized by significant sediment transport. During preliminary Frankfort test deployments, substantial buildup of sediment occurred on the face of the fluorometer. Beryllium-7 isotope data showed a high degree of sediment mixing at the Squamscott site (Brown, 2010).

During the Kittery flow burst, there are distinct periods of both positive and negative flux within the hour-long burst, as evident from Figure 4.5. To further analyze these trends, cumulative flux was plotted against time (in days) and was separated into five periods of either increasing or decreasing flux, ranging from about 4 min to 17 min. Using least squares linear regression, trend lines were fit to each of these periods (Fig. 4.8). The slope of each line is representative of flux (in $\text{mg m}^{-2} \text{d}^{-1}$).

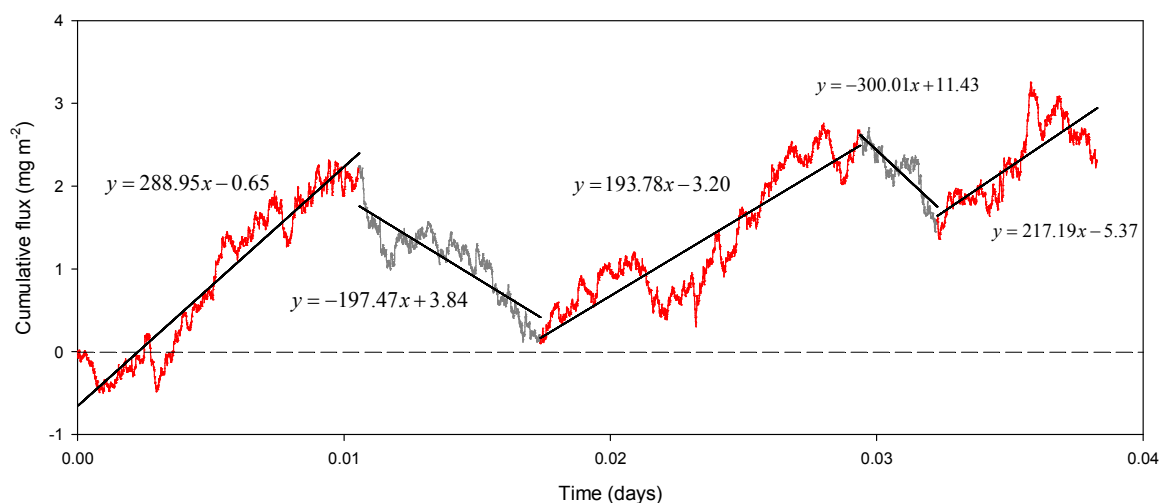


Figure 4.8. Cumulative flux for Kittery flow period burst calculated using linear regression. Trend lines are fit to periods of increasing and decreasing flux.

The average flux from the three positive periods is $233.3 \text{ mg m}^{-2} \text{d}^{-1}$, while the average flux from the two negative periods is $-248.8 \text{ mg m}^{-2} \text{d}^{-1}$. However, the periods of

positive flux account for 75% of the entire burst, leading to a net positive flux over the length of the deployment burst. A possible explanation for the changes between positive and negative flux is that the instrumentation is actually measuring the contribution to flux of different areas of sediment. A previous study determined equations for estimating the upstream elliptical sediment surface area contributing to O₂ flux based on sediment roughness, water depth, and the height of the instrument measurement volume (Berg et al., 2007). It has been shown that both horizontal and vertical velocity change over time and space in estuarine systems during tidal cycles (e.g. Sylaios and Boxall, 1998). Changes in upstream conditions and flow direction would lead to changes in the contributing surface area over time. In addition, Berg et al. (2007) showed that water depth has a significant influence on the size of the contributing footprint, especially at relatively shallow depths such as those present during the Kittery deployment. Therefore, the continuous change in water depth due to tides would lead to a varying area of flux contribution. The changes from positive to negative flux seen during the Kittery tidal flow period could be attributed to the contributing sediment surface area changing from net sources of DOC to net sinks.

There is some degree of high-frequency instrument noise recorded by both the ADV and fluorometer, which could lead to error in flux estimates. According to Berg et al. (2009), high-frequency noise can be quantified as “the difference between two adjacent 8 Hz data points.” Berg et al. (2009) reported that high-frequency noise was greater than the fluctuations of velocity and O₂ concentration, but this did not negatively affect flux estimates because “the noise was randomly distributed around the means.” To test the distribution of noise in DOC flux measurements, w and C noise were plotted in

histograms for each deployment burst and were fit with a Gaussian distribution (Fig. 4.9). Plots for each deployment burst are shown in Appendix F. Linear regression was used to compare the Gaussian fit with the original histogram. In addition, the percent difference between noise above the mean and noise below the mean was calculated to determine if noise skewed results in either a positive or negative direction. Results show that high-frequency noise has little effect ($< 1\%$) on DOC flux calculations, provided that the noise is uncorrelated.

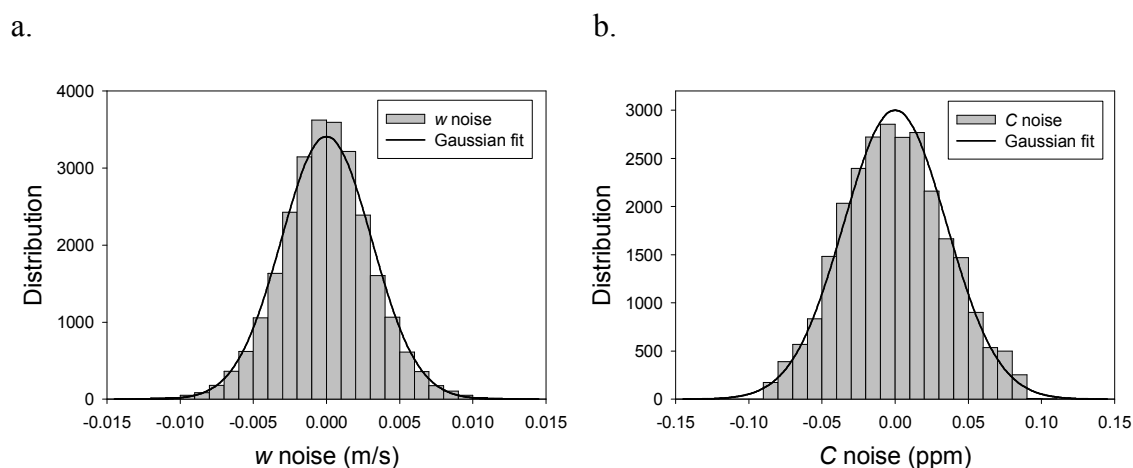


Figure 4.9. Typical distribution of high-frequency noise and Gaussian fit for (a.) vertical velocity and (b.) concentration.

Kuwaie et al. (2006) found that detrending can drastically change total O_2 flux estimates. Results of that study showed that in one case, detrending led to a 94% decrease in flux vs. removal of the statistical mean only. In another case, net flux changed from negative to positive with trend removal. The severity of these discrepancies suggests that not only is trend removal itself important, but the accuracy in establishing the trend for removal is just as crucial. Sharp changes in DOC concentration that occur in the middle of a selected block may be caused by a change in mean

concentration, rather than turbulent fluctuations, and therefore will not adequately be removed by linear regression or a moving average. This could lead to significant artifact in flux estimates. As noted previously, mean velocity and concentration must be stationary in order for trends to be adequately removed (Tennekes & Lumley, 1972).

DOC flux estimates captured using eddy-correlation are an order of magnitude higher than flux values calculated from porewater gradients (Brown, 2010). As mentioned previously, porewater gradients are thought to underestimate the total flux, as they capture only diffusive flux. The results illustrate the ability of eddy-correlation to capture contributions to total flux, such as bioturbation, bioirrigation, and porewater advection. Due to the cohesive nature of the sediments at the three estuarine study sites, porewater advection was likely not a contributing factor to DOC release from between sediment grains. However, advection-induced pressure changes may have led to DOC release from burrows at the sediment surface. In addition, bioturbation and bioirrigation are likely large contributors to DOC release, as evidence of macrofauna was found throughout the sediment column.

4.5. Spectral analysis

Some studies have used spectral analysis to examine aquatic flux measurements in the frequency domain (e.g. Brand et al., 2008; Kuwae et al., 2008). For the purpose of this study, spectral analysis was performed on the data, and flux calculations were reassessed based on the resulting spectra. Other studies generally show that frequencies higher than 1 Hz do not contribute significantly to flux. However, spectral analysis of

DOC flux obtained in this study typically showed significant flux contribution above 1 Hz. Figure 4.10 shows a typical cumulative cospectrum for DOC flux.

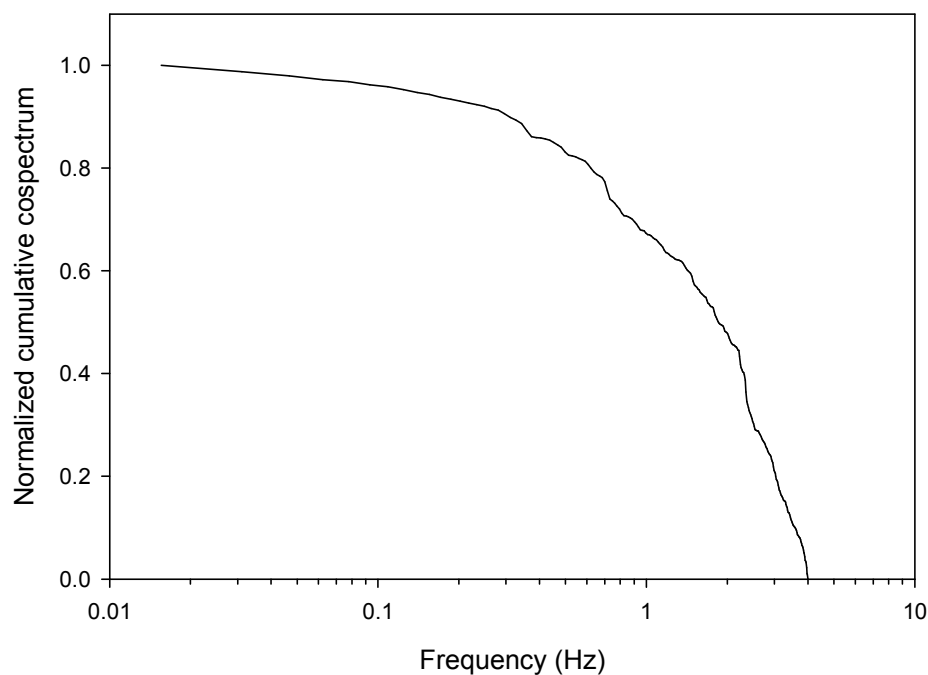
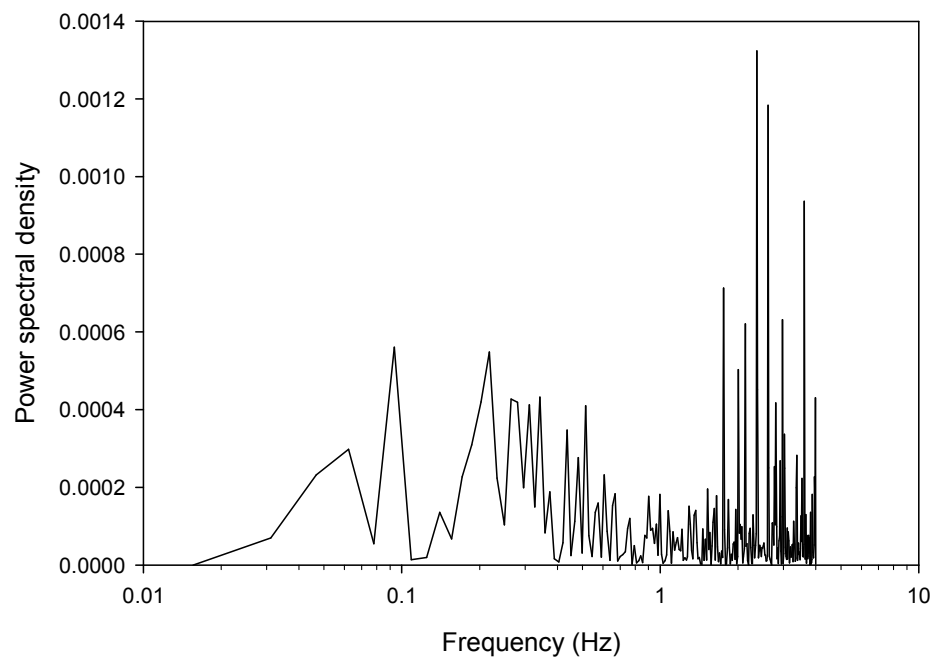


Figure 4.10. Typical normalized cumulative cospectrum (cumulated from the high-frequency end) of w' and C' for a 174-s block of data from the Kittery tidal flow period in which mean values were removed via linear trending.

The significant contribution above \sim Hz is indicative of high-frequency noise. Further investigation of the frequency series of the individual components contributing to flux (w' and C') showed that the high frequency contribution was from C' , while the majority of frequency contribution from w' was less than 1 Hz (Fig. 4.11).

a.



b.

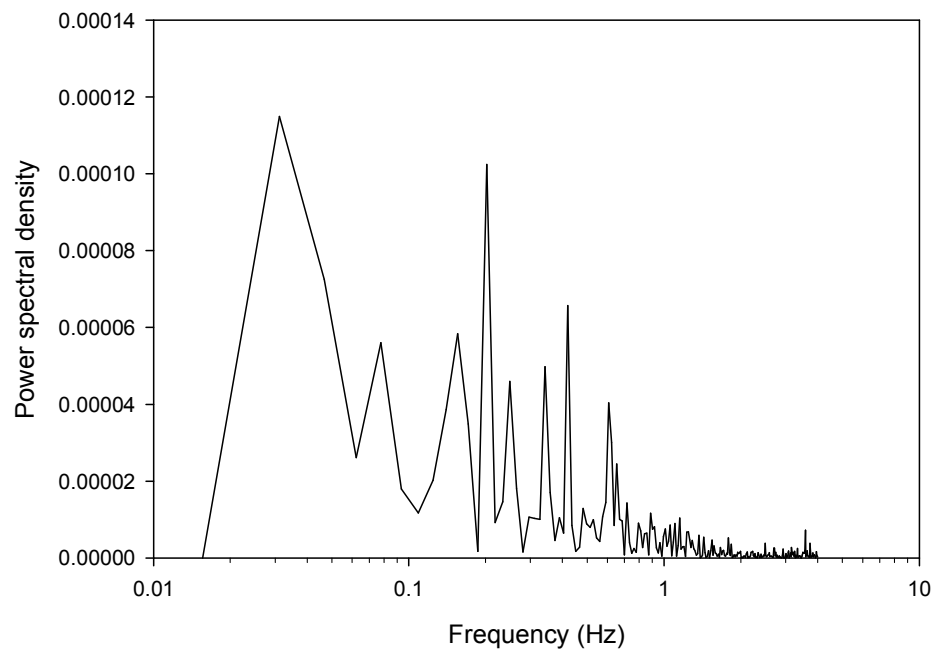


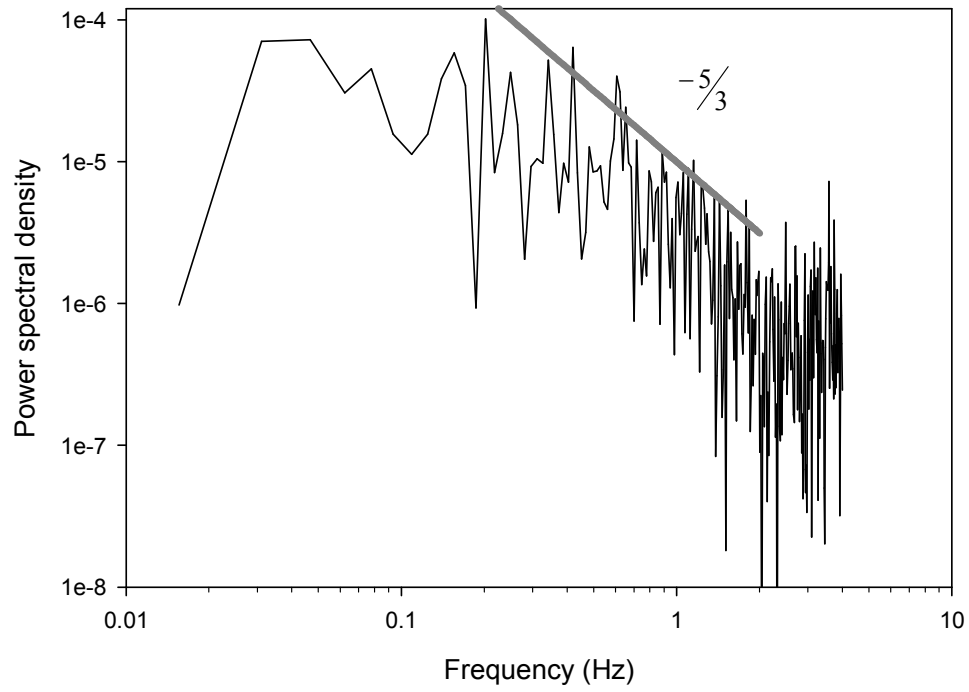
Figure 4.11. Typical spectra for (a.) C' and (b.) w' .

The high signal power in the high-frequency range of C' indicates a contamination of the spectrum, likely due to particles in the fluorometer's light path. Additionally, some contribution to signal power of both C' and w' at frequencies above ~ 1 Hz could be indicative of high-frequency instrument noise, which was determined to be randomly distributed. If the noise is also uncorrelated, it would not contaminate flux estimates.

Kuwae et al. (2006) observed that most w' contribution resided in a frequency band from 0.3-1.4 Hz, and $w'C'$ frequency had peaks in same band, while C' had more even contribution throughout the spectrum, including frequencies above 1 Hz (Fig. 2.2). In DOC flux analysis, $w'C'$ frequency is more similar to C' .

Another approach to examine the frequency domain of flux contribution is to perform spectral analysis on w and cospectral analysis on w and C , as per Brand et al. (2008) (Fig. 4.12). These plots can then be modified to better illustrate the characteristics of turbulent transport. The spectrum of w was filtered and plotted on a log-log scale to determine the frequency range corresponding with the inertial subrange (Fig. 4.13.a), and the cospectrum of w and C was cumulated from the high-frequency end (Fig. 4.13.b). The inertial subrange includes frequencies that represent eddies of intermediate length scales – smaller than energy-containing eddies and larger than viscous eddies (Glickman, 2000). Viscous stress is expected to be small in comparison with Reynolds stress at high Reynolds numbers (Tennekes & Lumley, 1972).

a.



b.

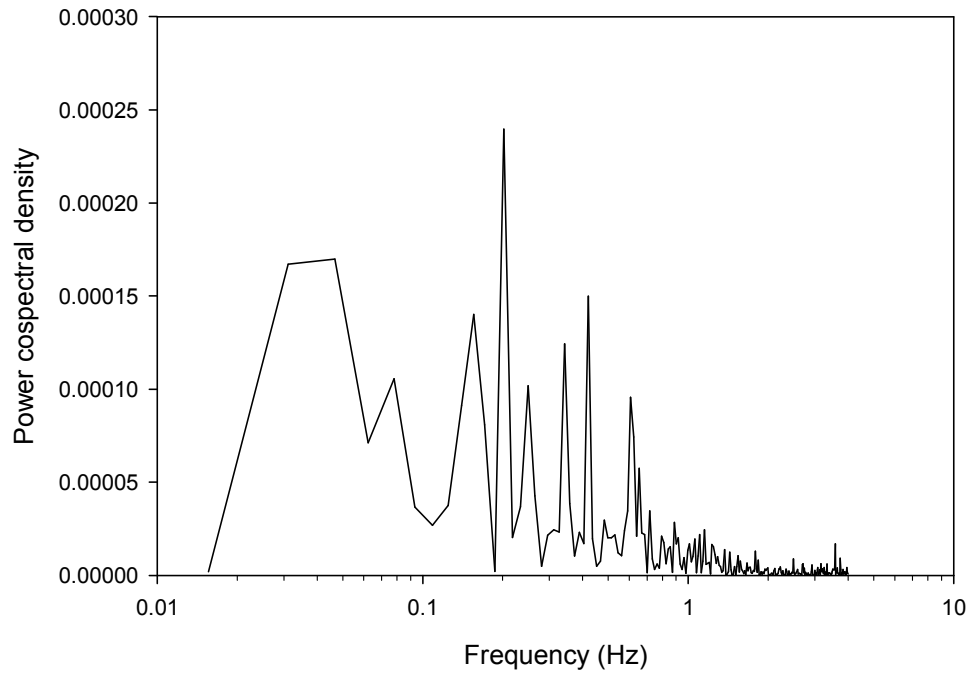


Figure 4.12. (a.) Power spectral density of w , shown with slope of inertial subrange; and (b.) power cospectral density of w and C .

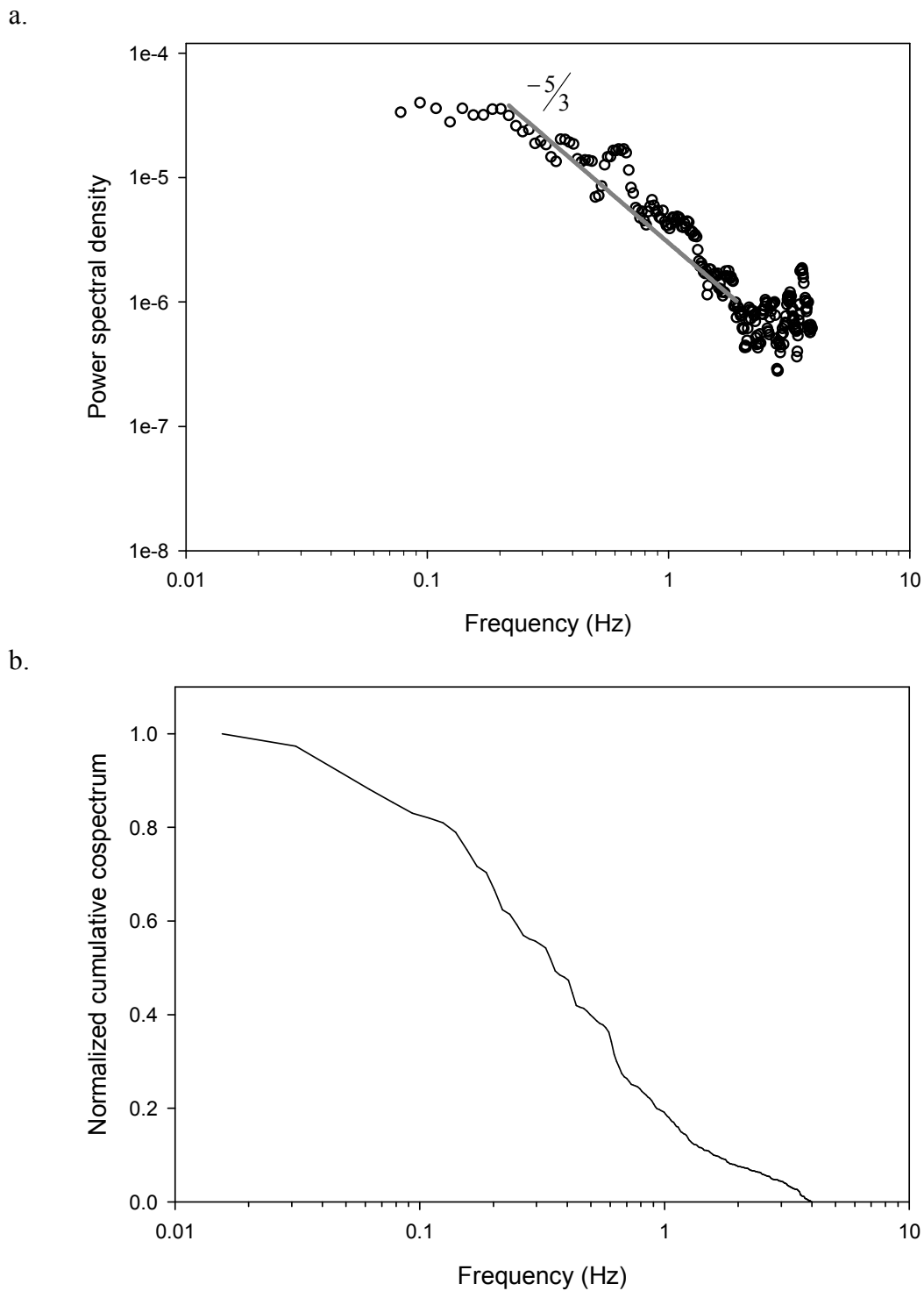


Figure 4.13. (a.) Smoothed power spectral density of w , shown with slope of inertial subrange; and (b.) normalized cumulative cospectrum of w and C , cumulated from the high-frequency end.

The significant difference between cumulative cospectra for $w'C'$ (Fig. 4.10) and wC (Fig. 4.13.b) could illustrate a failure of linear regression to adequately remove trends from DOC concentration data, since spectra for w' and w were similar to each other. The inertial subrange of the velocity spectrum corresponds with the frequency range of ~ 0.2 to 1.7 Hz. The cospectrum of w and C shows the majority of contribution in a similar frequency range. The peaks in the velocity spectrum occurring around 0.6 Hz and 1.1 Hz may be due to wave contamination (Gerbi et al., 2008). Removing the points associated with these jumps greatly increased the correlation between the spectrum and the $-5/3$ slope. This wave contamination may have led to artifact in flux calculation.

To remove the effects of particle-induced high-frequency noise, raw data was low-pass filtered, and flux values were recalculated using linear regression. Since the cutoff of the inertial subrange for w' and the beginning of high-frequency C' noise both occurred at ~ 1.7 Hz, flux was calculated for data low-pass filtered to both 1 Hz and 2 Hz. Results are compared with flux obtained from unfiltered data (Table 4.5).

Table 4.5. Values of average daily flux calculated from data at original sampling frequency and lower frequencies.

Project Site	Time Range (counts)	Window Length (s)	Average Daily Flux ($\text{mg m}^{-2} \text{d}^{-1}$) Calculated Using Linear Regression		
			8 Hz	2 Hz	1 Hz
Frankfort	76900-81700	100	-323.3	-252.3	-235.0
Frankfort	88000-92800	207	-62.6	-37.6	-66.8
Squamscott	103000-107800	170	-248.9	22.9	94.0
Kittery	8700-37500	174	60.4	-73.7	12.0
Kittery	127000-141400	337	174.3	33.3	118.6
Burton Bog	no acceptable range	-	-	-	-

The flux calculated at 2 Hz is expected to include the influence of noise from ~ 1.7 Hz to 2 Hz, which may be highly correlated judging from the considerable differences between flux values at each sampling rate. The flux calculated at 1 Hz is likely omitting some true flux contribution in the 1 Hz to ~ 1.7 Hz range. Plots of cumulative flux calculated using 1 Hz data are shown in Figures 4.14-4.18.

Spectral analysis was also used to look for differences between corrected and uncorrected velocity. Both corrected and uncorrected vertical velocity produced spectra with a similar range of frequencies in the inertial subrange. In addition, the potential effects of the removal of outliers were tested for by computing cumulative cospectra for $w'C'$ with no outliers removed. The removal of outliers appeared to have little effect on the cumulative cospectra.

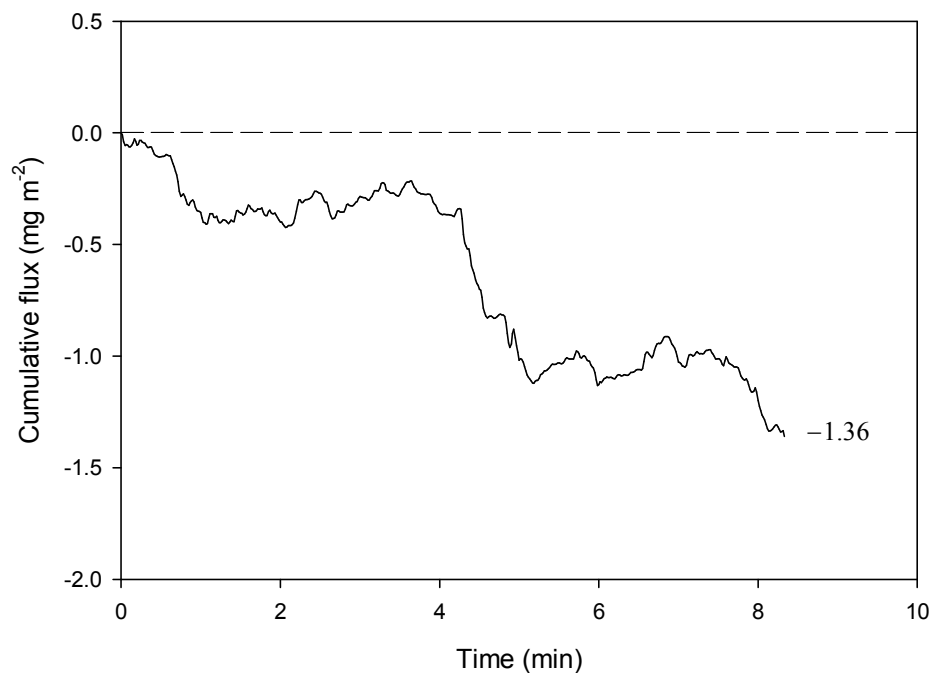


Figure 4.14. Plot of cumulative flux for Frankfort burst 1 at 1 Hz calculated using linear regression. The value reported at the end of the plot is the cumulative flux (mg m^{-2}) for the duration of the burst.

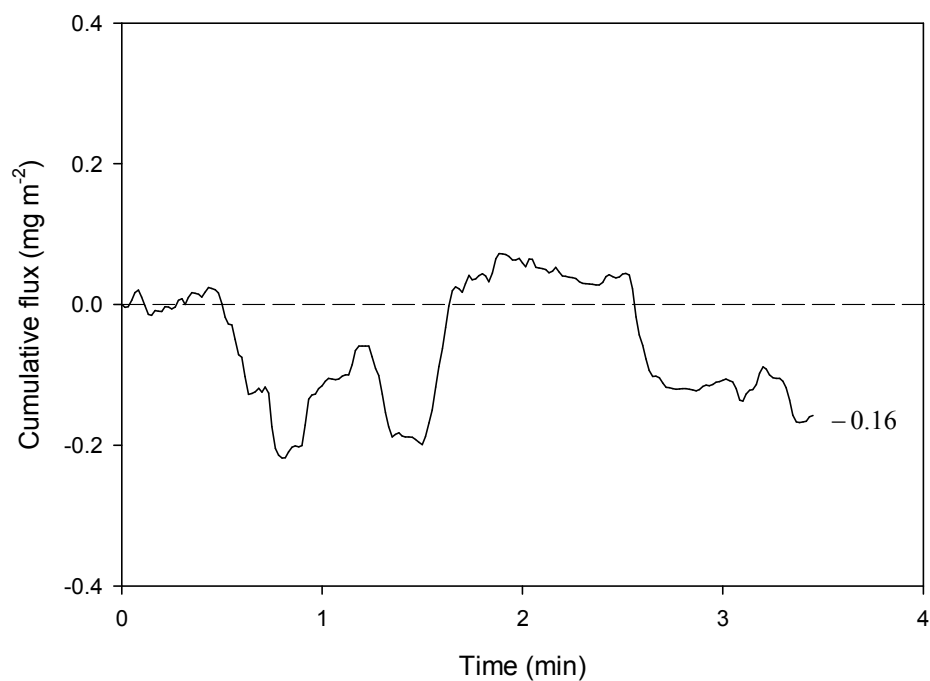


Figure 4.15. Plot of cumulative flux for Frankfort burst 2 at 1 Hz calculated using linear regression. The value reported at the end of the plot is the cumulative flux (mg m^{-2}) for the duration of the burst.

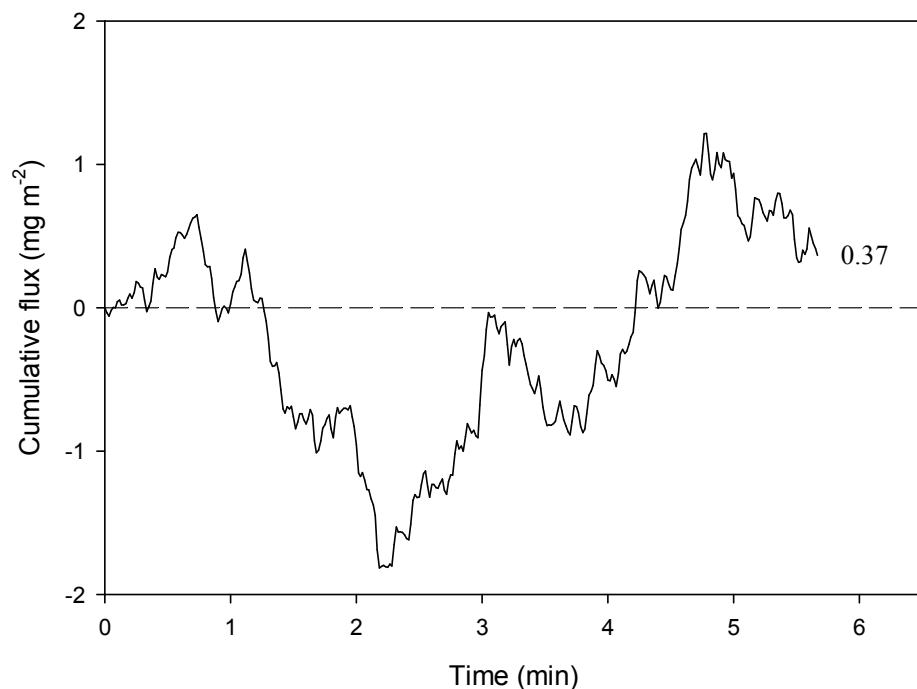


Figure 4.16. Plot of cumulative flux for Squamscott burst (low-pass filtered to 1 Hz) using linear regression. The value reported at the end of the plot is the cumulative flux (mg m^{-2}) for the duration of the burst.

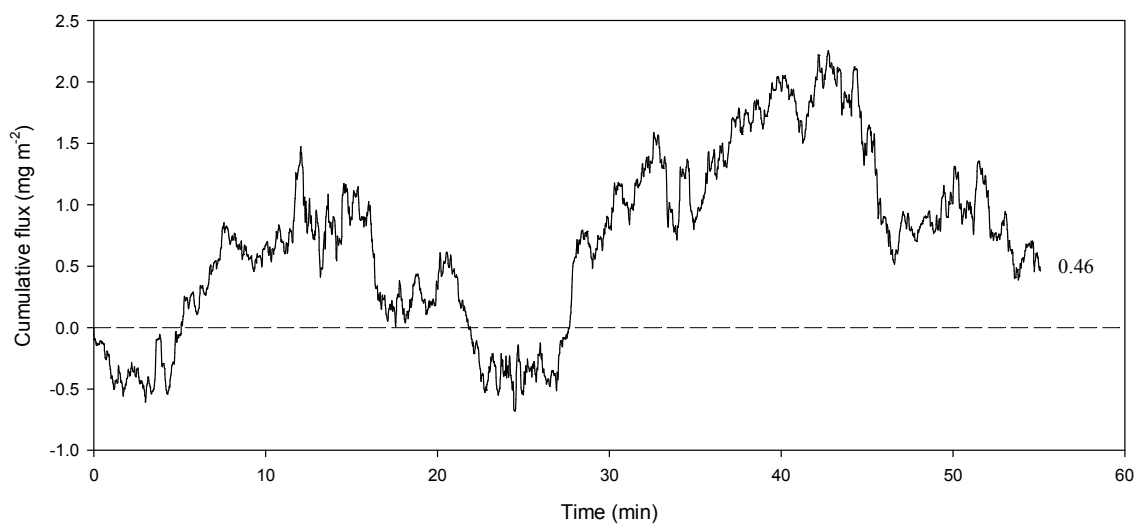


Figure 4.17. Plot of cumulative flux for Kittery flow period burst at 1 Hz calculated using linear regression. The value reported at the end of the plot is the cumulative flux (mg m^{-2}) for the duration of the burst.

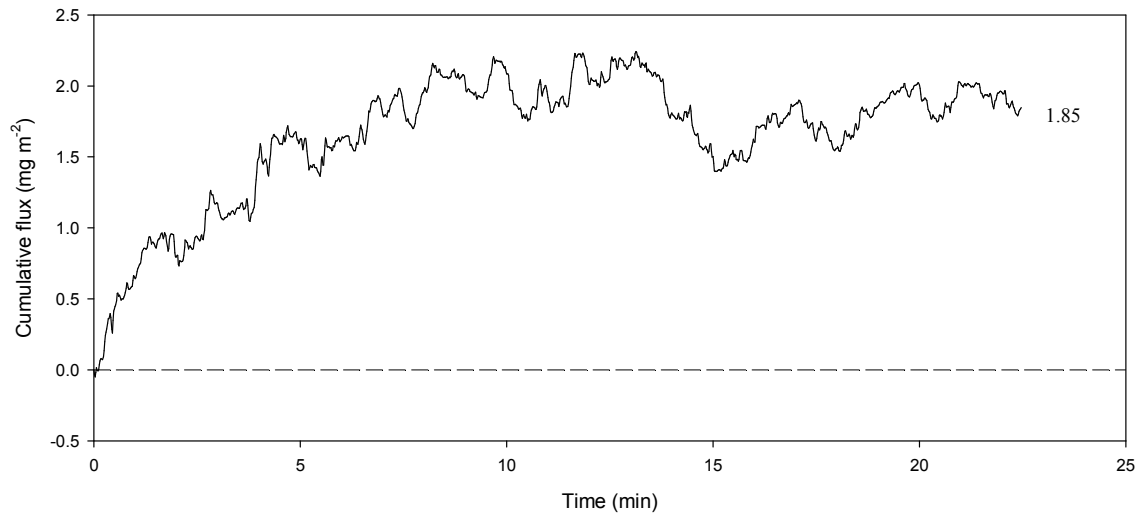


Figure 4.18. Plot of cumulative flux for Kittery ebb period burst at 1 Hz calculated using linear regression. The value reported at the end of the plot is the cumulative flux (mg m^{-2}) for the duration of the burst.

Chapter 5

SUMMARY AND CONCLUSIONS

In this study, the eddy correlation technique was utilized to quantify vertical benthic DOC flux in estuarine environments. DOC is a concern in these systems due to its ability to mobilize contaminants and create disinfection byproducts during water treatment. Methods were developed based on physical transport theories and previous aquatic eddy correlation studies. Eddy correlation offers benefits over other DOC flux measurement techniques by providing a non-invasive, *in situ* technique for measuring continuous vertical benthic flux. The results of this study demonstrate the potential of the eddy correlation technique for measurement of DOC flux from estuarine sediments.

Results indicate that benthic DOC flux may vary considerably over short time scales. Eddy correlation provides a method for monitoring short-term dynamics of flux, as well as variations on diurnal and seasonal scales. The magnitudes of DOC flux calculated using the eddy correlation technique were an order of magnitude larger than those calculated from porewater gradients obtained from sediment core centrifugation. These values are reasonable, since porewater gradients, which only capture diffusive flux, are expected to underestimate total benthic flux.

In heterogeneous environments such as the systems studied here, it is important, yet challenging, to decouple turbulent eddy flux from large-scale advective flux, as large-scale advective flow carries DOC and freshwater into the instrument measurement volume. Therefore, the instrumentation captures DOC inputs not only from sediment release, but also from upstream sources, which contaminate the eddy flux measurements.

This is especially the case in tidal systems, where inundation of estuarine vegetation can lead to increased production, which might not be indicative of sediment DOC release. The Kittery deployment site was characterized by less heterogeneity than the other estuarine sites, and DOC concentrations were relatively stationary over significant periods of time, making eddy correlation more feasible. Flux estimates may also have been contaminated by suspended particles contributing to noise in CDOM fluorometer measurements.

Since this is the first study to use eddy correlation for benthic DOC flux estimation, further development is necessary to improve methods and verify flux measurements. Recommendations for future work are as follows:

1. A large-scale laboratory chamber should be built for use in validating flux. This chamber should include a sediment layer and overlying water in which turbulent fluctuations can be induced. The eddy correlation instruments can be deployed in the chamber, and DOC concentration in the overlying water can be measured over time to obtain flux estimates for comparison.
2. An alternative method should be developed for selecting usable bursts of data, utilizing statistical methods to determine the stationarity of w and C , rather than visual inspection.
3. Since mean flows are not always steady in the environments studied here, there is high likelihood of wave contamination. Therefore, separation of wave

contribution along with turbulent fluctuations from mean flows should be investigated. This may be made possible by calculating flux directly from the spectra or via modeling techniques (Gerbi et al., 2008).

4. The effects of particle attenuation on CDOM fluorometer readings should be investigated further to determine the influence on eddy flux estimates. In addition, measurement techniques could be modified to reduce the influence of particles on CDOM readings. Other studies have used flow-through meters with in situ filters to measure optical properties in aquatic systems (e.g. Downing et al., 2009).

REFERENCES

- Alperin, M.J., Albert, D.B., and Martens, C.S. 1994. Seasonal variations in production and consumption rates of dissolved organic carbon in an organic-rich coastal sediment. *Geochimica et Cosmochimica Acta*. 58: 4909-4930.
- Benoit, J.M., Gilmour, C.C., Heyes, A., Mason, R.P., and Miller, C.L. 2003. Geochemical and biological controls over methylmercury production and degradation in aquatic ecosystems. In Cai, Y. and Braids, O.C. *Biogeochemistry of Environmentally Important Trace Elements* (pp. 262-297). American Chemical Society: Washington, DC.
- Berg, P., Glud, R.N., Hume, A., Stahl, H., Oguri, K., Meyer, V., and Kitazato, H. 2009. Eddy correlation measurements of oxygen uptake in deep ocean sediments. *Limnology and Oceanography: Methods*. 7: 576-584.
- Berg, P., Roy, H., Janssen, F., Meyer, V., Jørgensen, B.B., Huettel, M., and de Beer, D. 2003. Oxygen uptake by aquatic sediments measured with a novel non-invasive eddy-correlation technique. *Marine Ecology Progress Series*. 261: 75-83.
- Berg, P., Røy, H., and Wiberg, P.L. 2007. Eddy correlation flux measurements: The sediment surface area that contributes to the flux. *Limnology and Oceanography*. 52: 1672-1684.
- Blough, N.V. and Del Vecchio, R. 2002. Chromophoric DOM in the coastal environment. In Hansell, D.A. and Carlson, C.A. (Eds.) *Biogeochemistry of Marine Dissolved Organic Matter* (pp. 509-546). Academic Press: San Diego, CA.
- Boudreau, B.P. 2001. Solute transport above the sediment-water interface. In Boudreau, B.P. and Jørgensen, B.B. (Eds.) *The Benthic Boundary Layer: Transport Processes and Biogeochemistry* (pp. 104-126). Oxford University Press: Oxford.
- Brand, A., McGinnis, D.F., Wehrli, B., and Wüest, A. 2008. Intermittent oxygen flux from the interior into the bottom boundary of lakes as observed by eddy correlation. *Limnology and Oceanography*. 53: 1997-2006.
- Brown, L.E. 2010. Sedimentary mercury dynamics at two estuarine mudflats in Great Bay, New Hampshire. Master's Thesis, University of Maine, Orono. 88 pp.
- Bukata, R.P., Jerome, J.H., Kondratyev, K.Y., and Pozdnyakov, D.V. 1995. *Optical Properties and Remote Sensing of Inland and Coastal Waters*. CRC Press: Boca Raton, FL.
- Burdige, D.J. 2006. *Geochemistry of Marine Sediments*. Princeton University Press: Princeton, NJ. 609 pp.

- Burdige, D.J. and Homstead, J. 1994. Fluxes of dissolved organic carbon from Chesapeake Bay sediments. *Geochimica et Cosmochimica Acta*. 58: 3407-3424.
- Carignan, R., Rapin, F., and Tessier, A. 1985. Sediment porewater sampling for metal analysis: A comparison of techniques. *Geochimica et Cosmochimica Acta*. 49: 2493-2497.
- Carignan, R., St-Pierre, S., and Gächter, R. 1994. Use of diffusion samplers in oligotrophic lake sediments: Effects of free oxygen in sampler material. *Limnology and Oceanography*. 39: 468-474.
- Carlson, C.A. 2002. Production and removal processes. In Hansell, D.A. and Carlson, C.A. (Eds.) *Biogeochemistry of Marine Dissolved Organic Matter* (pp. 91-151). Academic Press: San Diego, CA.
- Chen, R.F., Bissett, P., Coble, P., Conmy, R., Gardner, G.B., Moran, M.A., Wang, X., Wells, M.L., Whelan, P., and Zepp, R.G. 2004. Chromophoric dissolved organic matter (CDOM) source characterization in the Louisiana Bight. *Marine Chemistry*. 89: 257-272.
- Cauwet, G. 2002. DOM in the coastal zone. In Hansell, D.A. and Carlson, C.A. (Eds.) *Biogeochemistry of Marine Dissolved Organic Matter* (pp. 579-609). Academic Press: San Diego, CA.
- Crusius, J., Berg, P., Koopmans, D.J., and Erban, L. 2008. Eddy correlation measurements of submarine groundwater discharge. *Marine Chemistry*. 109: 77-85.
- Downing, B.D., Boss, E., Bergamaschi, B.A., Fleck, J.A., Lionberger, M.A., Ganju, N.K., Schoellhamer, D.H., and Fujii, R. 2009. Quantifying fluxes and characterizing compositional changes of dissolved organic matter in aquatic systems *in situ* using combined acoustic and optical measurements. *Limnology and Oceanography: Methods*. 7: 119-131.
- Dyer, A.J. 1961. Measurement of evaporation and heat transfer in the lower atmosphere by an automatic eddy-correlation technique. *Quarterly Journal of the Royal Meteorological Society*. 87: 401-412.
- Dyer, A.J. and Hicks, B.B. 1967. The Fluxatron – A revised approach to the measurement of eddy fluxes in the lower atmosphere. *Journal of Applied Meteorology*. 6: 408-413.
- Dyer, A.J. and Maher, F.J. 1965. Automatic eddy-flux measurement with the Evapotron. *Journal of Applied Meteorology*. 4: 622-625.
- Dyer, A.J. and Pruitt, W.O. 1962. Eddy-flux measurements over a small, irrigated area. *Journal of Applied Meteorology*. 1: 471-473.

- Eastman, J.A. and Stedman, D.H. 1977. A fast response sensor for ozone eddy-correlation flux measurements. *Atmospheric Environment*. 11: 1209-1211.
- Emery, W.J. and Thomson, R.E. 2001. *Data Analysis Methods in Physical Oceanography: Second and Revised Edition*. Elsevier: Amsterdam. 638 pp.
- Everitt, B.S. (ed.) 2006. *The Cambridge Dictionary of Statistics: Third Edition*. Cambridge University Press: Cambridge. 444 pp.
- Fleck, J.A., Fram, M.S., and Fujii, R. 2007. Organic carbon and disinfection byproduct precursor loads from a constructed, non-tidal wetland in California's Sacramento-San Joaquin Delta. *San Francisco Estuary and Watershed Science*. 5: 24 pp.
- Gerbi, G.P., Trowbridge, J.H., Edson, J.B., Plueddemann, A.J., Terray, E.A., and Fredericks, J.J. 2008. Measurements of momentum and heat transfer across the air-sea interface. *Journal of Physical Oceanography*. 38: 1054-1072.
- Glickman, T.S. (ed.) 2000. *Glossary of Meteorology: Second Edition*. American Meteorological Society: Boston, MA. 850 pp.
- Ham, R. van der, Kranenburg, C., and Winerwerp, J.C. 1998. Turbulent vertical exchange of fine sediments in stratified tidal flows. In Dronkers, J. and Scheffers, M.B.A.M. (Eds.) *Physics of Estuaries and Coastal Seas* (pp. 201-207). Balkema: Rotterdam.
- Hesslein, R.H. 1976. An in situ sampler for close interval pore water studies. *Limnology and Oceanography*. 21: 912-914.
- Hicks, B.B. 1970. The measurement of atmospheric fluxes near the surface: A generalized approach. *Journal of Applied Meteorology*. 9: 386-388.
- Huettel, M. and Webster, I.T. 2001. Porewater flow in permeable sediments. In Boudreau, B.P. and Jørgensen, B.B. (Eds.) *The Benthic Boundary Layer: Transport Processes and Biogeochemistry* (pp. 144-179). Oxford University Press: Oxford.
- Janssen, F., Faerber, P., Huettel, M., Meyer, V., and Witte, U. 2005. Pore-water advection and solute fluxes in permeable marine sediments (I): Calibration and performance of the novel benthic chamber system *Sandy*. *Limnology and Oceanography*. 50: 768-778.
- Jones, E.P., Ward, T.V., and Zwick, H.H. 1978. A fast response atmospheric CO₂ sensor for eddy correlation flux measurements. *Atmospheric Environment*. 12: 845-851.
- Kalbitz, K., Popp, P., Geyer, W., and Hanschmann, G. 1997. β -HCH mobilization in polluted wetland soils as influenced by dissolved organic matter. *The Science of the Total Environment*. 204: 37-48.

Kuwae, T., Kamio, K., Inoue, T., Miyoshi, E., and Uchiyama, Y. 2006. Oxygen exchange flux between sediment and water in an intertidal sandflat, measured *in situ* by the eddy-correlation method. *Marine Ecology Progress Series*. 307: 59-68.

Lahajnar, N., Rixen, T., Gaye-Haake, B., Schäfer, P., and Ittekkot, V. 2005. Dissolved organic carbon (DOC) fluxes of deep-sea sediments from the Arabian Sea and NE Atlantic. *Deep-Sea Research II*. 52: 1947-1964.

Laws, E. 1997. *Mathematical Methods for Oceanographers: An Introduction*. John Wiley & Son, Inc.: New York. 343 pp.

Maier, R.M., Pepper, I.L., and Gerba, C.P. 2009. *Environmental Microbiology: Second Edition*. Academic Press: Burlington, MA. 598 pp.

McGinnis, D.F., Berg, P., Brand, A., Lorrain, C., Edmonds, T.J., and Wüest, A. 2008. Measurement of eddy correlation oxygen fluxes in shallow freshwaters: Toward routine applications and analysis. *Geophysical Research Letters*. 35: L04403.

Merritt, K.A. 2007. Mercury dynamics in sulfide-rich sediments: Geochemical influence on contaminant mobilization and methylation within the Penobscot River Estuary, Maine, USA. Ph.D. Dissertation, University of Maine, Orono. 172 pp.

Merritt, K.A. and Amirbahman, A. 2007. Mercury dynamics in sulfide-rich sediments: Geochemical influence on contaminant mobilization within the Penobscot River estuary, Maine, USA. *Geochimica et Cosmochimica Acta*. 71: 929-941.

Merritt, K.A. and Amirbahman, A. 2008. Methylmercury cycling in estuarine sediment pore waters (Penobscot River estuary, Maine, USA). *Limnology and Oceanography*. 53: 1064-1075.

Reimers, C.E., Jahnke, R.A., and Thomsen, L. 2001. In situ sampling in the benthic boundary layer. In: B.P. Boudreau and B.B. Jørgensen (eds.). *The Benthic Boundary Layer* (pp. 245-268). Oxford University Press.

Reynolds, O. 1895. On the dynamical theory of incompressible viscous fluids and the determination of the criterion. *Philosophical Transactions of the Royal Society of London A*. 186: 123-164.

Shirasawa, K., Ingram, R.G., and Hudier, E.J.-J. 1997. Ocean heat fluxes under thin sea ice in Saroma-ko Lagoon, Hokkaido, Japan. *Journal of Marine Systems*. 11: 9-19.

Swinbank, W.C. 1951. The measurement of vertical transfer of heat and water vapor by eddies in the lower atmosphere. *Journal of Meteorology*. 8: 135-145.

Sylaios, G. and Boxall, S.R. 1998. Circulation and mixing of a partially-mixed estuary. In Dronkers, J. and Scheffers, M.B.A.M. (Eds.) *Physics of Estuaries and Coastal Seas* (pp. 47-61). Balkema: Rotterdam.

Tengberg, A. et al. 1995. Benthic chamber and profiling landers in oceanography – A review of design, technical solutions and functioning. *Progress in Oceanography*. 35: 253-294.

Tennekes, H. and Lumley, J.L. 1972. *A First Course in Turbulence*. MIT Press: Cambridge, MA. 300 pp.

Wesely, M.L, Hicks, B.B., Dannevik, W.P., Frisella, S., and Husar, R.B. 1977. An eddy-correlation measurement of particulate deposition from the atmosphere. *Atmospheric Environment*. 11: 561-563.

West, J.R. and Oduyemi, O.K. 1989. Turbulence measurements of suspended solids concentration in estuaries. *Journal of Hydraulic Engineering*. 115: 457-474.

APPENDICES

Appendix A: MATLAB code

```

%flux_calc
%Emmanuel Boss, U. of Maine, Dec. 2004
%Modified version, M.P. Swett, April 2010

%read in data
clear all
close all
A=load('kitt_0903.txt');

%lowpass filter to 1 Hz
for i=1:18
    AA(:,i)=filtfilt(ones(1,8)/8,1,A(:,i));
end
clear 'A'
A=AA;

%transform 'counts' column into continuous set
B=size(A(:,2));
B=B(1);
B=1:B;
A(:,2)=B;

A(:,19)=(A(:,6)+A(:,7)+A(:,8))/3;
A(:,20)=10.^(0.043.*A(:,19));
A(:,20)=A(:,20)-10.^(0.043*min(A(:,19)));

S=3;

%identify count starting point
C=9396;
%identify count end point
D=C+1392;

START=C;
BLOCK=D-C;

%read in data
mean_p=A(C:D,15)';
mean_amp=((A(C:D,6)+A(C:D,7)+A(C:D,8))/3)';
mean_CDOM=A(C:D,16)';
mean_CDOM=(mean_CDOM-133.6)/267.03;
mean_u=A(C:D,3)';
mean_v=A(C:D,4)';
mean_w=A(C:D,5)';
mean_amp_lin=10.^(0.043.*mean_amp)-10.^(0.043.*min(mean_amp));

```



```

%linear regression using least squares
R1(:,1)=C:D; %counts
R1(:,2)=mean_CDOM; %CDOM
FitCoeff=polyfit(R1(:,1),R1(:,2),1); % c1, c2
R1(:,3)=R1(:,1)*FitCoeff(1,1)+FitCoeff(1,2); % c bar
R1(:,4)=R1(:,2)-R1(:,3); % c'

%removes mean to get C', p', and amp'
p_p=(A(C:D,15)-mean(A(C:D,15)))';
amp_p=((A(C:D,6)+A(C:D,7)+A(C:D,8))/3-
mean(A(C:D,6)+A(C:D,7)+A(C:D,8)))';
CDOM_p=R1(:,4)';

%finds the angle that maximizes the variance in one direction in the
%horizontal
phi=0.5*atan(sum(2*mean_u.*mean_v)/(sum(mean_u.^2)-sum(mean_v.^2)));
mean_u_new=mean_u*cos(phi)+mean_v*sin(phi);
mean_v_new=-mean_u*sin(phi)+mean_v*cos(phi);

u_new=A(C:D,3)*cos(phi)+A(C:D,4)*sin(phi);
v_new=A(C:D,4)*cos(phi)-A(C:D,3)*sin(phi);

%finds the angle that minimizes the variance in the vertical
theta=0.5*atan(sum(2*mean_v_new.*mean_w)/sum(mean_v_new.^2-mean_w.^2));
mean_w_new=-mean_v_new*sin(theta)+mean_w*cos(theta);
mean_v_new_b=mean_v_new*cos(theta)+mean_w*sin(theta);

w_new=-v_new*sin(theta)+A(C:D,5)*cos(theta);
v_new_b=v_new*cos(theta)+A(C:D,5)*sin(theta);

%finds the angle that minimizes the variance in the vertical
theta2=0.5*atan(sum(2*mean_u_new.*mean_w_new)/sum(mean_u_new.^2-
mean_w_new.^2));
mean_w_new_b=-mean_u_new*sin(theta2)+mean_w_new*cos(theta);
mean_u_new_b=mean_u_new*cos(theta2)+mean_w_new*sin(theta);

w_new_b=-u_new*sin(theta2)+w_new*cos(theta2);
u_new_b=u_new*cos(theta2)+w_new*sin(theta2);

%rows to columns
u_new=(u_new)';
v_new=(v_new)';
w_new=(w_new)';
v_new_b=(v_new_b)';
u_new_b=(u_new_b)';
w_new_b=(w_new_b)';

%velocity linear regression using least squares
R1(:,5)=w_new_b;
FitCoeff2=polyfit(R1(:,1),R1(:,5),1); % c1, c2
R1(:,6)=R1(:,1)*FitCoeff2(1,1)+FitCoeff2(1,2); % w bar
R1(:,7)=R1(:,5)-R1(:,6); %w'

```

```

%flux calculations
u_p=u_new_b-mean(u_new_b);
v_p=v_new_b-mean(v_new_b);
w_p=R1(:,7)';

uu=(u_p.*u_p);
vv=(v_p.*v_p);
ww=(w_p.*w_p);
uv=(u_p.*v_p);
vw=(v_p.*w_p);
wu=(w_p.*u_p);
uCDOM=(u_p.*CDOM_p);
vCDOM=(v_p.*CDOM_p);
wCDOM=(w_p.*CDOM_p);
uamp=(u_p.*amp_p);
vamp=(v_p.*amp_p);
wamp=(w_p.*amp_p);

%remove bad w'C' data
WCSP=mean(wCDOM)+std(wCDOM)*S;
WCSM=mean(wCDOM)-std(wCDOM)*S;
WCSUBP=0;
WCSUBM=0;

for n=1:BLOCK
if wCDOM(1,n)>WCSP
    wCDOM(1,n)=WCSUBP;
elseif wCDOM(1,n)<WCSM
    wCDOM(1,n)=WCSUBM;
end
end

%final data matrix
R(:,1)=C:D; %counts
R(:,2)=(R(:,1)-R(1,1))/(8*3600*24); %time (days)
R(:,3)=R(:,2)*1440; %time (min)
R(:,4)=w_new_b; %corrected vert. vel. (w)
R(:,5)=R1(:,6); %vert. vel. trend (w bar)
R(:,6)=w_p'; %w'
R(:,7)=mean_CDOM; %C
R(:,8)=R1(:,3); %C bar
R(:,9)=CDOM_p'; %C'
R(:,10)=wCDOM*86400000; %w'c' flux
R(:,11)=cumtrapz(R(:,2),R(:,10)); %cumulative flux (mg m-2)

%spectral analysis using periodogram
%w'C' cospectrum + cumulative
P(:,1)=(1:(512/2+1))*4/(512/2+1); %frequency
%P(:,2)=periodogram((R(:,6)).*R(:,9)), [], 'onesided', 512, 8); %Power/Freq
P(:,2)=periodogram((R(:,10))/86400000), [], 'onesided', 512, 8); %Power/Freq
P(:,2)=flipud(P(:,2));
P(:,3)=cumtrapz(P(:,2));
P(:,2)=flipud(P(:,2));
P(:,3)=flipud(P(:,3));
P(:,3)=P(:,3)./P(1,3); %Normalized cum. cospectrum

```

```

%wC cospectrum
P(:,4)=periodogram((R(:,4).*R(:,7)), [], 'onesided', 512, 8); %Power/Freq
P(:,4)=flipud(P(:,4));
P(:,5)=cumtrapz(P(:,4));
P(:,4)=flipud(P(:,4));
P(:,5)=flipud(P(:,5));
P(:,5)=P(:,5)./P(1,5); %Normalized cum. cospectrum

%w spectrum
P(:,6)=periodogram(R(:,4), [], 'onesided', 512, 8); %Power/Freq
P(:,6)=flipud(P(:,6));
P(:,7)=cumtrapz(P(:,6));
P(:,6)=flipud(P(:,6));
P(:,7)=flipud(P(:,7));
P(:,7)=P(:,7)./P(1,7); %Normalized cum. cospectrum

%C spectrum
P(:,8)=periodogram(R(:,7), [], 'onesided', 512, 8); %Power/Freq
P(:,8)=flipud(P(:,8));
P(:,9)=cumtrapz(P(:,8));
P(:,8)=flipud(P(:,8));
P(:,9)=flipud(P(:,9));
P(:,9)=P(:,9)./P(1,9); %Normalized cum. cospectrum

%w' spectrum
P(:,10)=periodogram(R(:,6), [], 'onesided', 512, 8); %Power/Freq
P(:,10)=flipud(P(:,10));
P(:,11)=cumtrapz(P(:,10));
P(:,10)=flipud(P(:,10));
P(:,11)=flipud(P(:,11));
P(:,11)=P(:,11)./P(1,11); %Normalized cum. cospectrum

%C' spectrum
P(:,12)=periodogram(R(:,9), [], 'onesided', 512, 8); %Power/Freq
P(:,12)=flipud(P(:,12));
P(:,13)=cumtrapz(P(:,12));
P(:,12)=flipud(P(:,12));
P(:,13)=flipud(P(:,13));
P(:,13)=P(:,13)./P(1,13); %Normalized cum. cospectrum

```

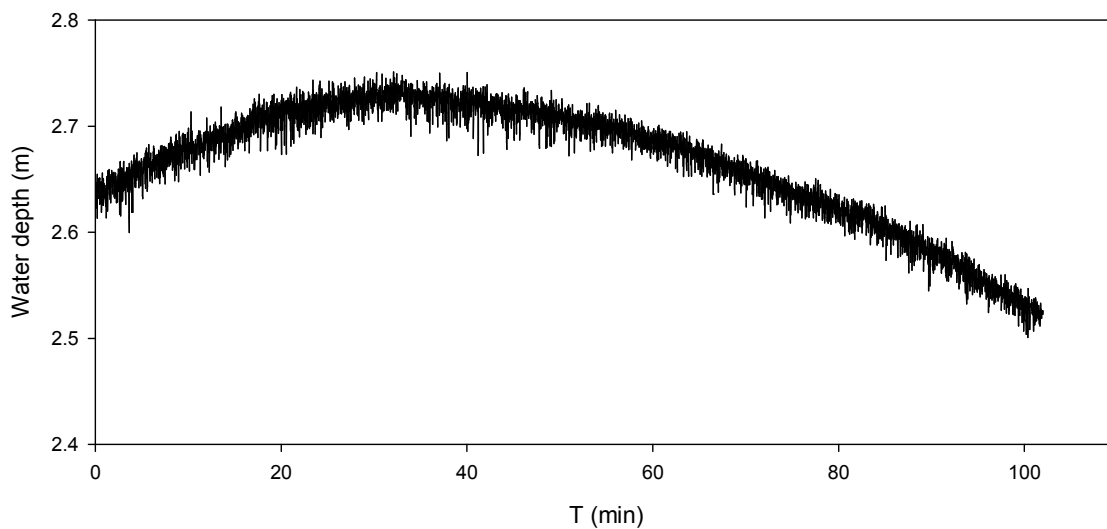
Appendix B: Water depth, DOC concentration, and velocity data

Figure B.1. Water depth over time for entire Frankfort deployment (filtered to 1 Hz for clarity).

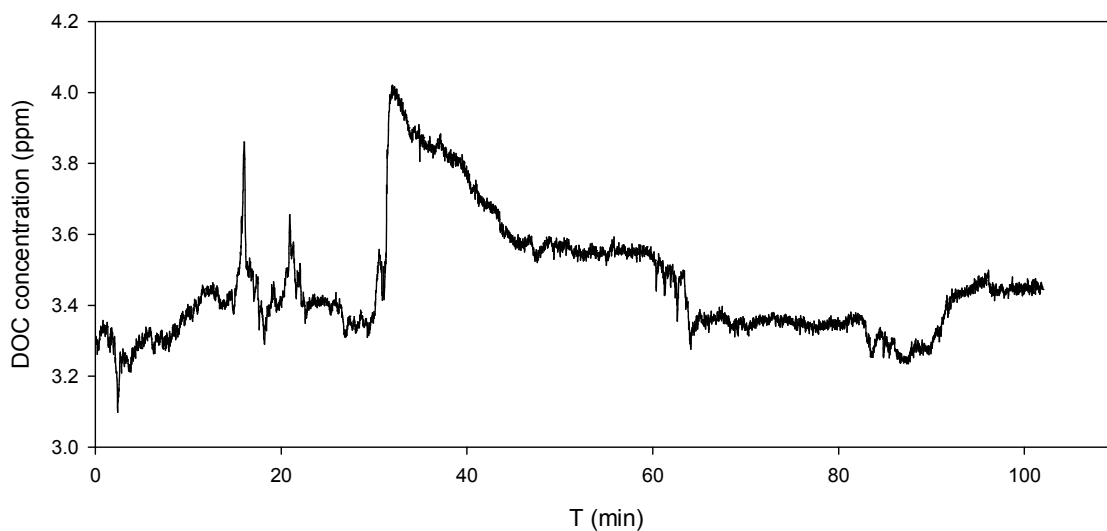


Figure B.2. DOC concentration over time for entire Frankfort deployment (filtered to 1 Hz for clarity).

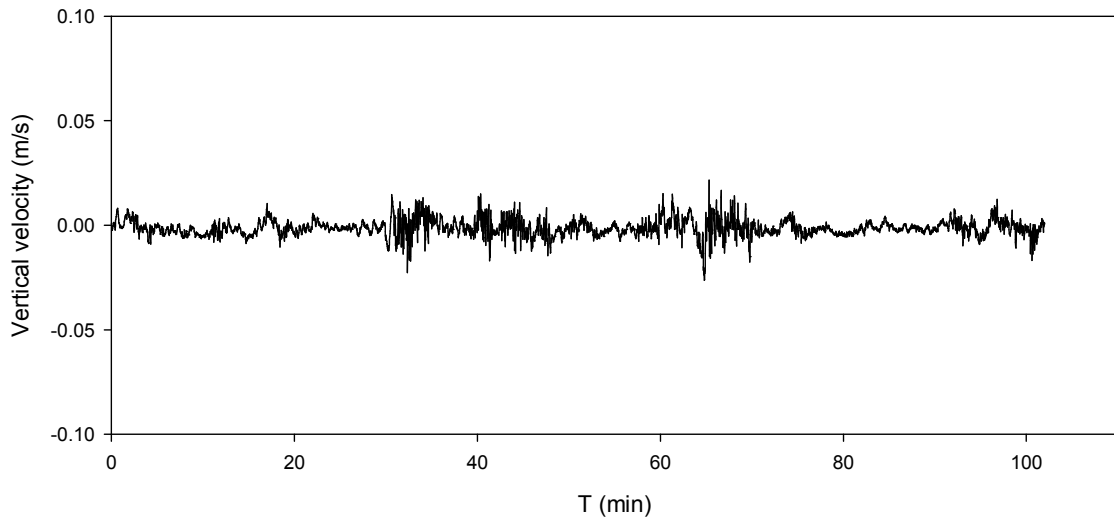


Figure B.3. Vertical velocity over time for entire Frankfort deployment (filtered to 1 Hz for clarity).

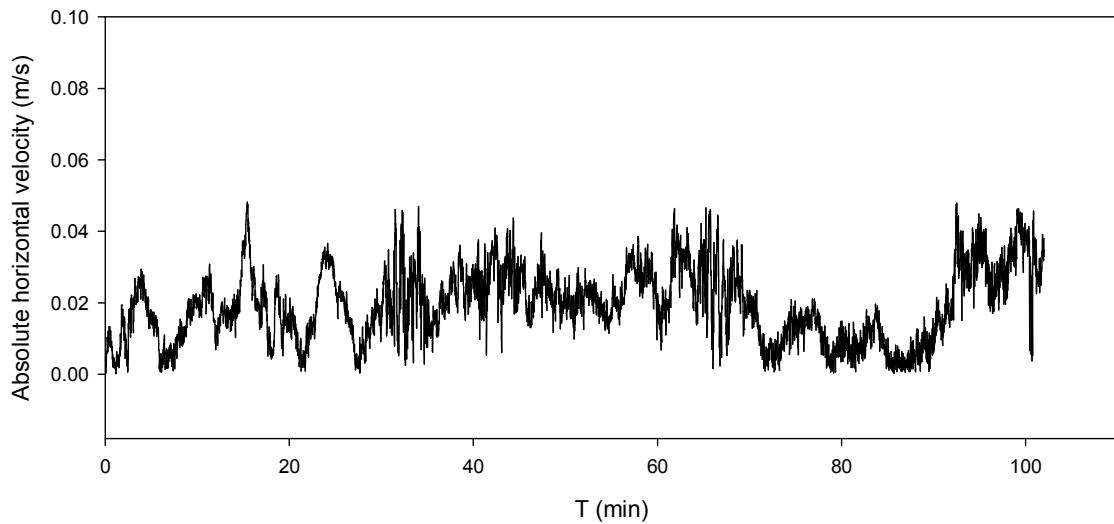


Figure B.4. Absolute horizontal velocity over time for entire Frankfort deployment (filtered to 1 Hz for clarity).

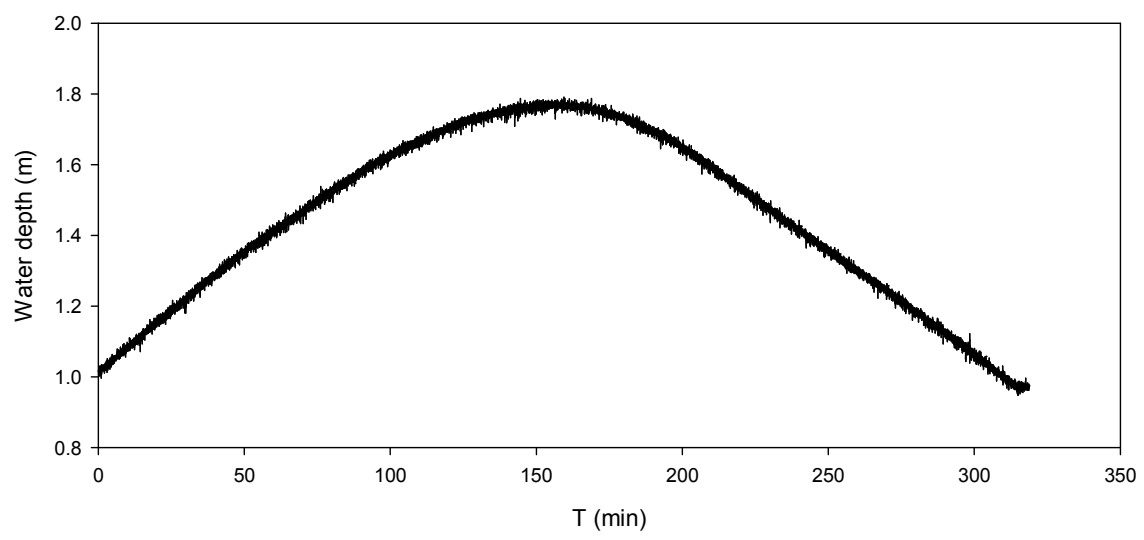


Figure B.5. Water depth over time for entire Squamscott deployment (filtered to 1 Hz for clarity).

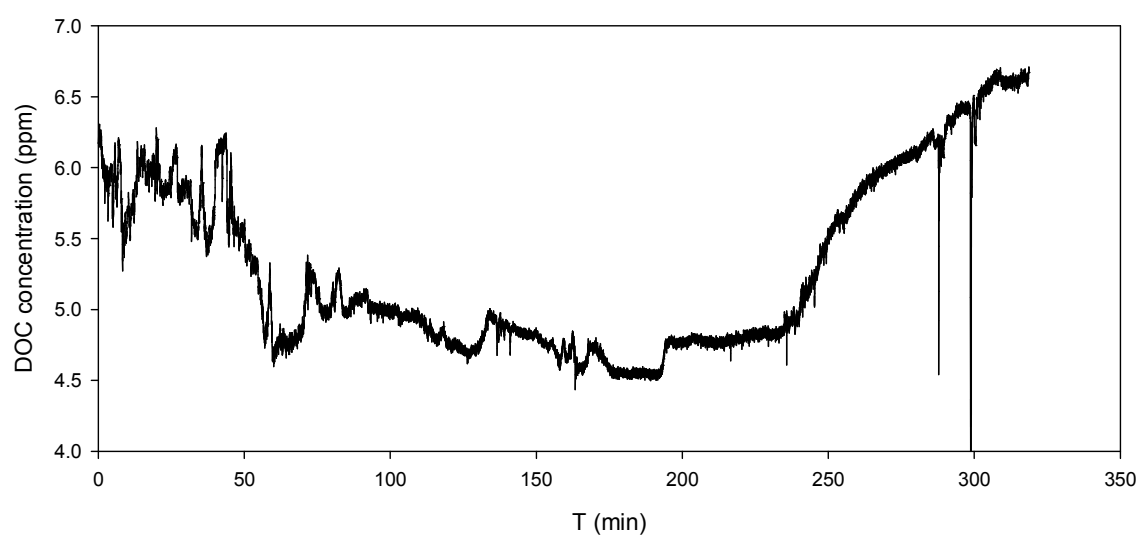


Figure B.6. DOC concentration over time for entire Squamscott deployment (filtered to 1 Hz for clarity).

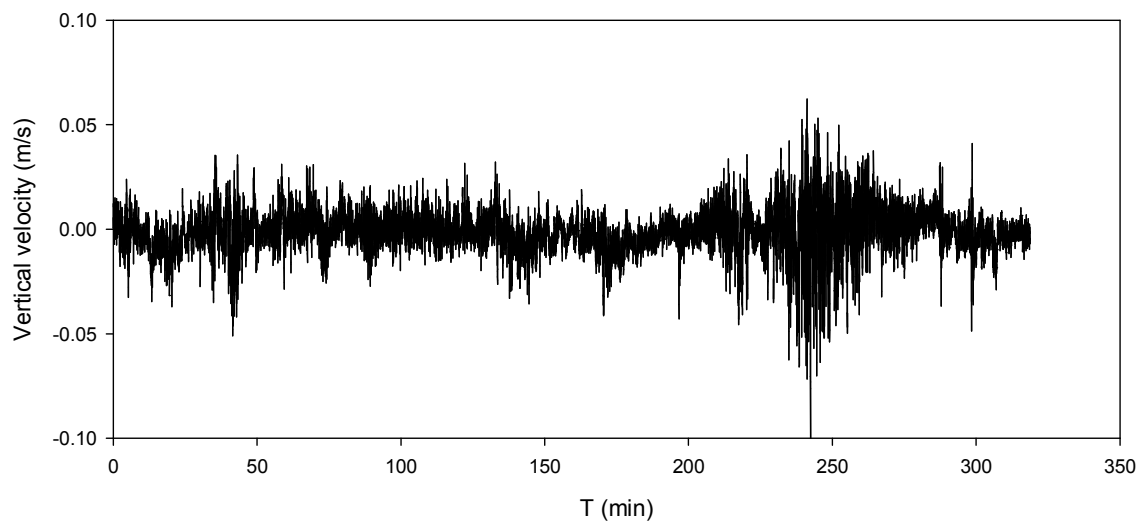


Figure B.7. Vertical velocity over time for entire Squamscott deployment (filtered to 1 Hz for clarity).

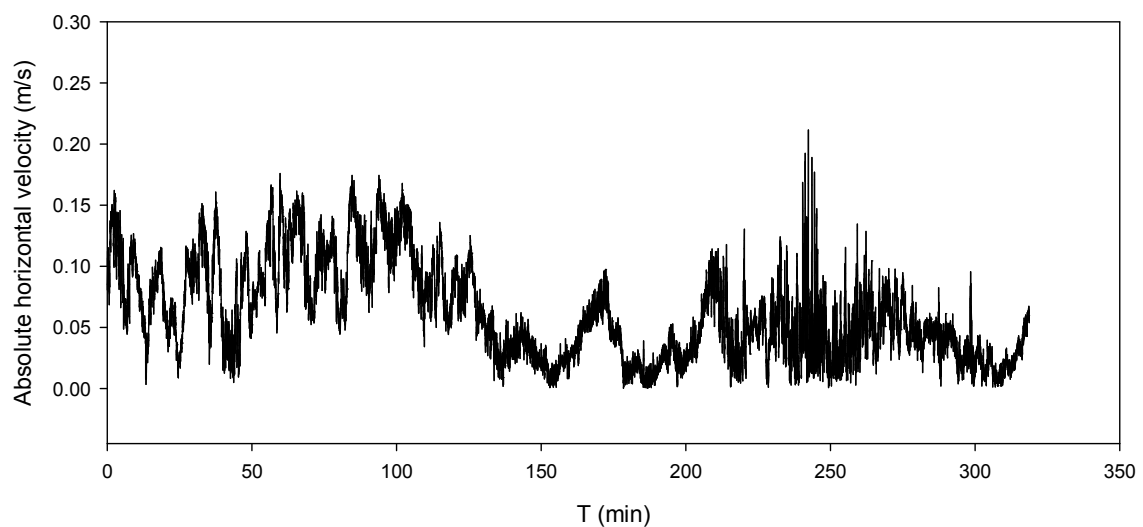


Figure B.8. Absolute horizontal velocity over time for entire Squamscott deployment (filtered to 1 Hz for clarity).

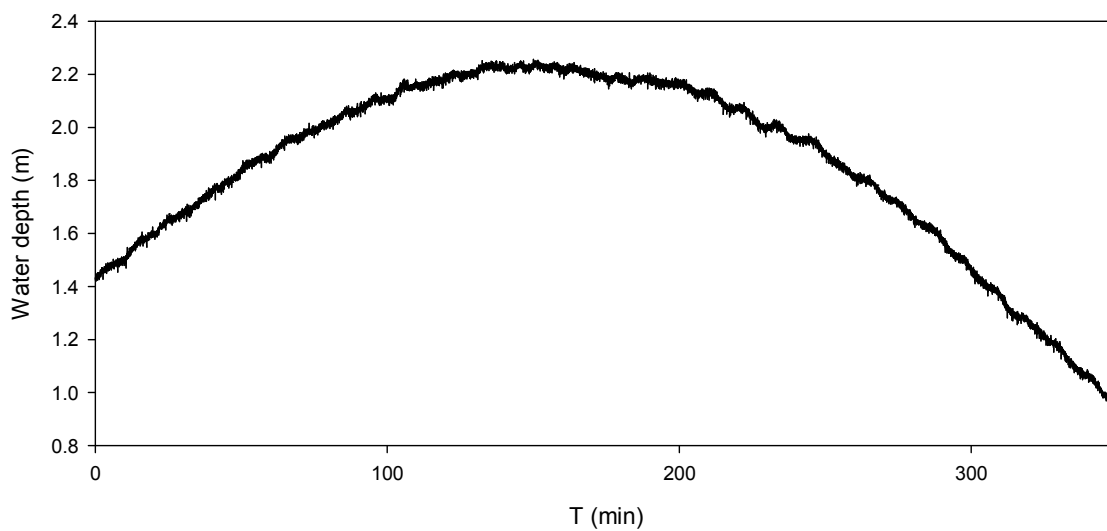


Figure B.9. Water depth over time for entire Kittery deployment (filtered to 1 Hz for clarity).

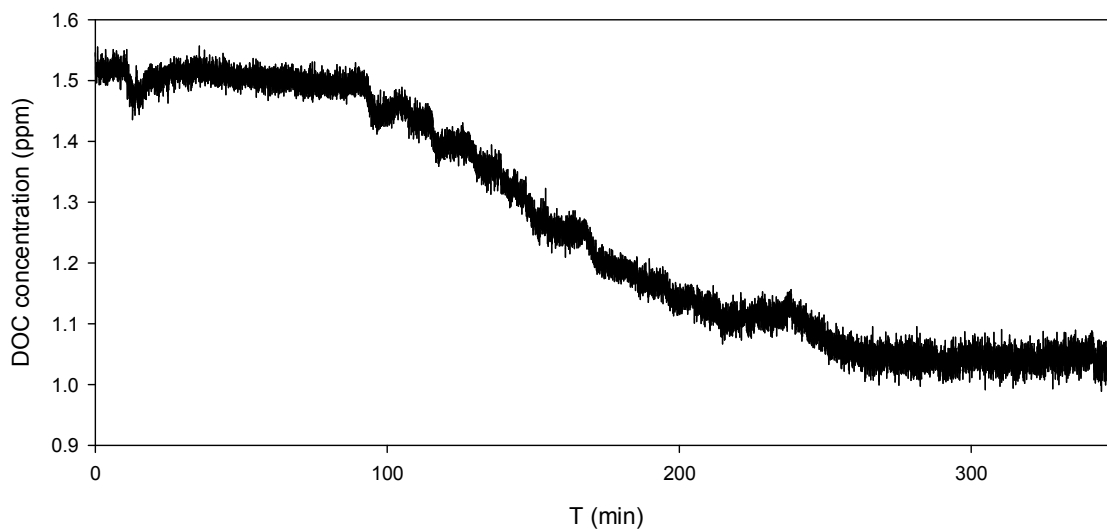


Figure B.10. DOC concentration over time for entire Kittery deployment (filtered to 1 Hz for clarity).

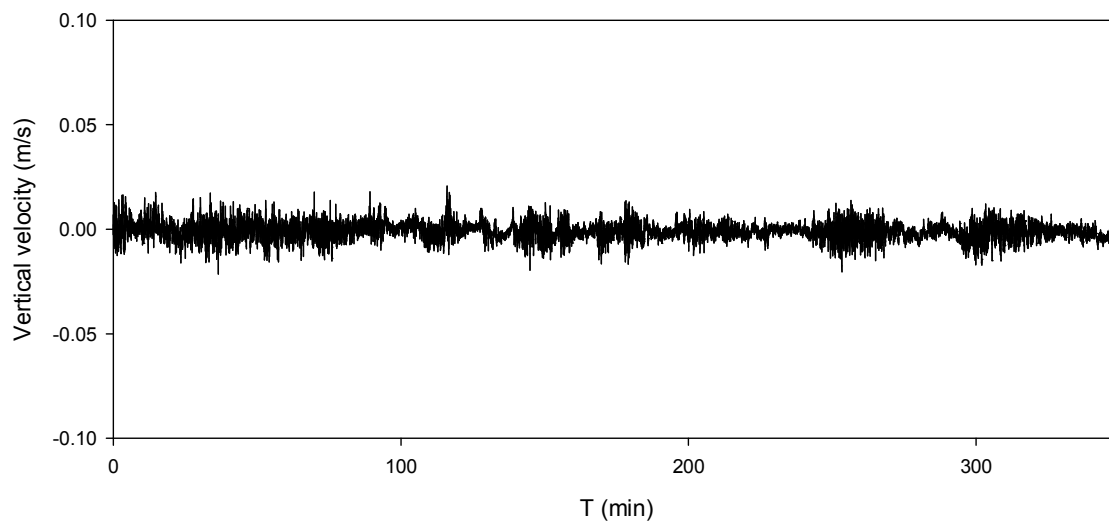


Figure B.11. Vertical velocity over time for entire Kittery deployment (filtered to 1 Hz for clarity).

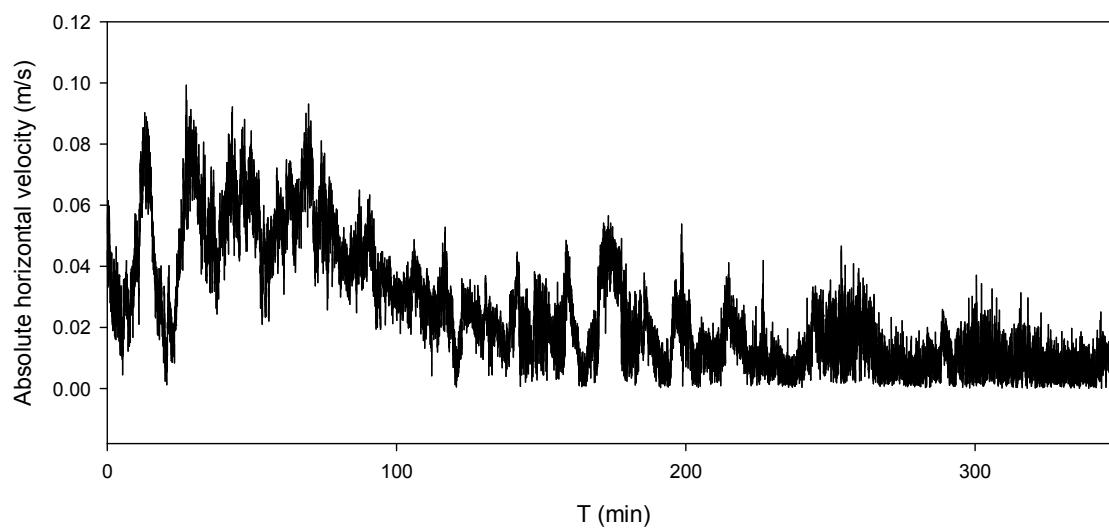


Figure B.12. Absolute horizontal velocity over time for entire Kittery deployment (filtered to 1 Hz for clarity).

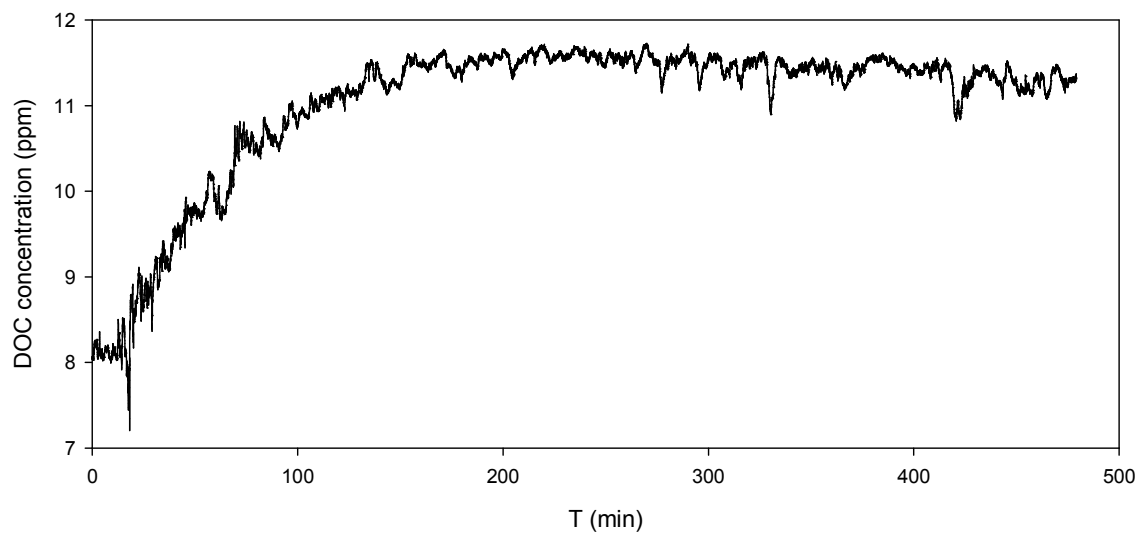


Figure B.13. DOC concentration over time for entire Burton Bog deployment (filtered to 1 Hz for clarity).

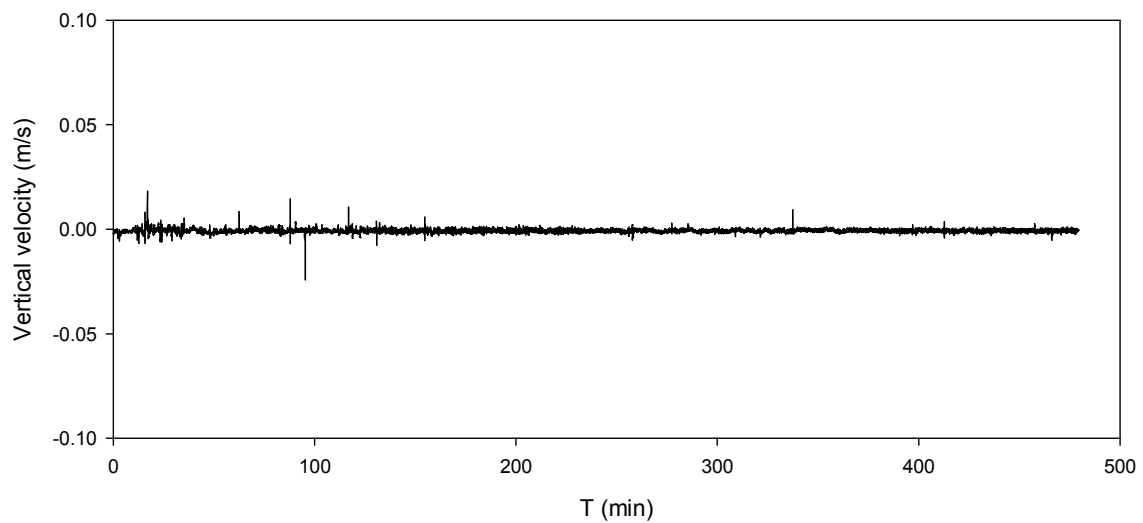


Figure B.14. Vertical velocity over time for entire Burton Bog deployment (filtered to 1 Hz for clarity).

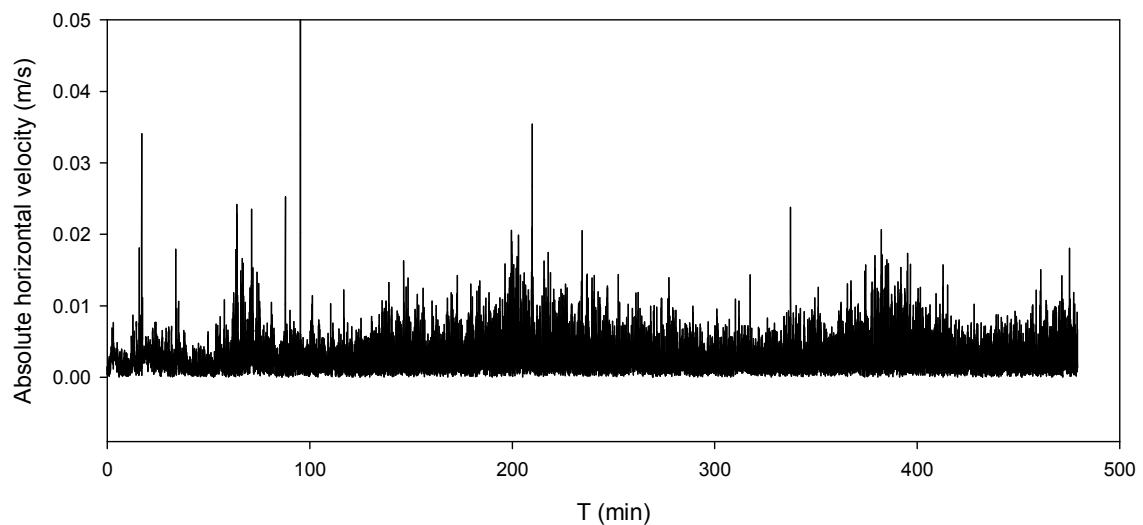


Figure B.15. Absolute horizontal velocity over time for entire Burton Bog deployment (filtered to 1 Hz for clarity).

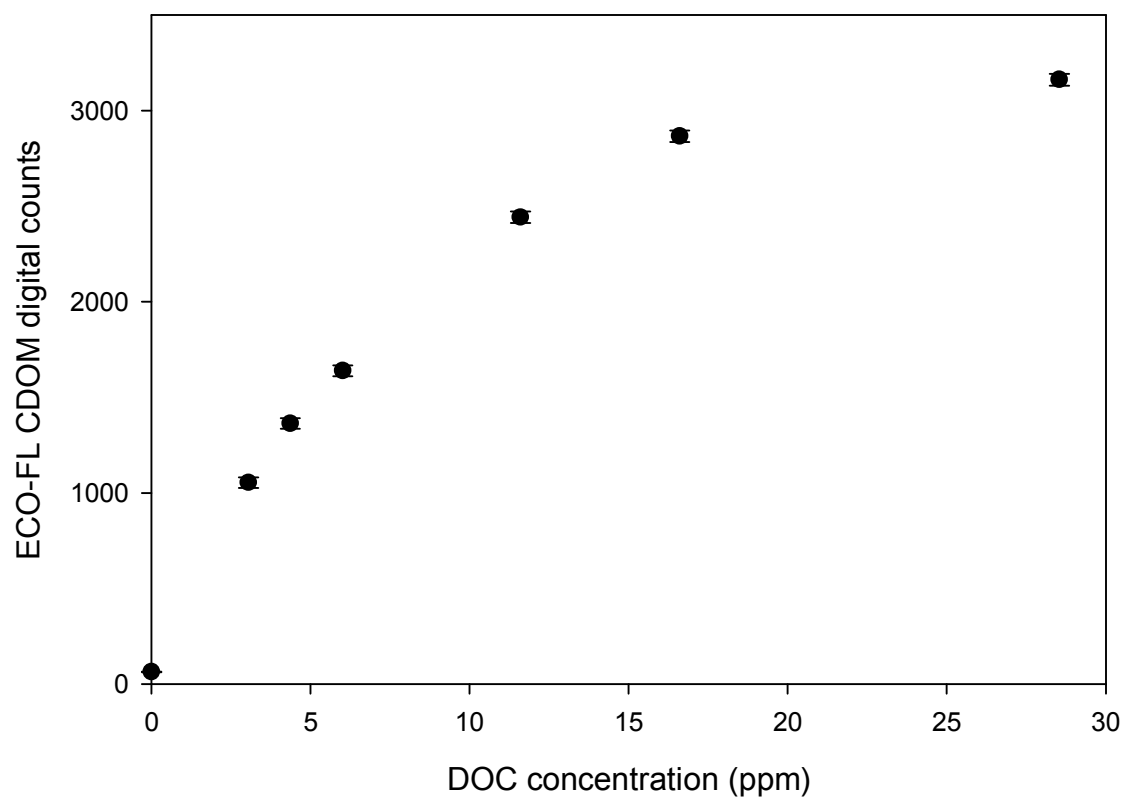
Appendix C: CDOM calibration points

Figure C.1. All points obtained in laboratory DOC calibration of ECO-FL.

Appendix D: Correlation coefficient vs. filter length

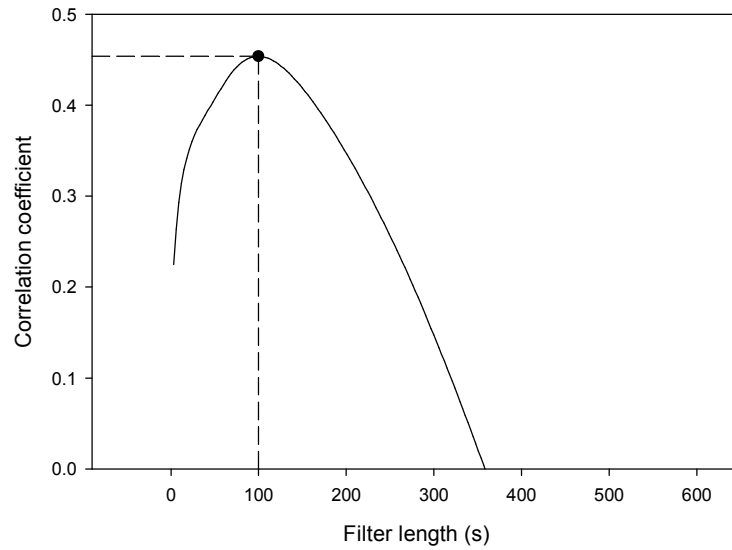


Figure D.1. Correlation coefficient vs. filter length for Frankfort burst 1, shown with optimum averaging window (•).

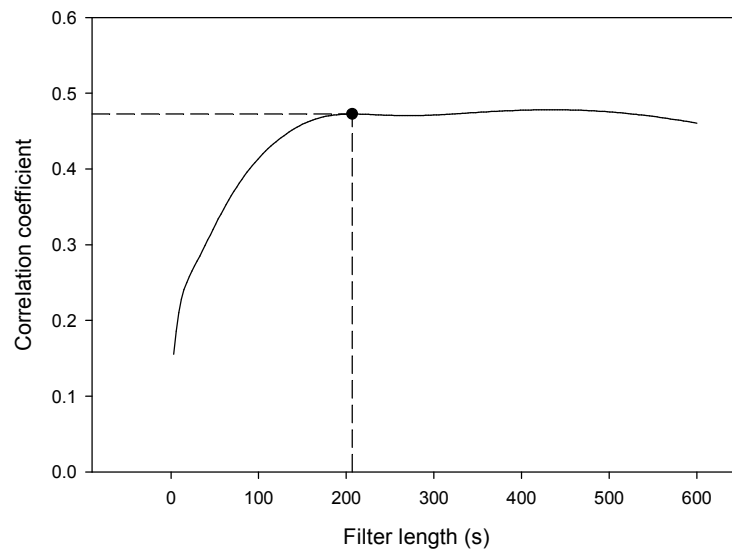


Figure D.2. Correlation coefficient vs. filter length for Frankfort burst 2, shown with optimum averaging window (•).

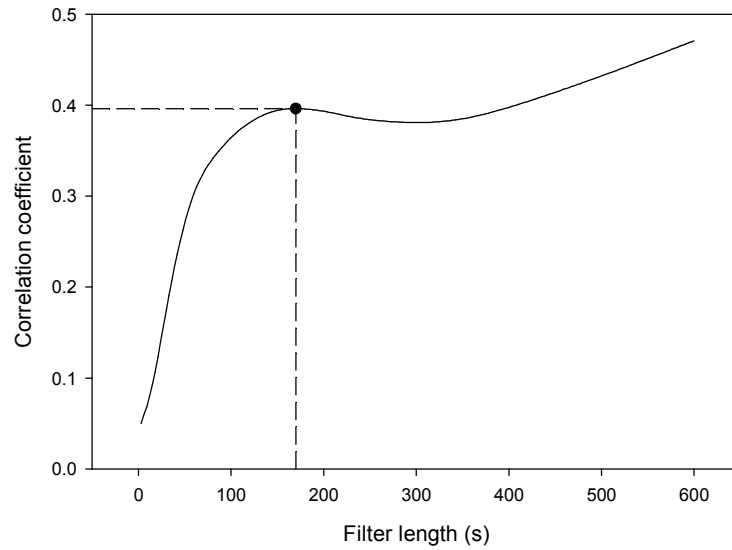


Figure D.3. Correlation coefficient vs. filter length for Squamscott burst, shown with optimum averaging window (•).

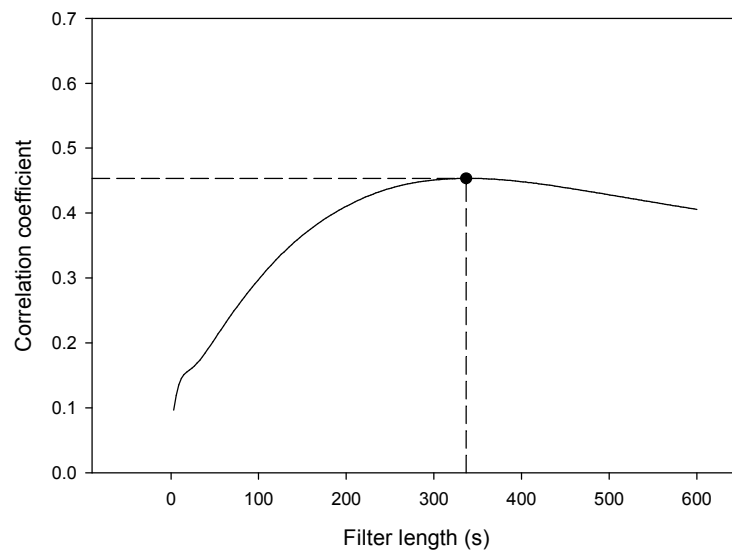


Figure D.4. Correlation coefficient vs. filter length for Kittery tidal ebb burst, shown with optimum averaging window (•).

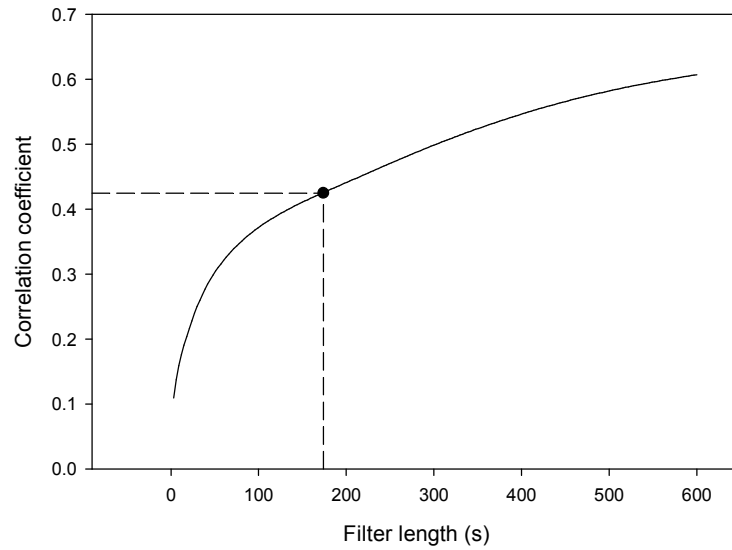


Figure D.5. Correlation coefficient vs. filter length for Kittery tidal flow burst, shown with optimum averaging window (•).

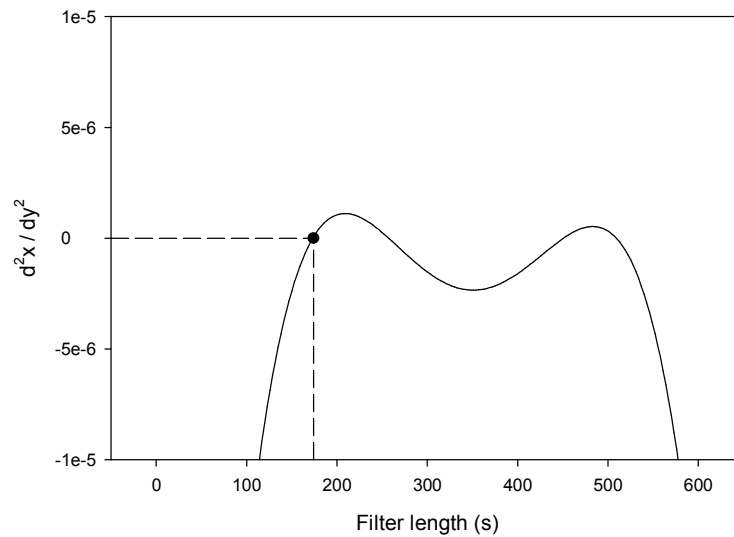


Figure D.6. Second derivative of Fig. D.4 showing initial inflection point (•).

Appendix E: Velocity and concentration with trends

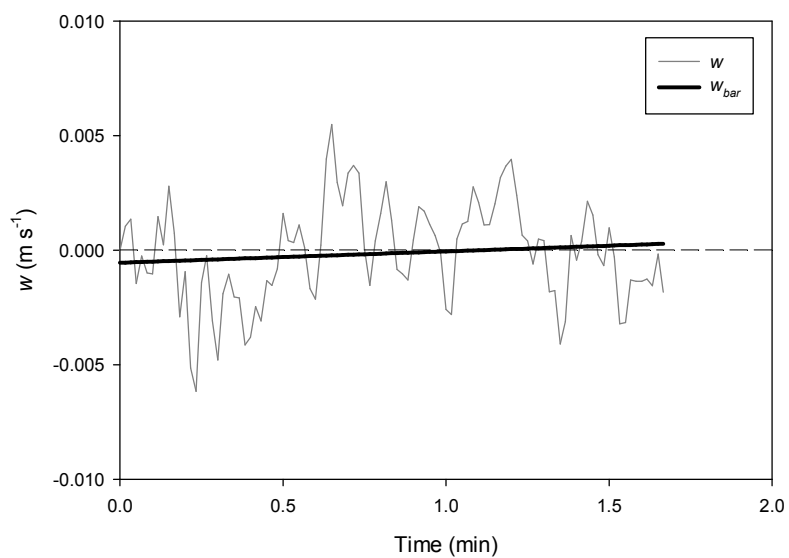


Figure E.1. Vertical velocity and corresponding linear trend for Frankfort burst 1, block 77300-78100 (filtered to 1 Hz for clarity).

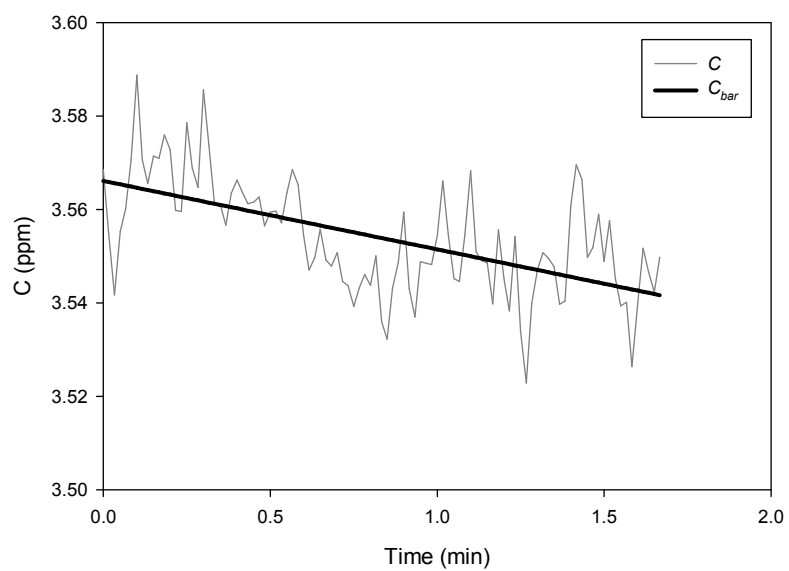


Figure E.2. DOC concentration and corresponding linear trend for Frankfort burst 1, block 77300-78100 (filtered to 1 Hz for clarity).

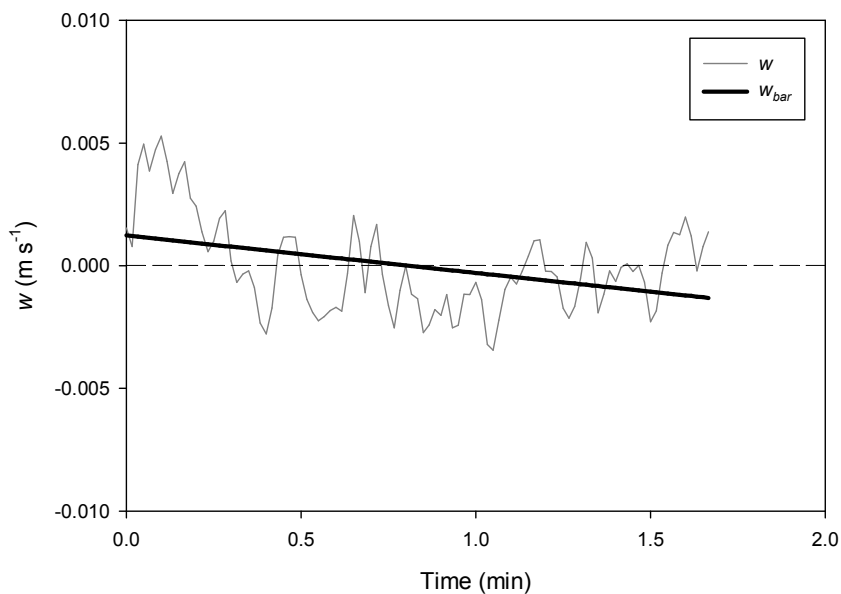


Figure E.3. Vertical velocity and corresponding linear trend for Frankfort burst 1, block 78100-78900 (filtered to 1 Hz for clarity).

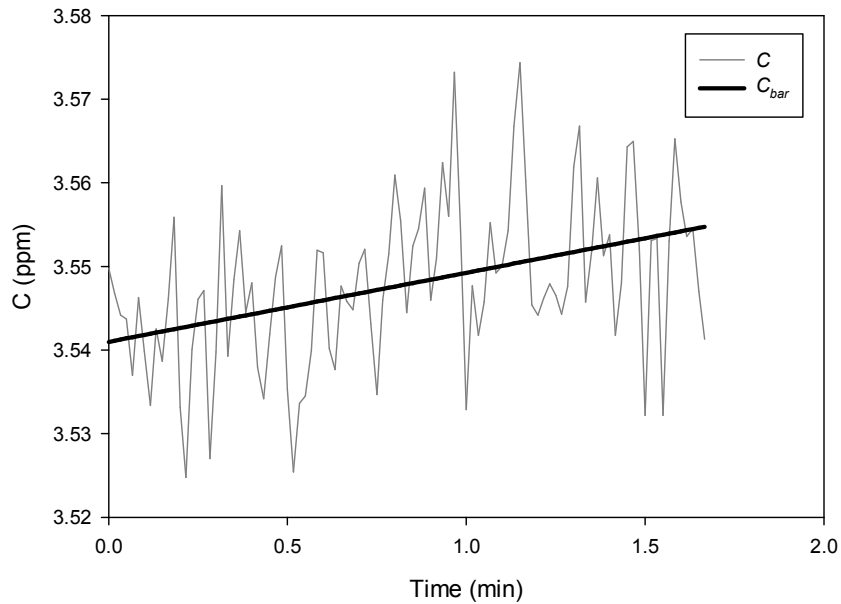


Figure E.4. DOC concentration and corresponding linear trend for Frankfort burst 1, block 78100-78900 (filtered to 1 Hz for clarity).

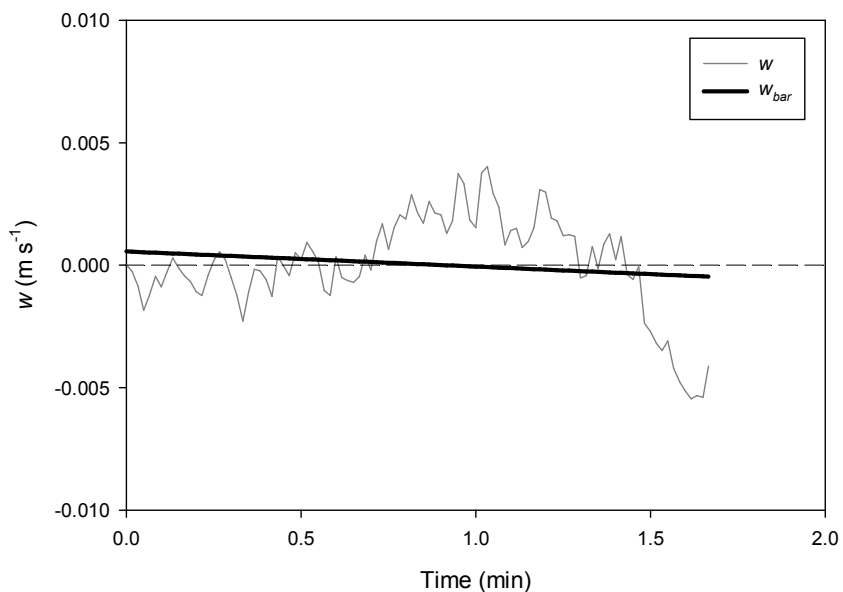


Figure E.5. Vertical velocity and corresponding linear trend for Frankfort burst 1, block 78900-79700 (filtered to 1 Hz for clarity).

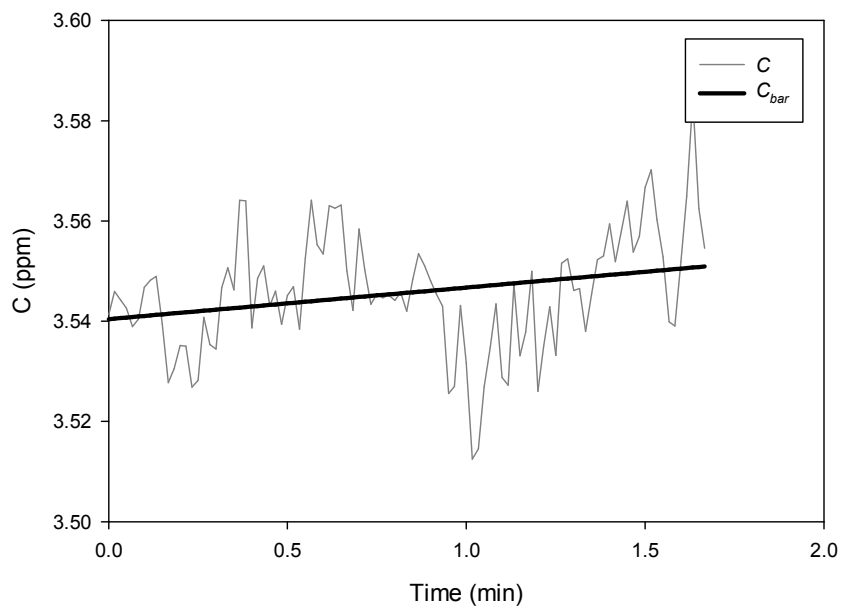


Figure E.6. DOC concentration and corresponding linear trend for Frankfort burst 1, block 78900-79700 (filtered to 1 Hz for clarity).

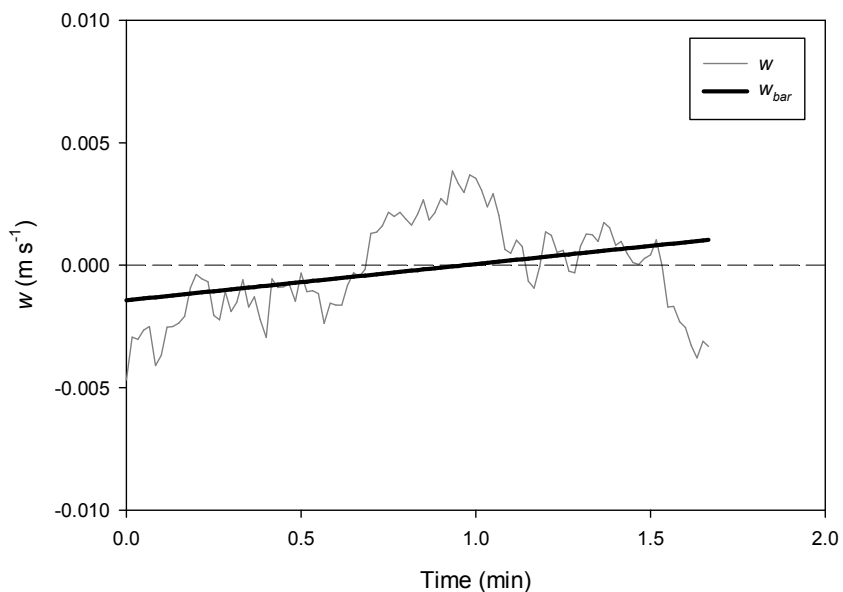


Figure E.7. Vertical velocity and corresponding linear trend for Frankfort burst 1, block 79700-80500 (filtered to 1 Hz for clarity).

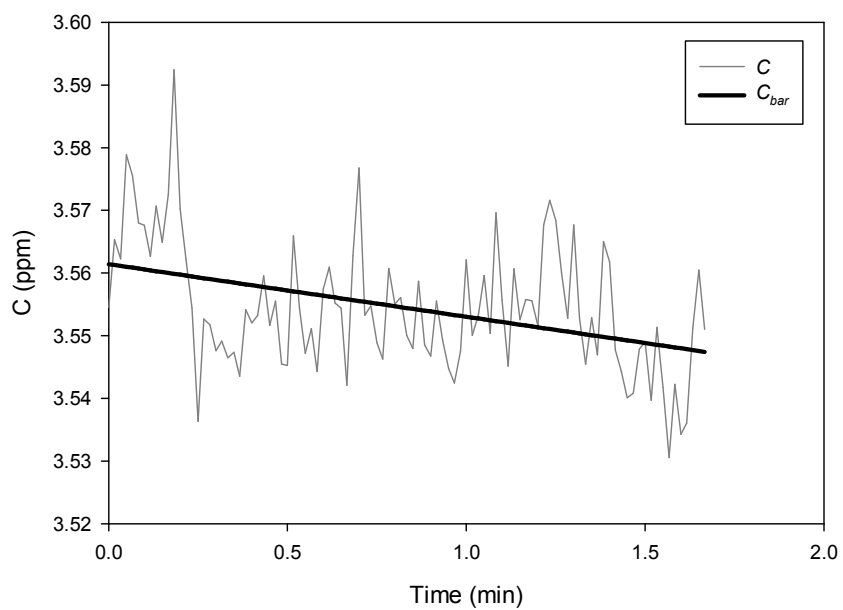


Figure E.8. DOC concentration and corresponding linear trend for Frankfort burst 1, block 79700-80500 (filtered to 1 Hz for clarity).

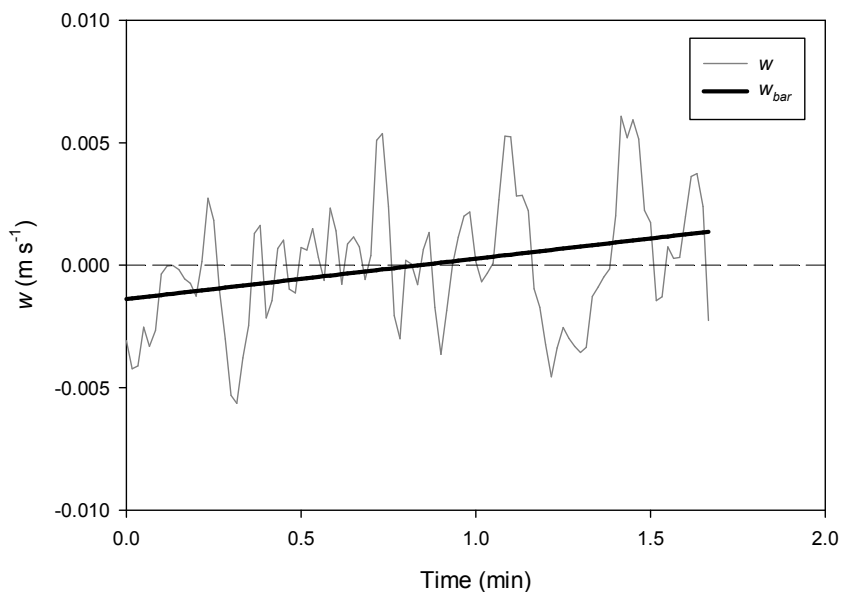


Figure E.9. Vertical velocity and corresponding linear trend for Frankfort burst 1, block 80500-81300 (filtered to 1 Hz for clarity).

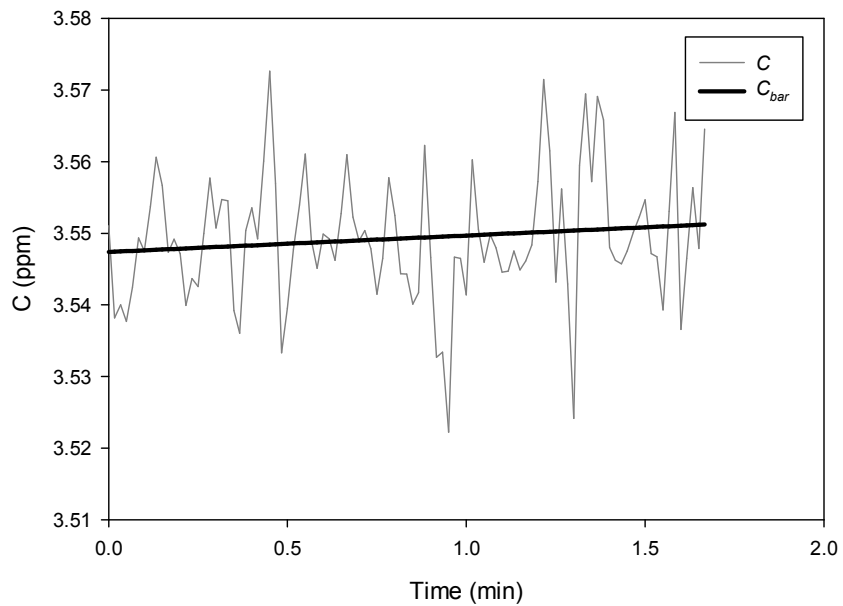


Figure E.10. DOC concentration and corresponding linear trend for Frankfort burst 1, block 80500-81300 (filtered to 1 Hz for clarity).

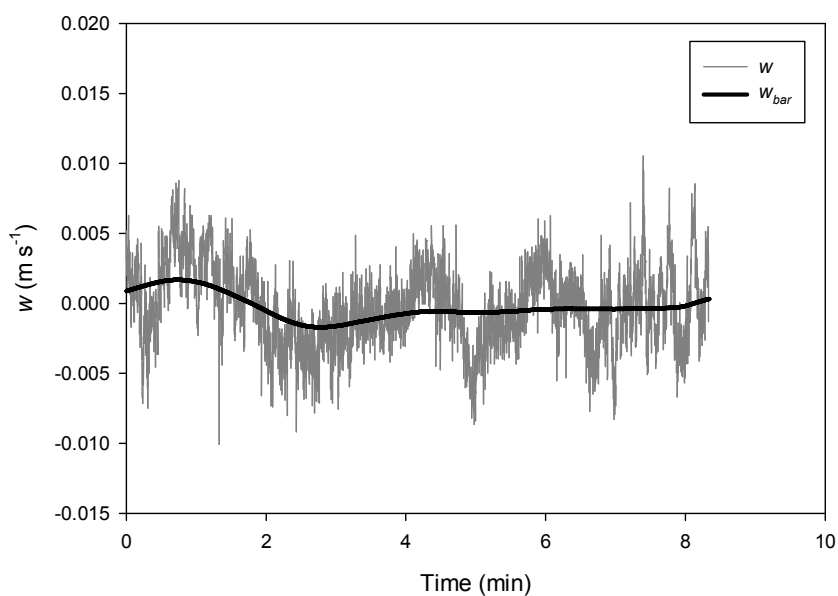


Figure E.11. Vertical velocity and corresponding moving average trend for Frankfort burst 1.

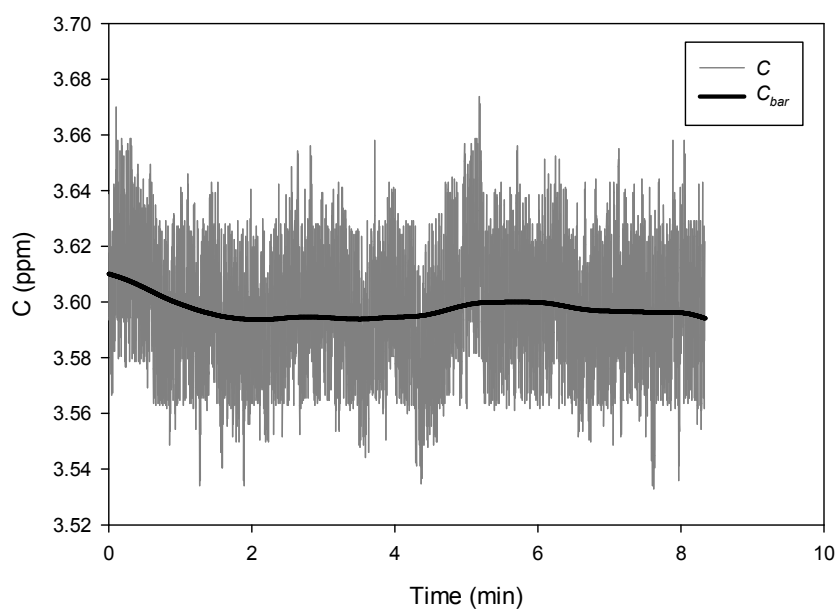


Figure E.12. DOC concentration and corresponding moving average trend for Frankfort burst 1.

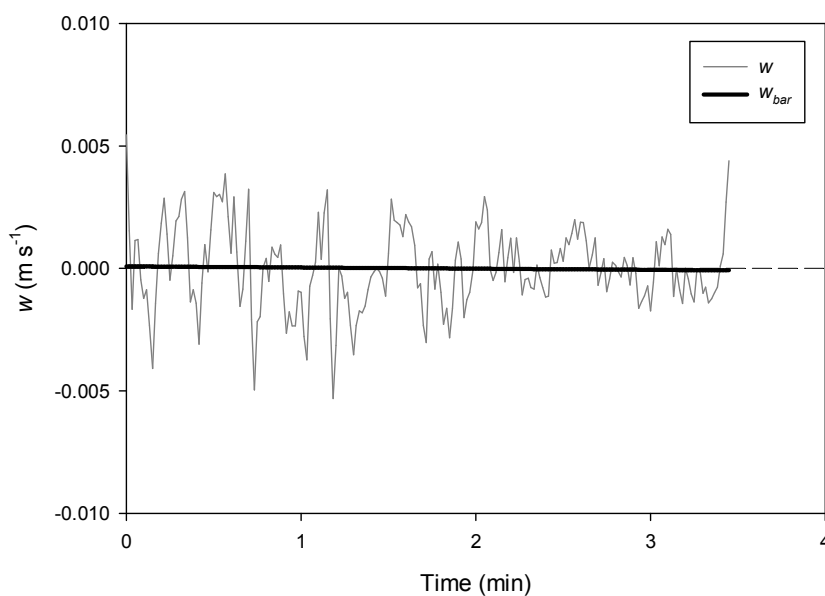


Figure E.13. Vertical velocity and corresponding linear trend for Frankfort burst 2, block 88828-90484 (filtered to 1 Hz for clarity).

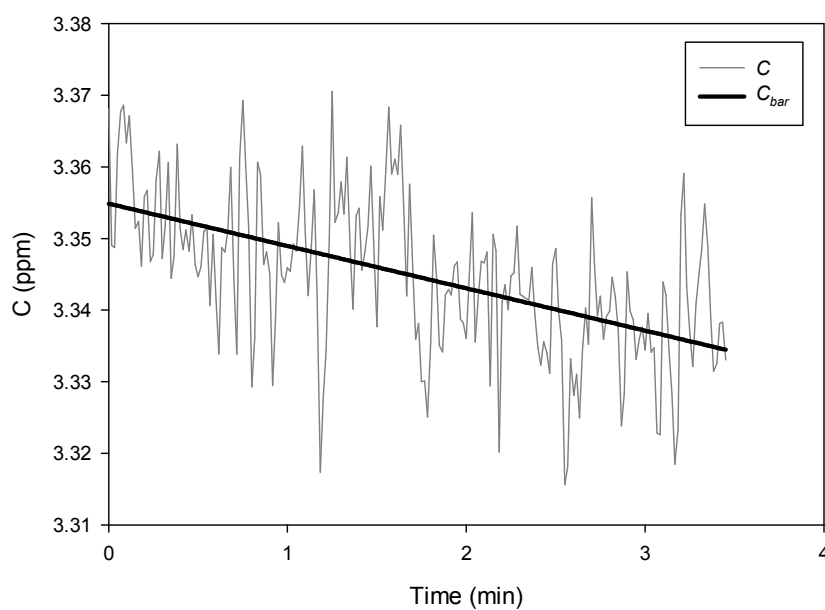


Figure E.14. DOC concentration and corresponding linear trend for Frankfort burst 2, block 88828-90484 (filtered to 1 Hz for clarity).

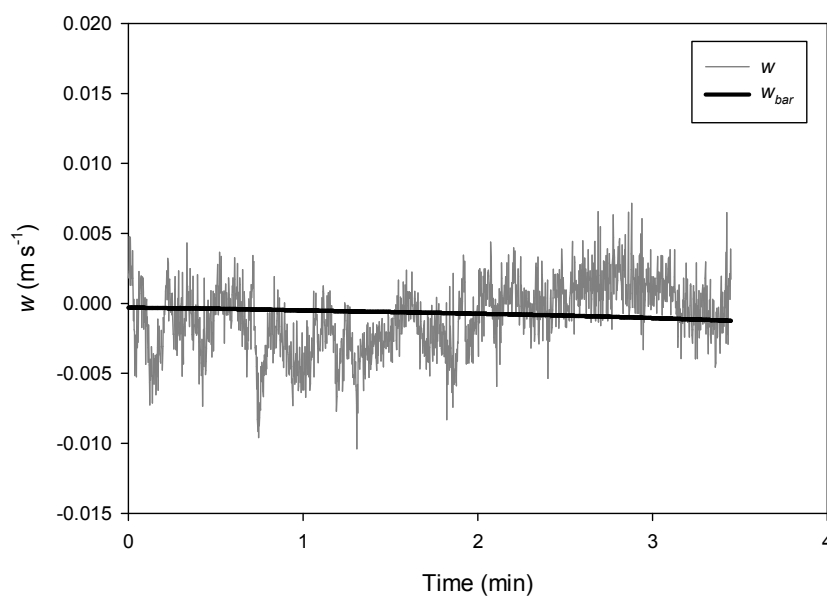


Figure E.15. Vertical velocity and corresponding moving average trend for Frankfort burst 2.

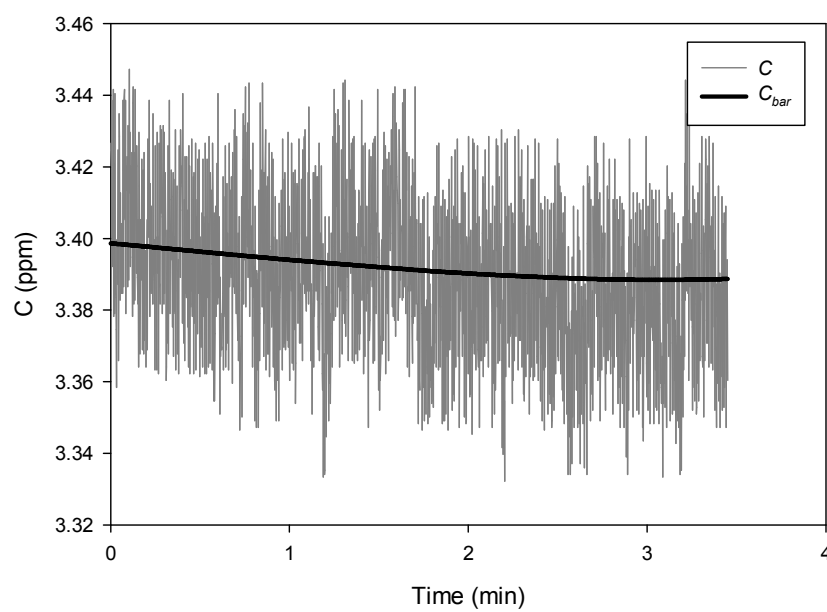


Figure E.16. DOC concentration and corresponding moving average trend for Frankfort burst 2.

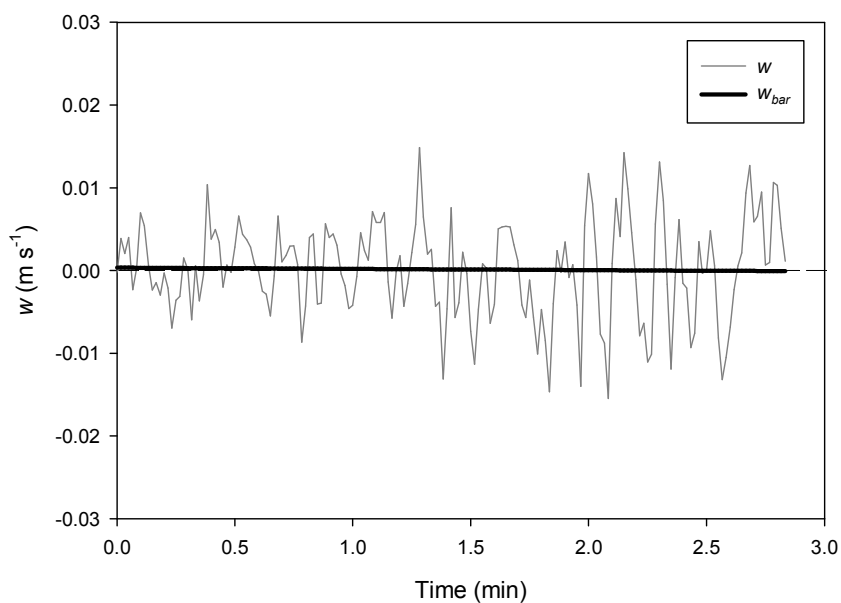


Figure E.17. Vertical velocity and corresponding linear trend for Squamscott burst, block 103680-105040 (filtered to 1 Hz for clarity).

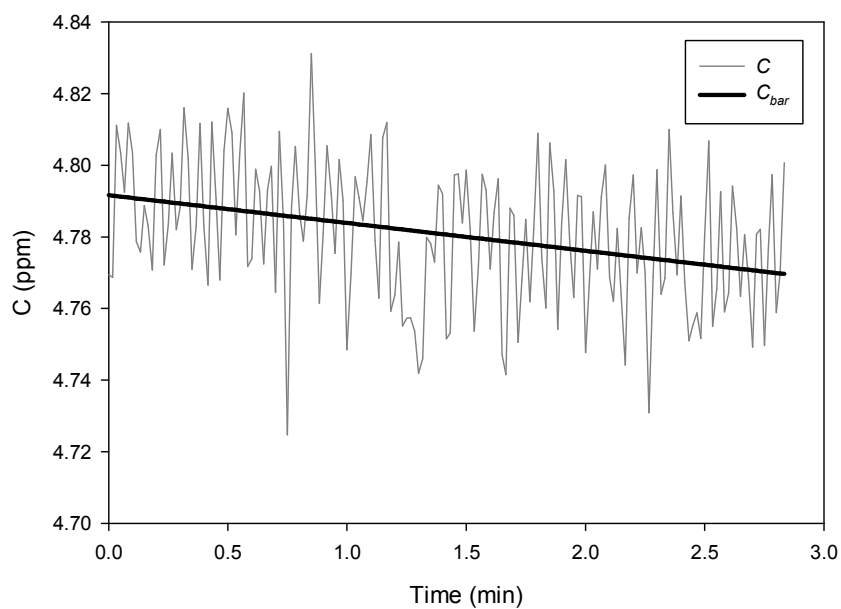


Figure E.18. DOC concentration and corresponding linear trend for Squamscott burst, block 103680-105040 (filtered to 1 Hz for clarity).

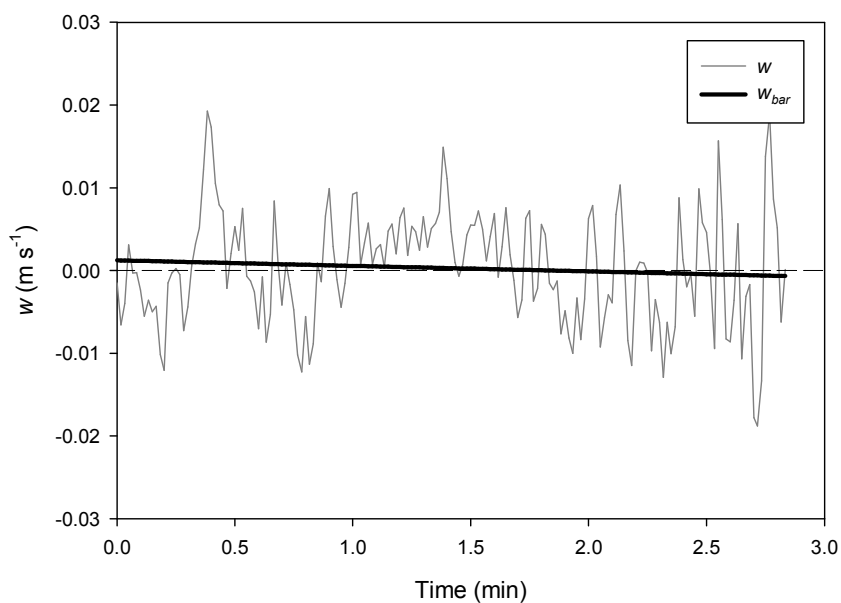


Figure E.19. Vertical velocity and corresponding linear trend for Squamscott burst, block 105040-106400 (filtered to 1 Hz for clarity).

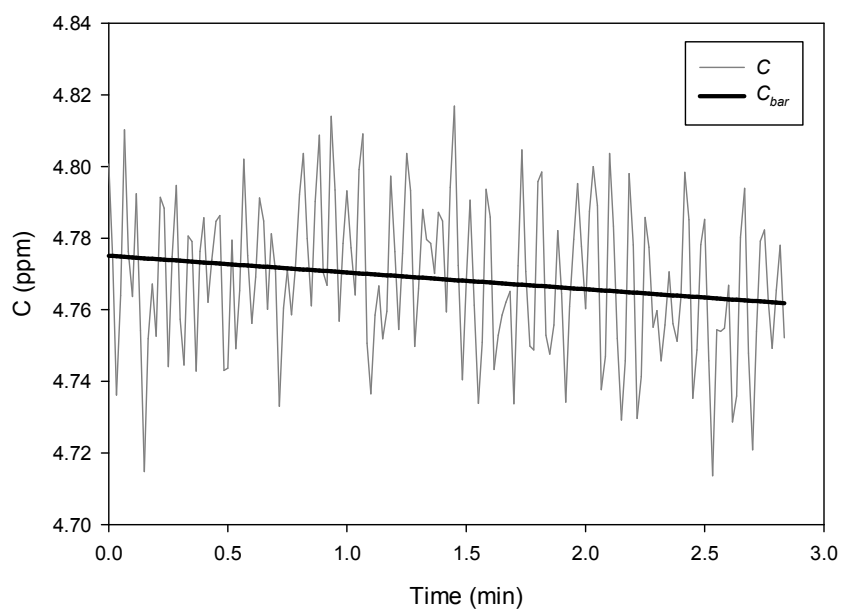


Figure E.20. DOC concentration and corresponding linear trend for Squamscott burst, block 105040-106400 (filtered to 1 Hz for clarity).

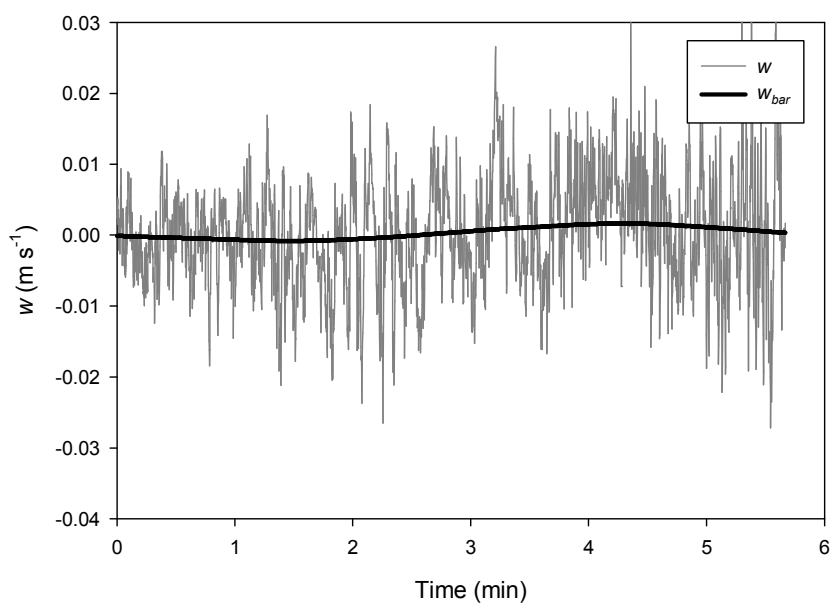


Figure E.21. Vertical velocity and corresponding moving average trend for Squamscott burst.

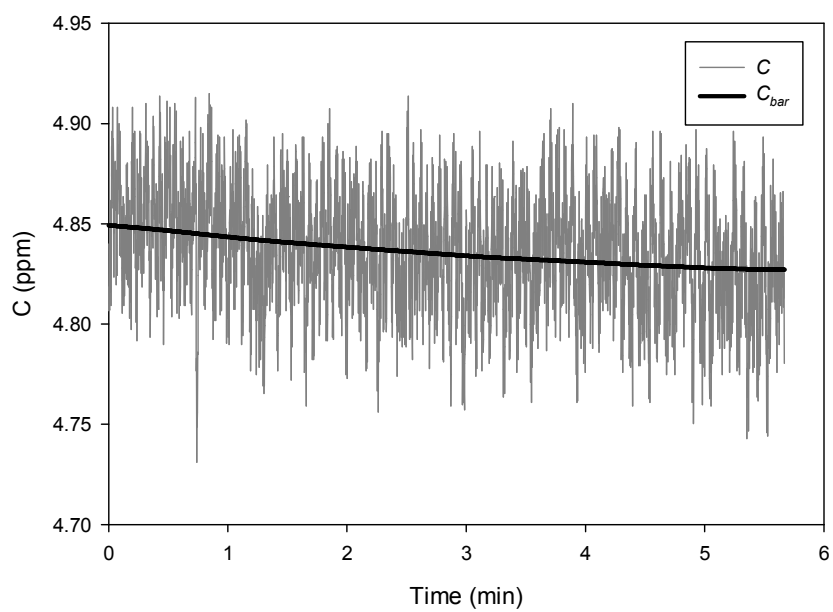


Figure E.22. DOC concentration and corresponding moving average trend for Squamscott burst.

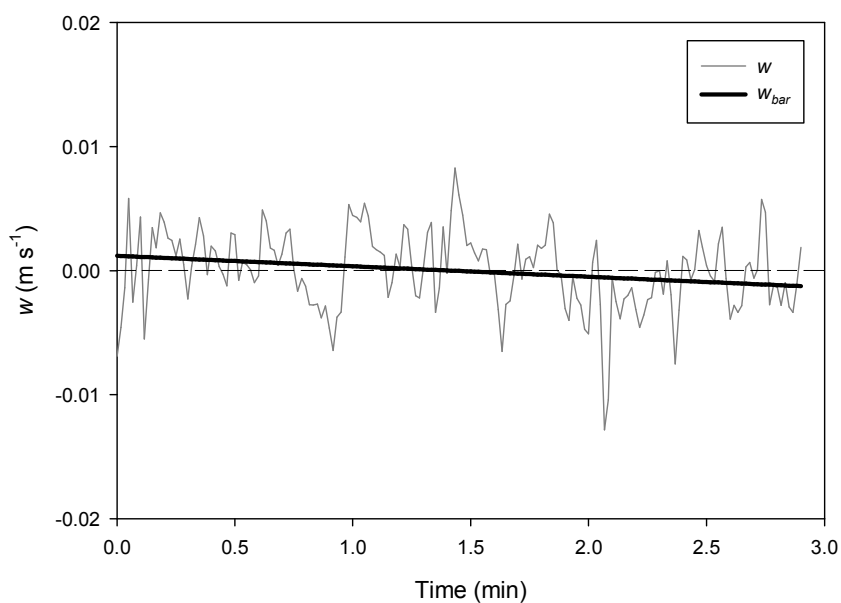


Figure E.23. Vertical velocity and corresponding linear trend for Kittery tidal flow burst, block 9396-10788 (filtered to 1 Hz for clarity).

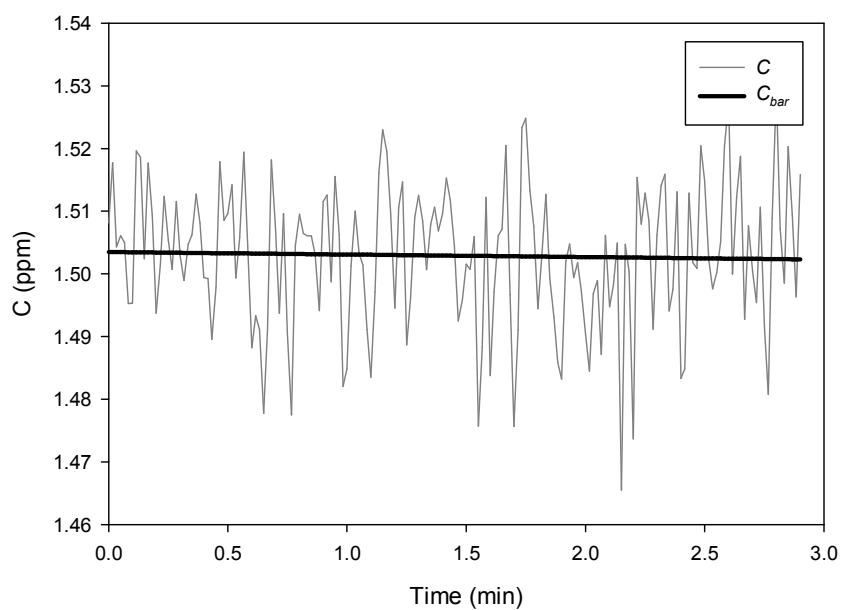


Figure E.24. DOC concentration and corresponding linear trend for Kittery tidal flow burst, block 9396-10788 (filtered to 1 Hz for clarity).

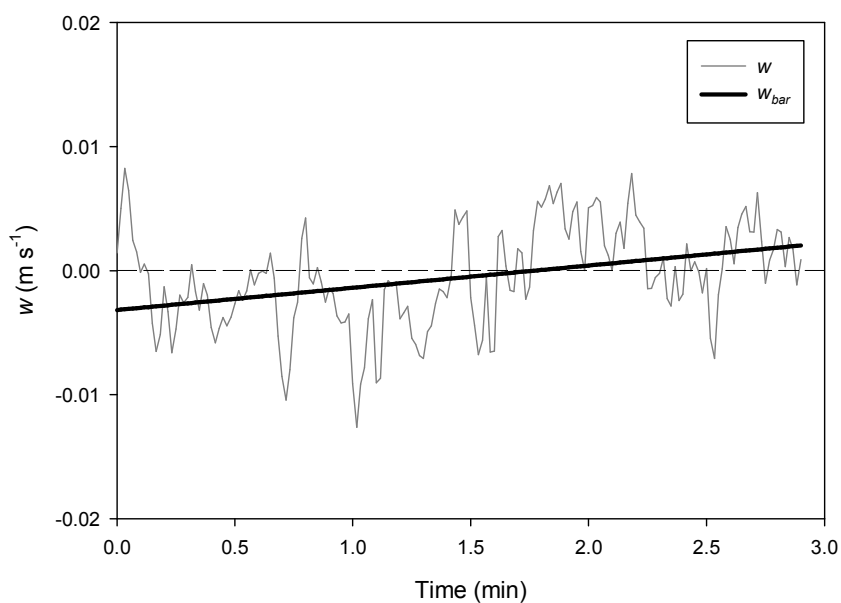


Figure E.25. Vertical velocity and corresponding linear trend for Kittery tidal flow burst, block 10788-12180 (filtered to 1 Hz for clarity).

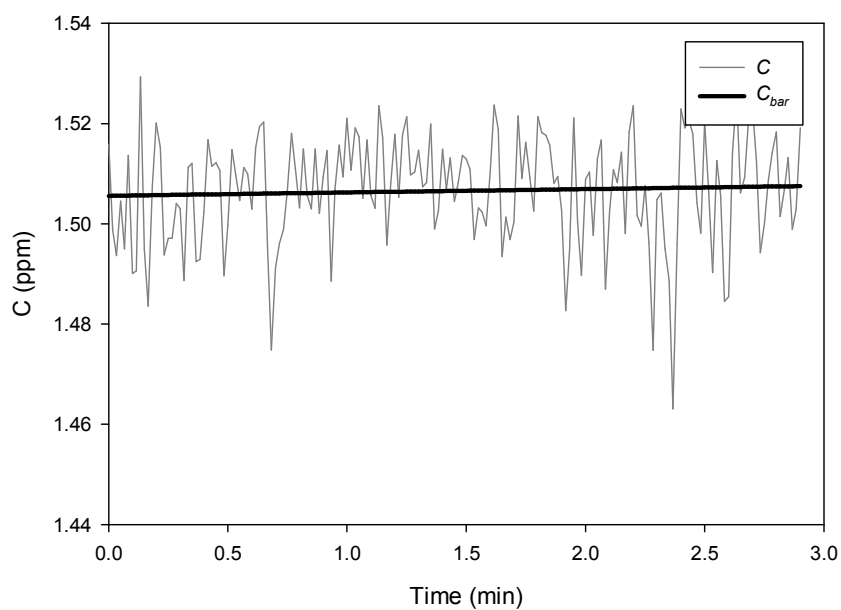


Figure E.26. DOC concentration and corresponding linear trend for Kittery tidal flow burst, block 10788-12180 (filtered to 1 Hz for clarity).

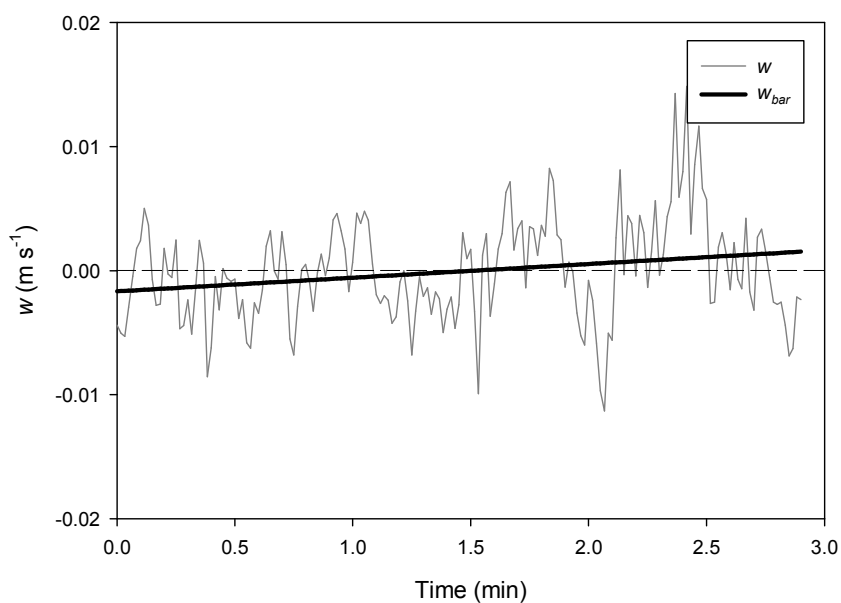


Figure E.27. Vertical velocity and corresponding linear trend for Kittery tidal flow burst, block 12180-13572 (filtered to 1 Hz for clarity).

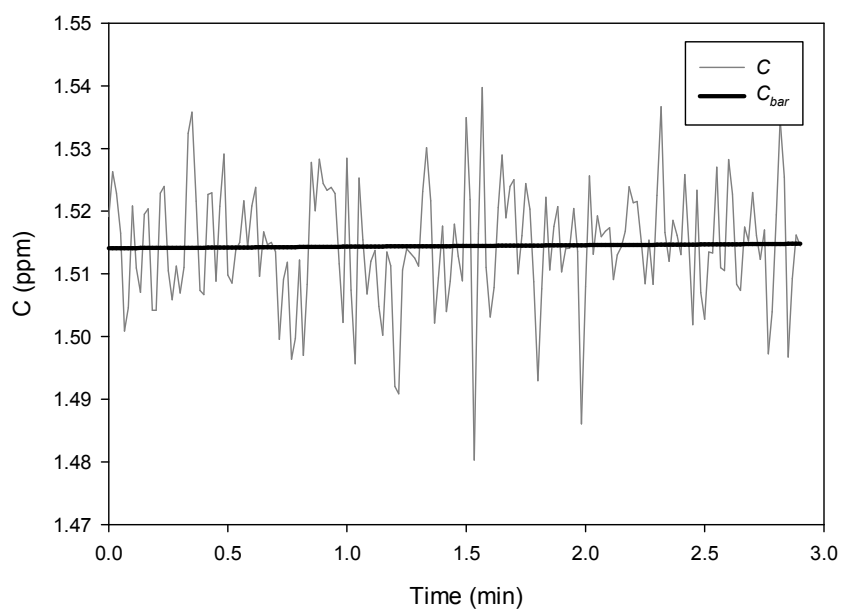


Figure E.28. DOC concentration and corresponding linear trend for Kittery tidal flow burst, block 12180-13572 (filtered to 1 Hz for clarity).

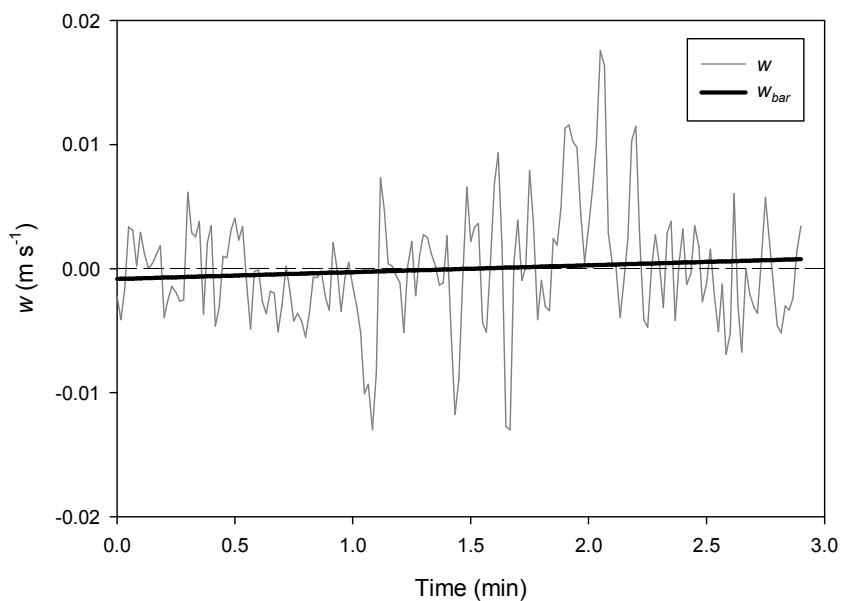


Figure E.29. Vertical velocity and corresponding linear trend for Kittery tidal flow burst, block 13572-14964 (filtered to 1 Hz for clarity).

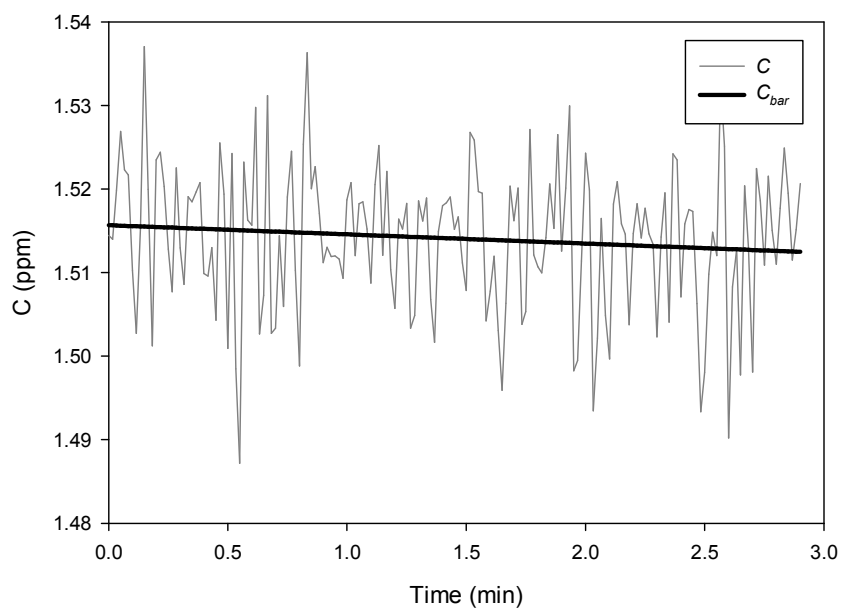


Figure E.30. DOC concentration and corresponding linear trend for Kittery tidal flow burst, block 13572-14964 (filtered to 1 Hz for clarity).

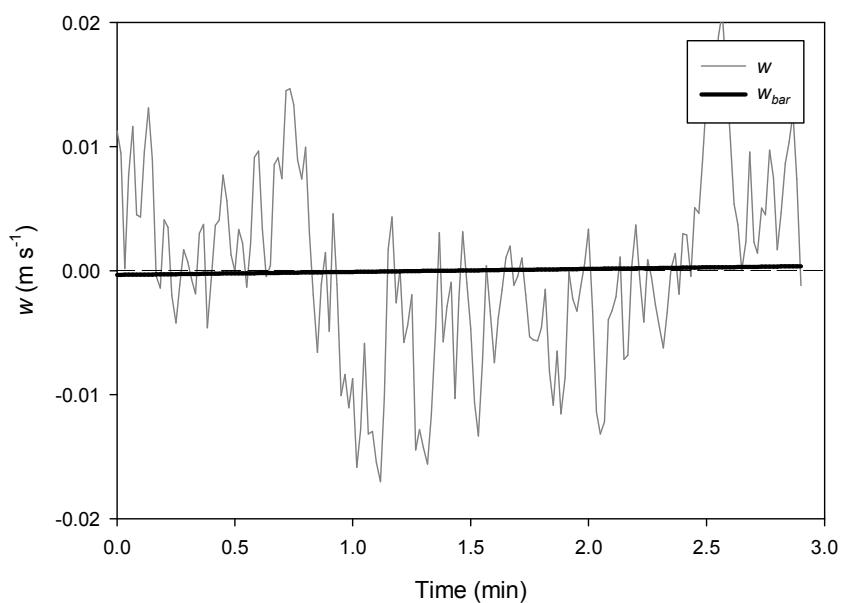


Figure E.31. Vertical velocity and corresponding linear trend for Kittery tidal flow burst, block 14964-16356 (filtered to 1 Hz for clarity).

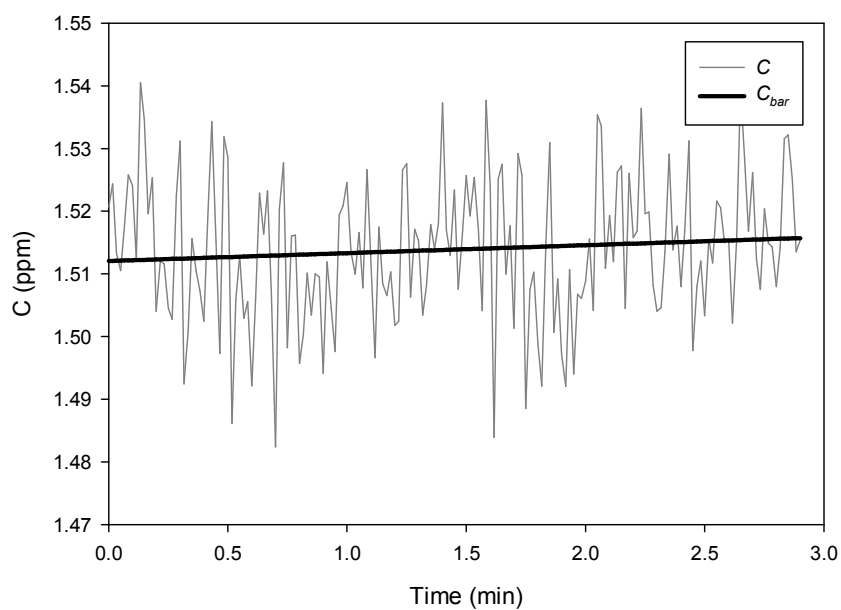


Figure E.32. DOC concentration and corresponding linear trend for Kittery tidal flow burst, block 14964-16356 (filtered to 1 Hz for clarity).

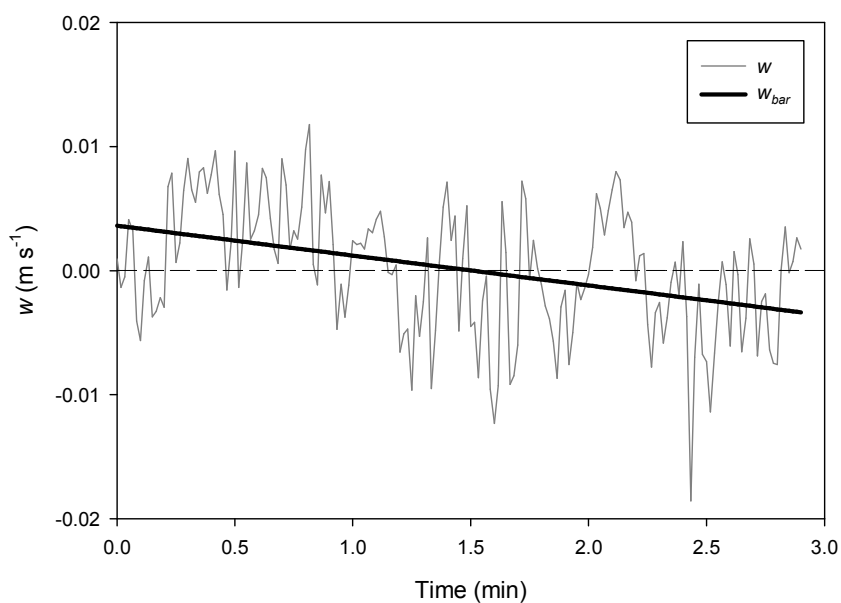


Figure E.33. Vertical velocity and corresponding linear trend for Kittery tidal flow burst, block 16356-17748 (filtered to 1 Hz for clarity).

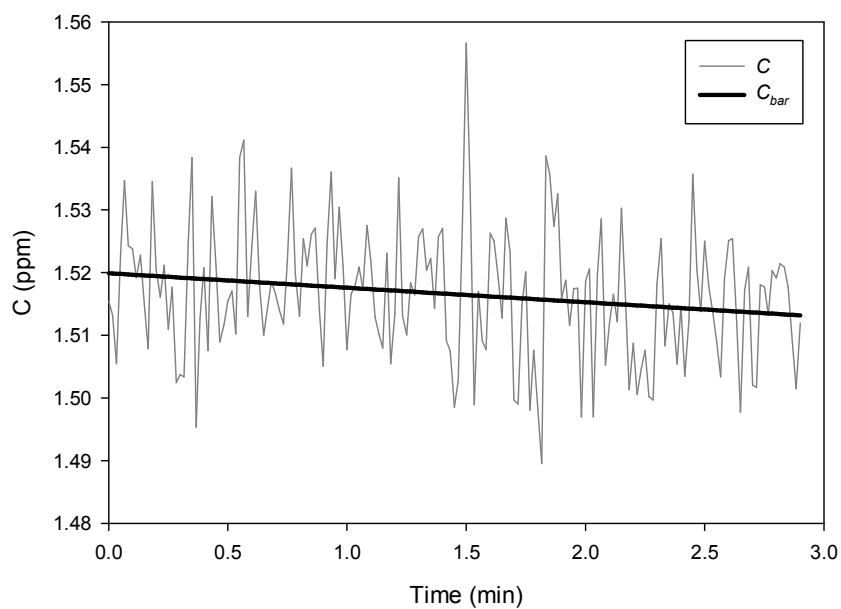


Figure E.34. DOC concentration and corresponding linear trend for Kittery tidal flow burst, block 16356-17748 (filtered to 1 Hz for clarity).

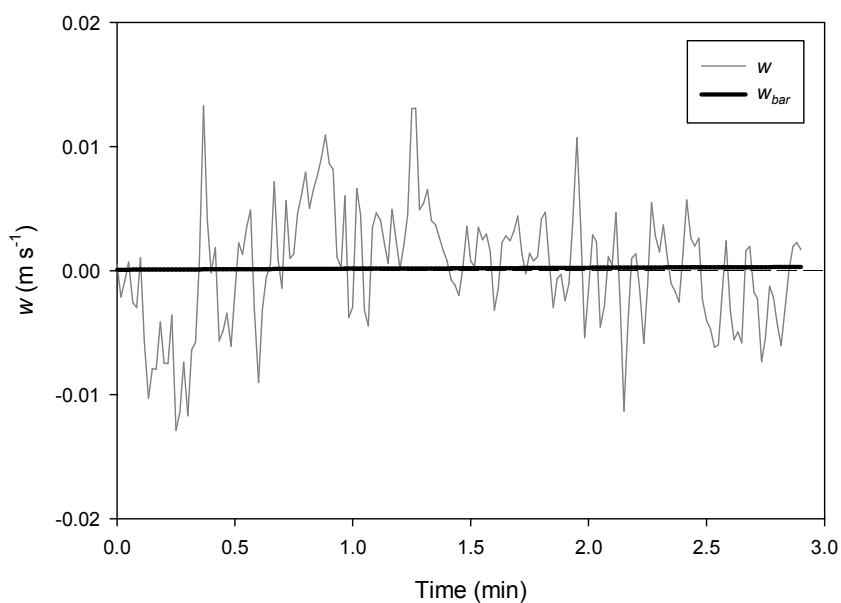


Figure E.35. Vertical velocity and corresponding linear trend for Kittery tidal flow burst, block 17748-19140 (filtered to 1 Hz for clarity).

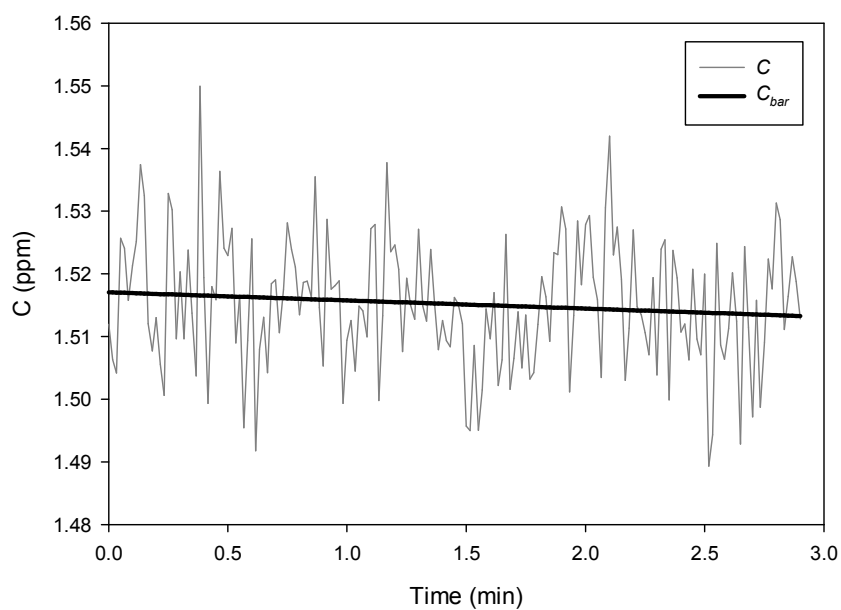


Figure E.36. DOC concentration and corresponding linear trend for Kittery tidal flow burst, block 17748-19140 (filtered to 1 Hz for clarity).

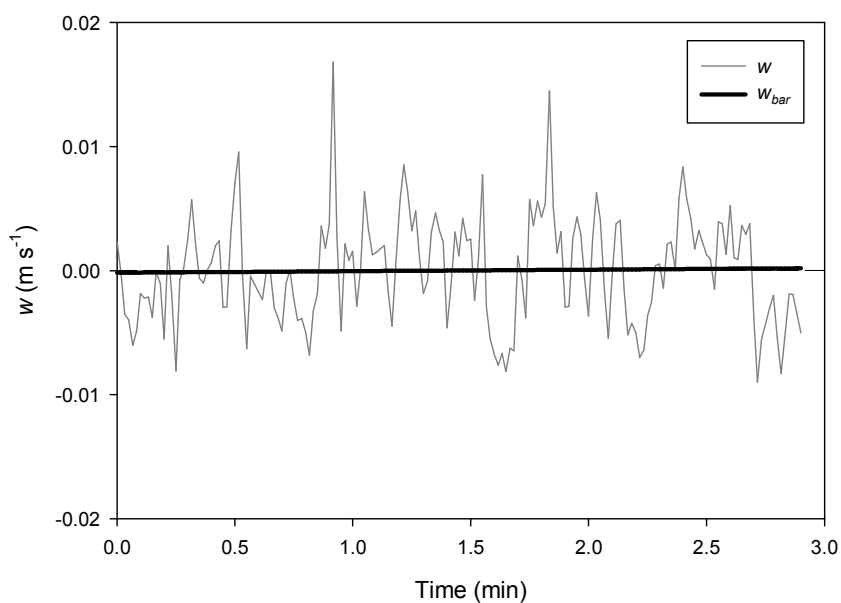


Figure E.37. Vertical velocity and corresponding linear trend for Kittery tidal flow burst, block 19140-20532 (filtered to 1 Hz for clarity).

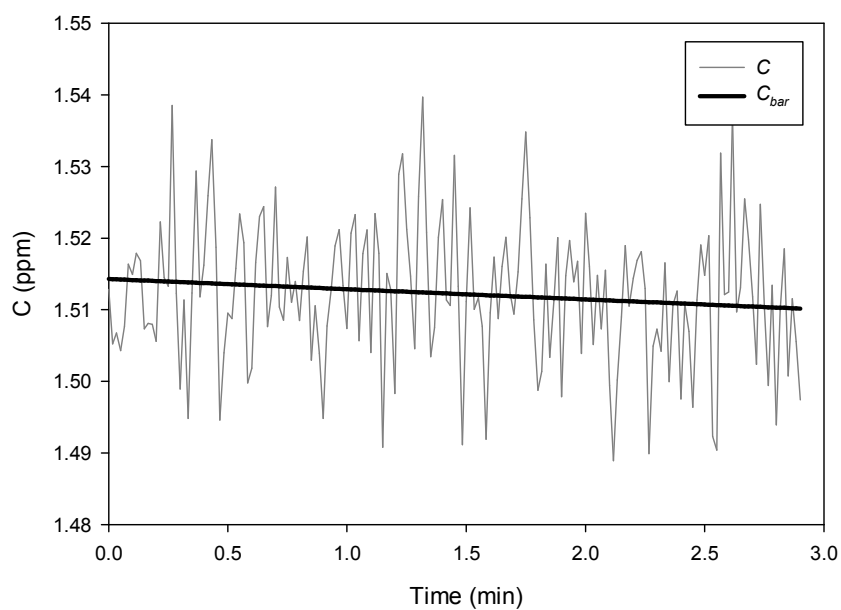


Figure E.38. DOC concentration and corresponding linear trend for Kittery tidal flow burst, block 19140-20532 (filtered to 1 Hz for clarity).

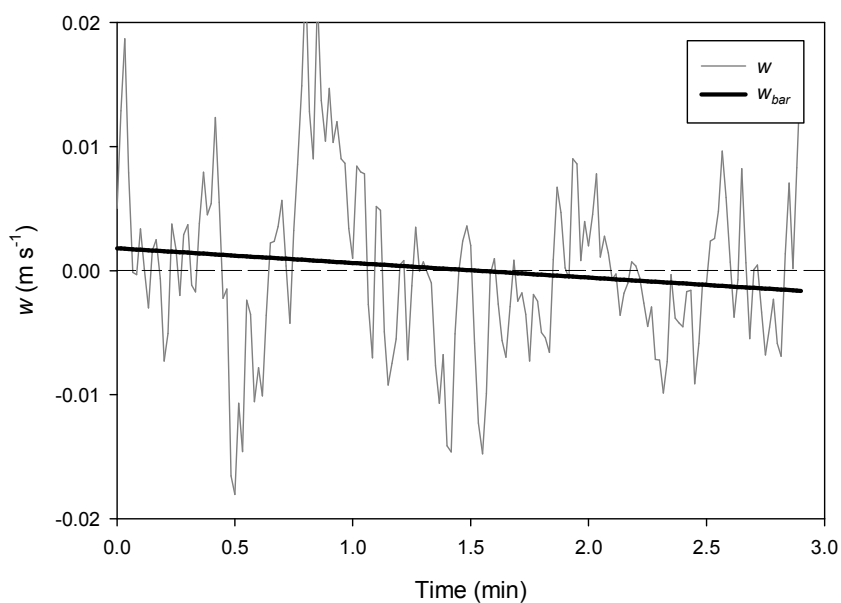


Figure E.39. Vertical velocity and corresponding linear trend for Kittery tidal flow burst, block 20532-21924 (filtered to 1 Hz for clarity).

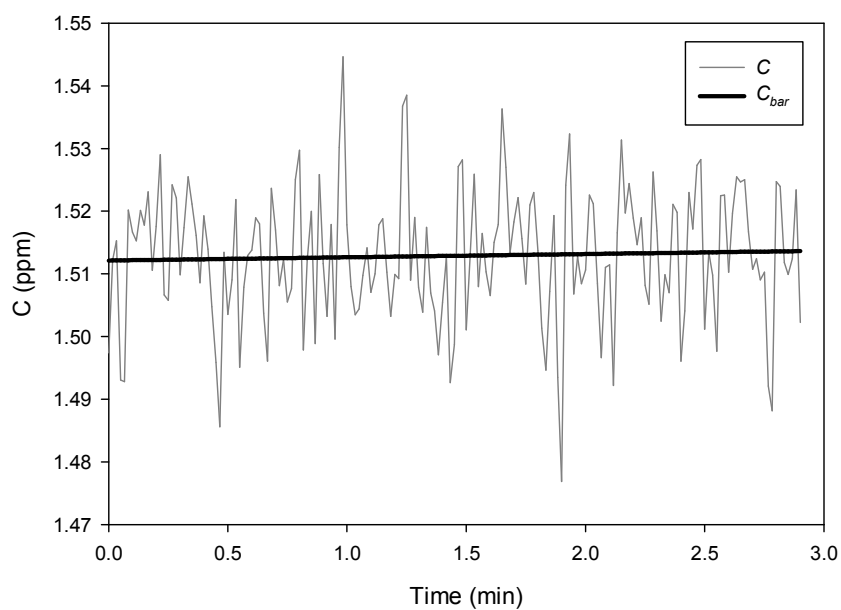


Figure E.40. DOC concentration and corresponding linear trend for Kittery tidal flow burst, block 20532-21924 (filtered to 1 Hz for clarity).

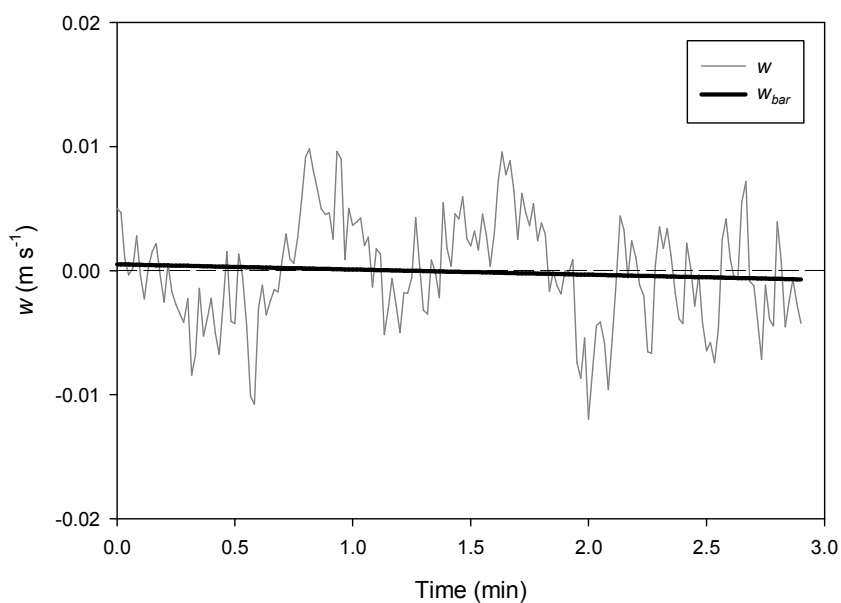


Figure E.41. Vertical velocity and corresponding linear trend for Kittery tidal flow burst, block 21924-23316 (filtered to 1 Hz for clarity).

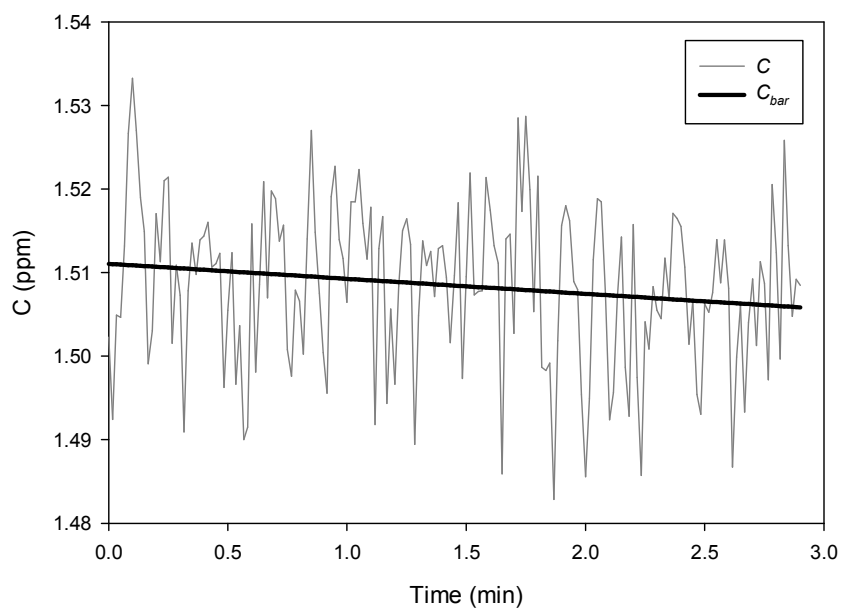


Figure E.42. DOC concentration and corresponding linear trend for Kittery tidal flow burst, block 21924-23316 (filtered to 1 Hz for clarity).

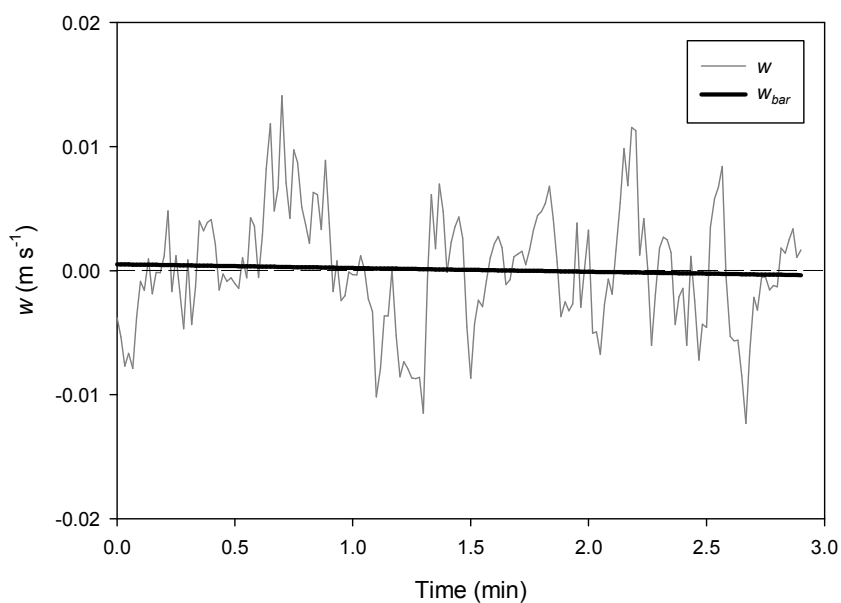


Figure E.43. Vertical velocity and corresponding linear trend for Kittery tidal flow burst, block 23316-24708 (filtered to 1 Hz for clarity).

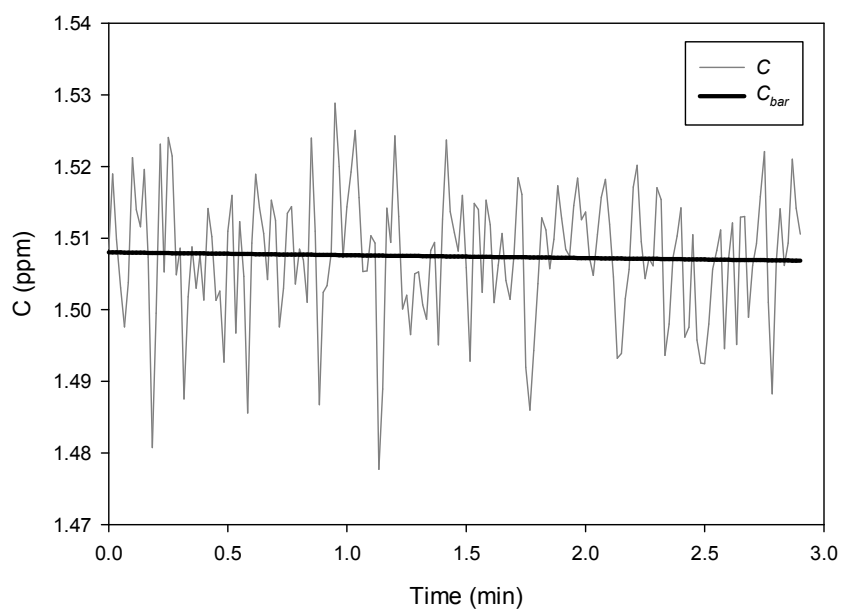


Figure E.44. DOC concentration and corresponding linear trend for Kittery tidal flow burst, block 23316-24708 (filtered to 1 Hz for clarity).

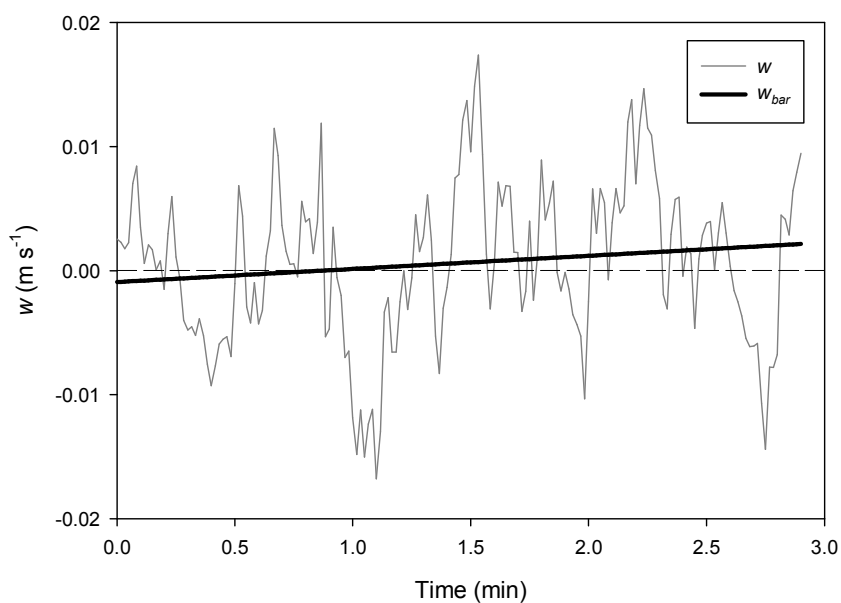


Figure E.45. Vertical velocity and corresponding linear trend for Kittery tidal flow burst, block 24708-26100 (filtered to 1 Hz for clarity).

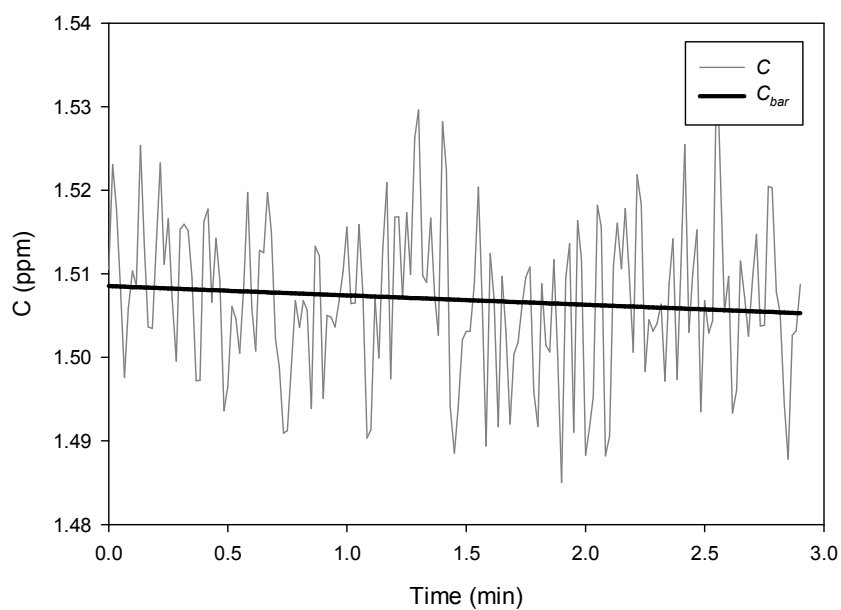


Figure E.46. DOC concentration and corresponding linear trend for Kittery tidal flow burst, block 24708-26100 (filtered to 1 Hz for clarity).

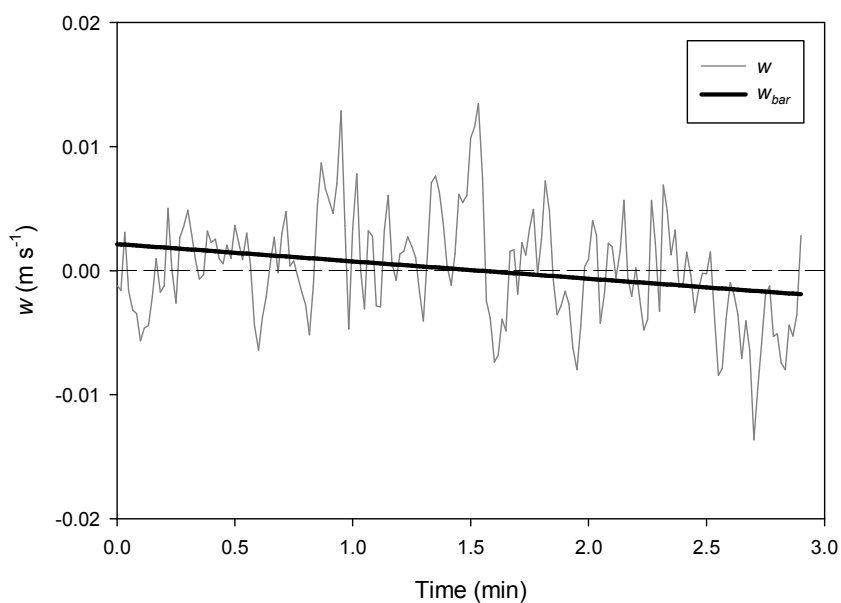


Figure E.47. Vertical velocity and corresponding linear trend for Kittery tidal flow burst, block 26100-27492 (filtered to 1 Hz for clarity).

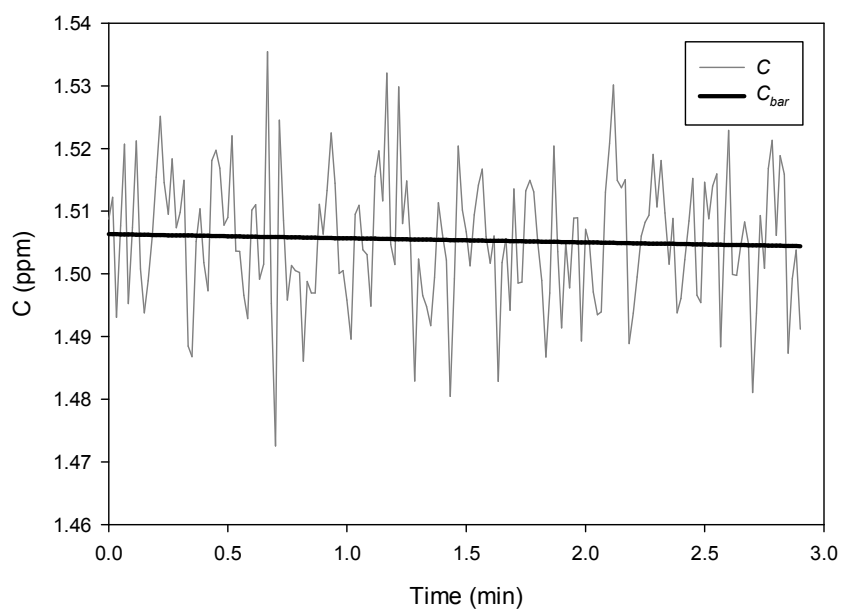


Figure E.48. DOC concentration and corresponding linear trend for Kittery tidal flow burst, block 26100-27492 (filtered to 1 Hz for clarity).

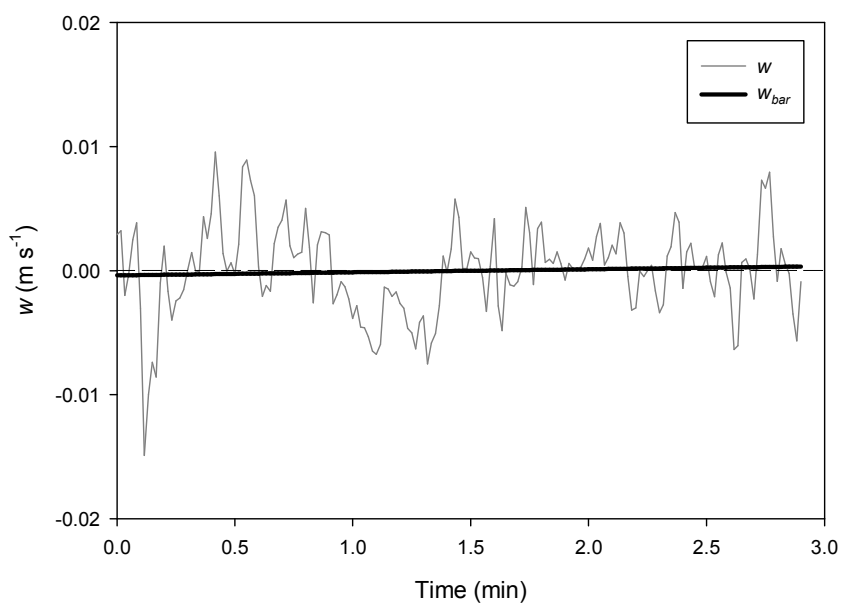


Figure E.49. Vertical velocity and corresponding linear trend for Kittery tidal flow burst, block 27492-28884 (filtered to 1 Hz for clarity).

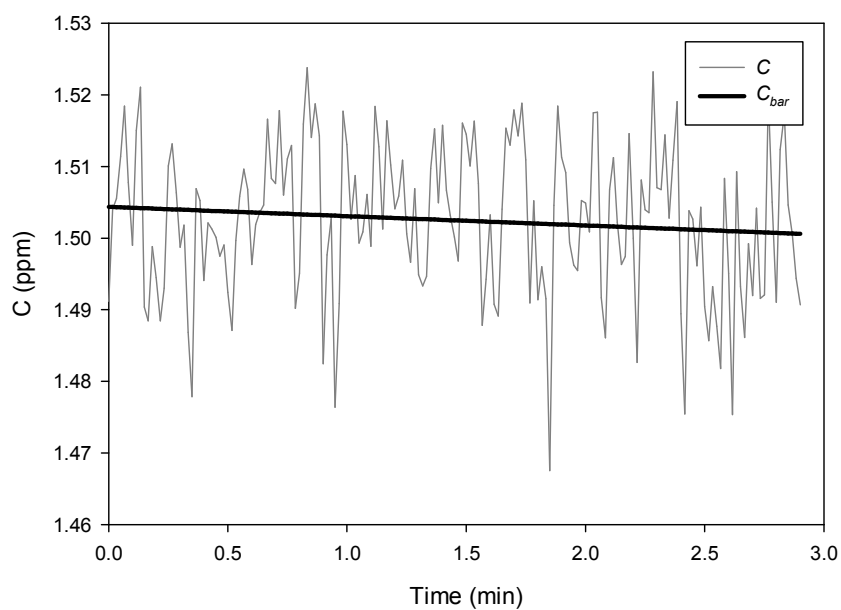


Figure E.50. DOC concentration and corresponding linear trend for Kittery tidal flow burst, block 27492-28884 (filtered to 1 Hz for clarity).

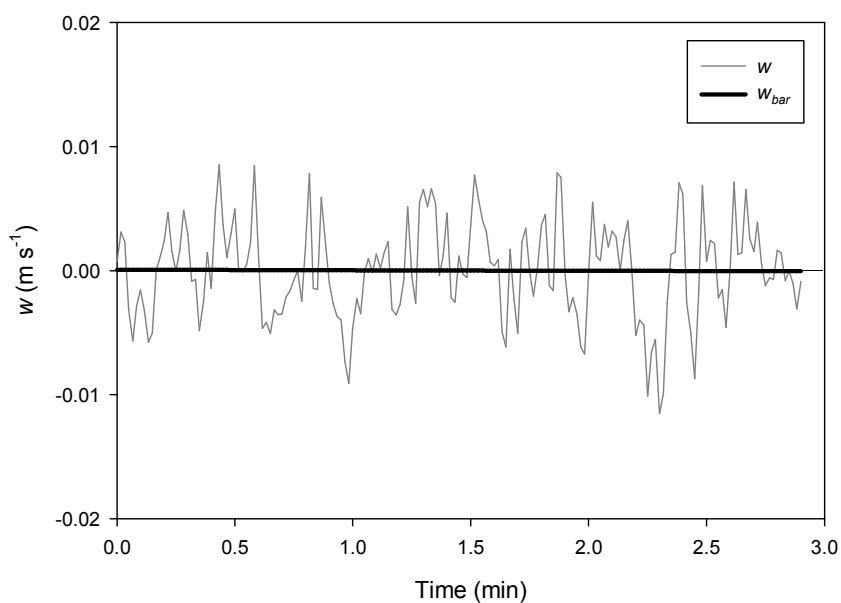


Figure E.51. Vertical velocity and corresponding linear trend for Kittery tidal flow burst, block 28884-30276 (filtered to 1 Hz for clarity).

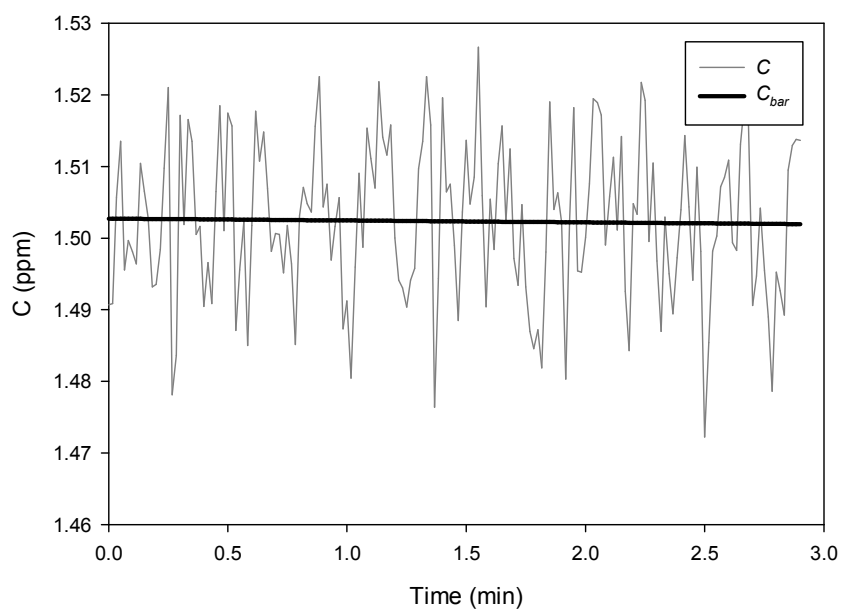


Figure E.52. DOC concentration and corresponding linear trend for Kittery tidal flow burst, block 28884-30276 (filtered to 1 Hz for clarity).

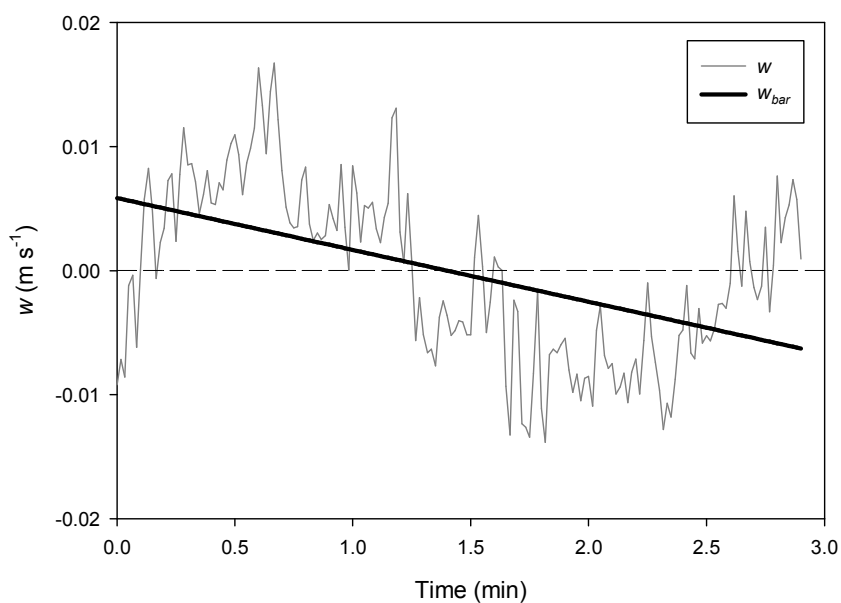


Figure E.53. Vertical velocity and corresponding linear trend for Kittery tidal flow burst, block 30276-31668 (filtered to 1 Hz for clarity).

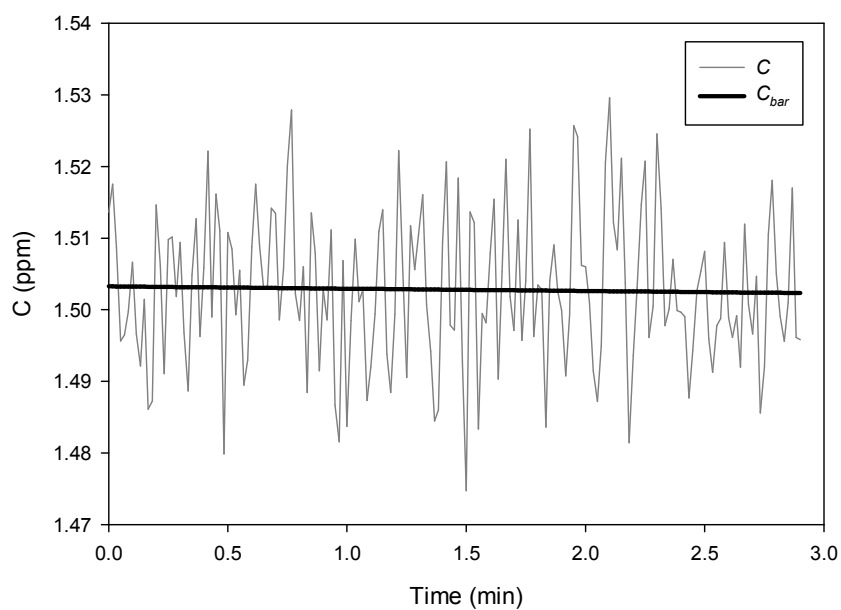


Figure E.54. DOC concentration and corresponding linear trend for Kittery tidal flow burst, block 30276-31668 (filtered to 1 Hz for clarity).

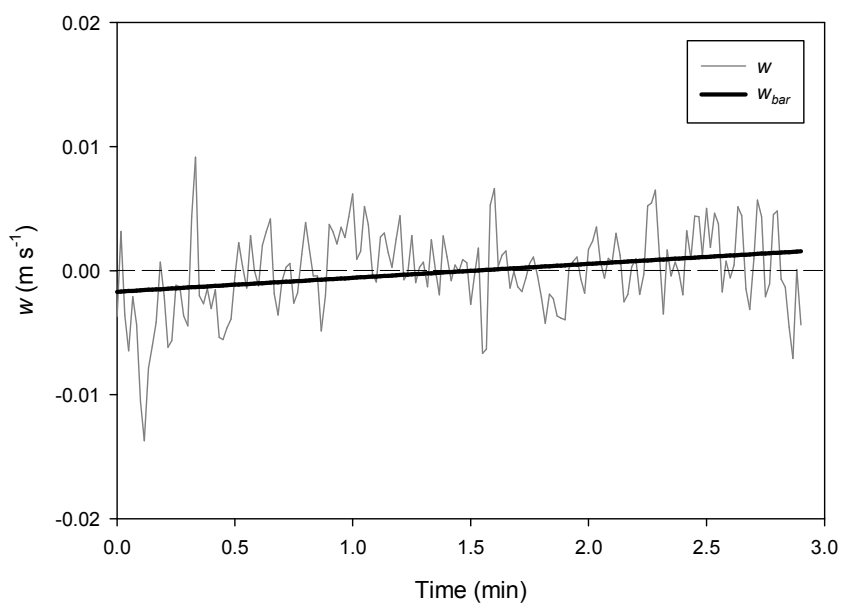


Figure E.55. Vertical velocity and corresponding linear trend for Kittery tidal flow burst, block 31688-33060 (filtered to 1 Hz for clarity).

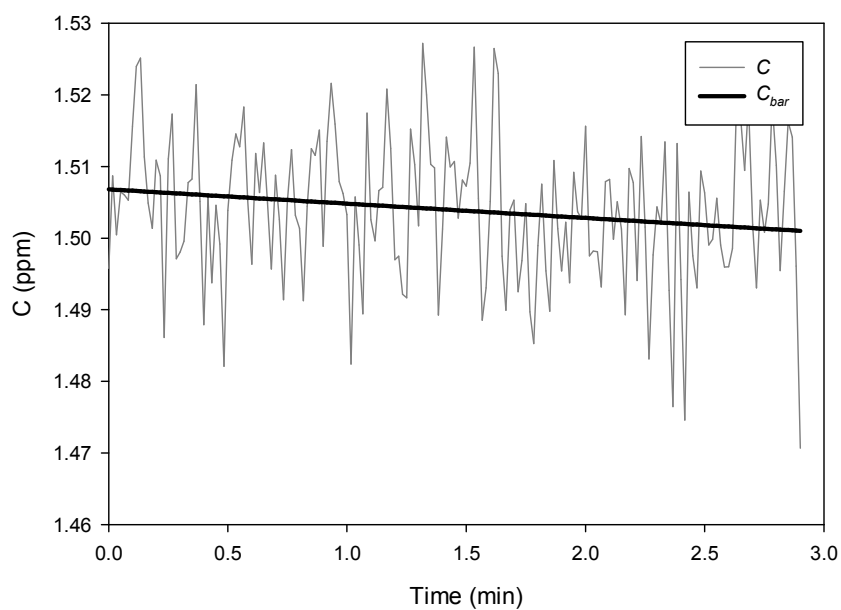


Figure E.56. DOC concentration and corresponding linear trend for Kittery tidal flow burst, block 31688-33060 (filtered to 1 Hz for clarity).

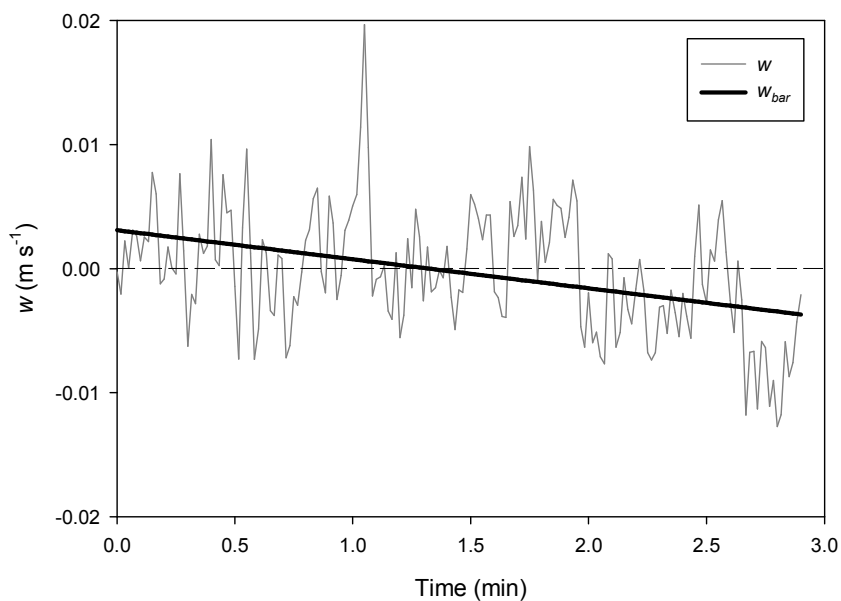


Figure E.57. Vertical velocity and corresponding linear trend for Kittery tidal flow burst, block 33060-34452 (filtered to 1 Hz for clarity).

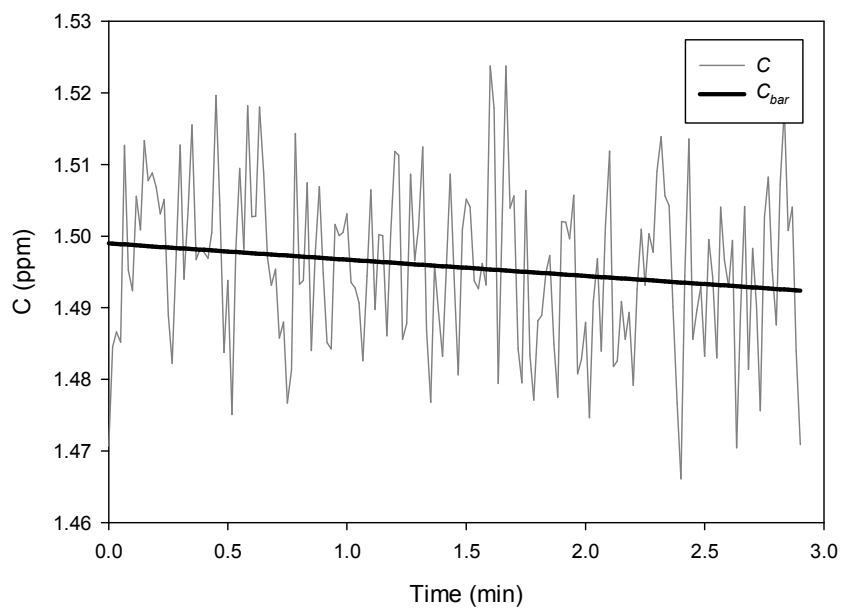


Figure E.58. DOC concentration and corresponding linear trend for Kittery tidal flow burst, block 33060-34452 (filtered to 1 Hz for clarity).

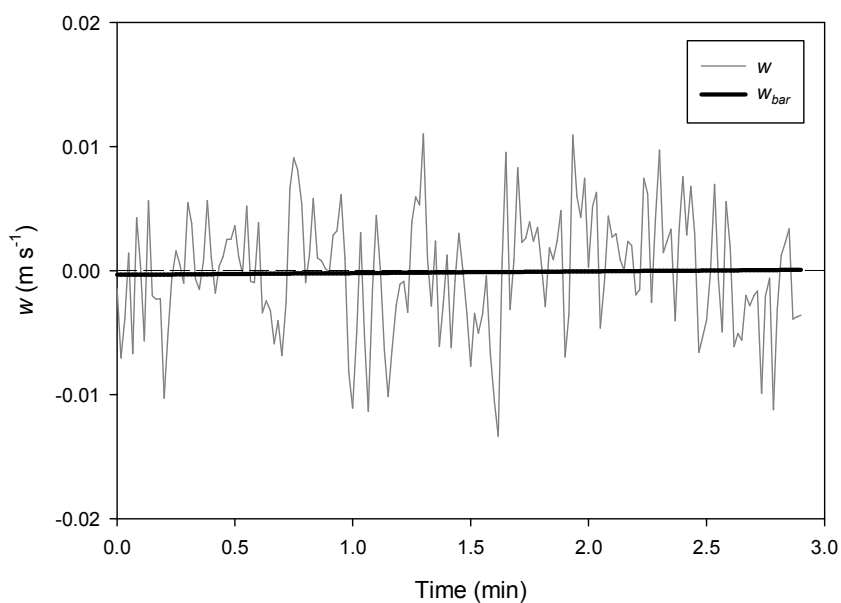


Figure E.59. Vertical velocity and corresponding linear trend for Kittery tidal flow burst, block 34452-35844 (filtered to 1 Hz for clarity).

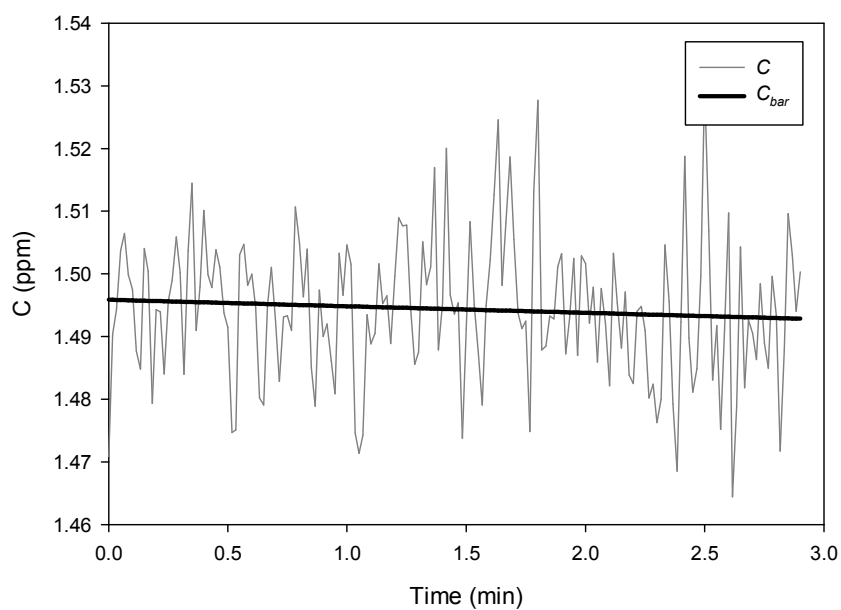


Figure E.60. DOC concentration and corresponding linear trend for Kittery tidal flow burst, block 34452-35844 (filtered to 1 Hz for clarity).

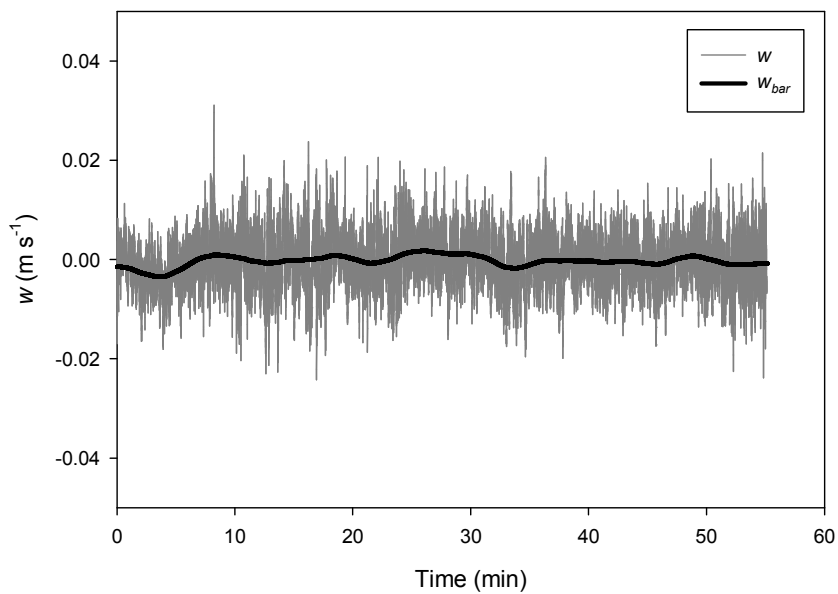


Figure E.61. Vertical velocity and corresponding moving average trend for Kittery tidal flow burst.

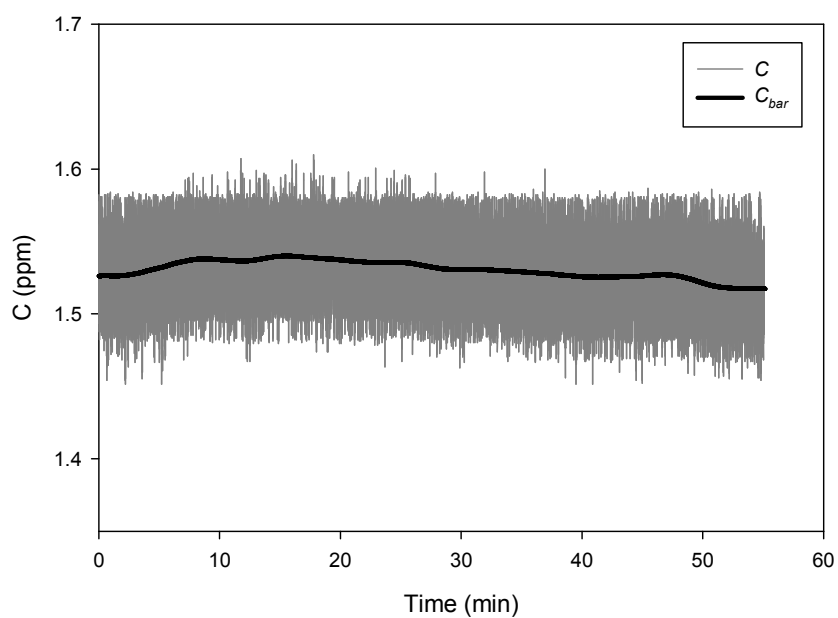


Figure E.62. DOC concentration and corresponding moving average trend for Kittery tidal flow burst.

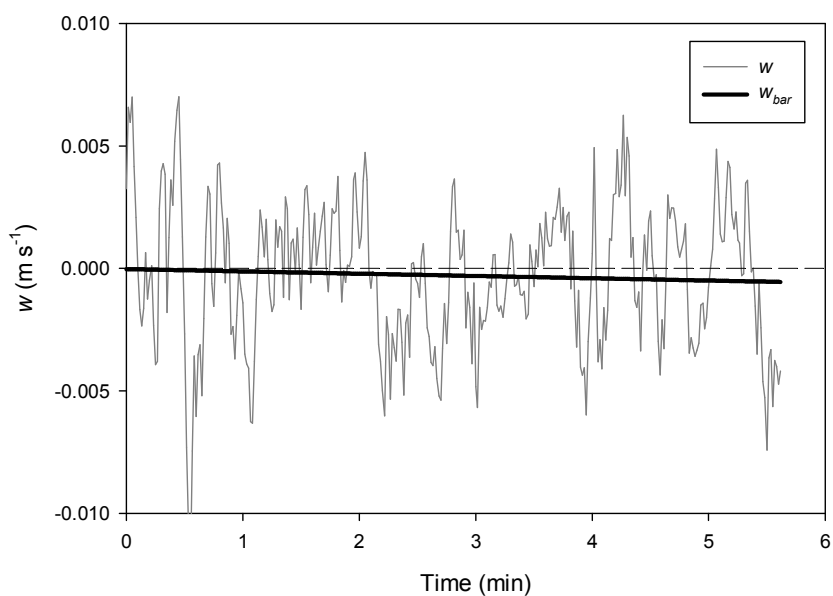


Figure E.63. Vertical velocity and corresponding linear trend for Kittery tidal ebb burst, block 128348-131044 (filtered to 1 Hz for clarity).

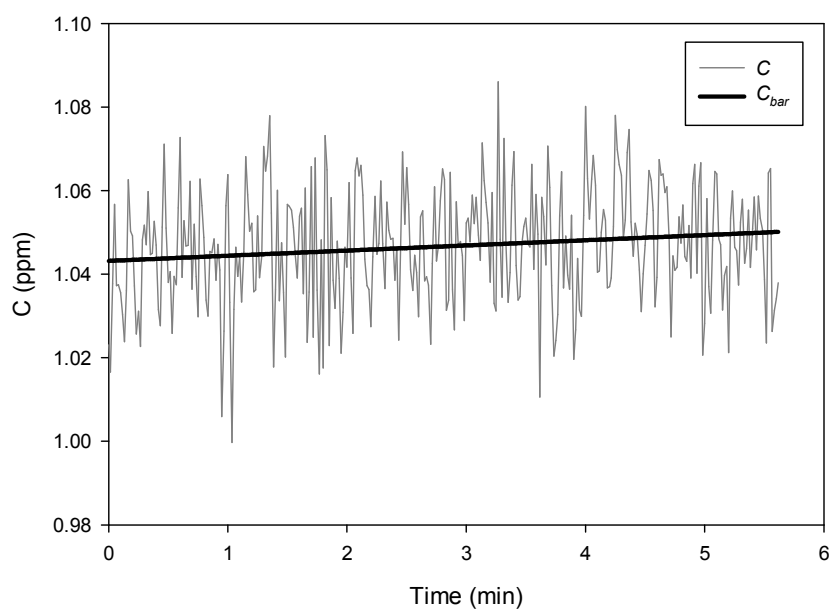


Figure E.64. DOC concentration and corresponding linear trend for Kittery tidal ebb burst, block 128348-131044 (filtered to 1 Hz for clarity).

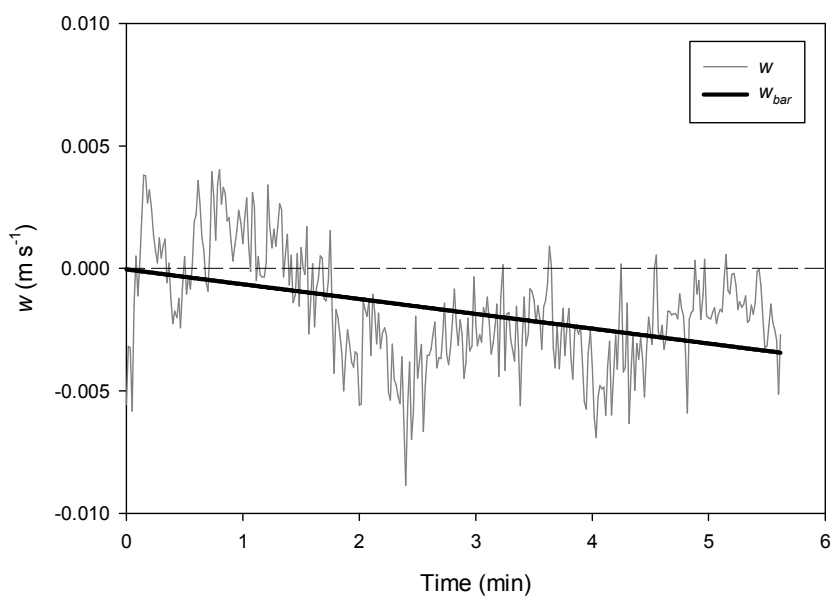


Figure E.65. Vertical velocity and corresponding linear trend for Kittery tidal ebb burst, block 131044-133740 (filtered to 1 Hz for clarity).

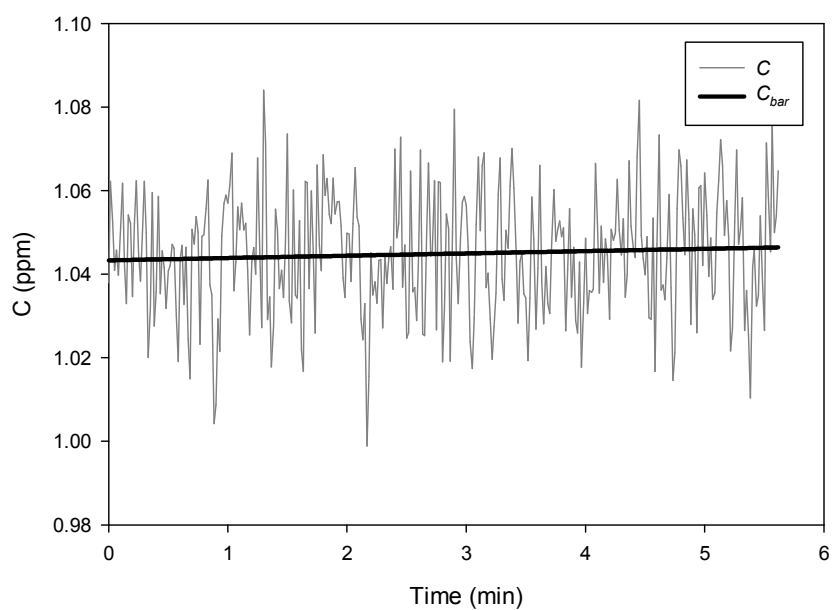


Figure E.66. DOC concentration and corresponding linear trend for Kittery tidal ebb burst, block 131044-133740 (filtered to 1 Hz for clarity).

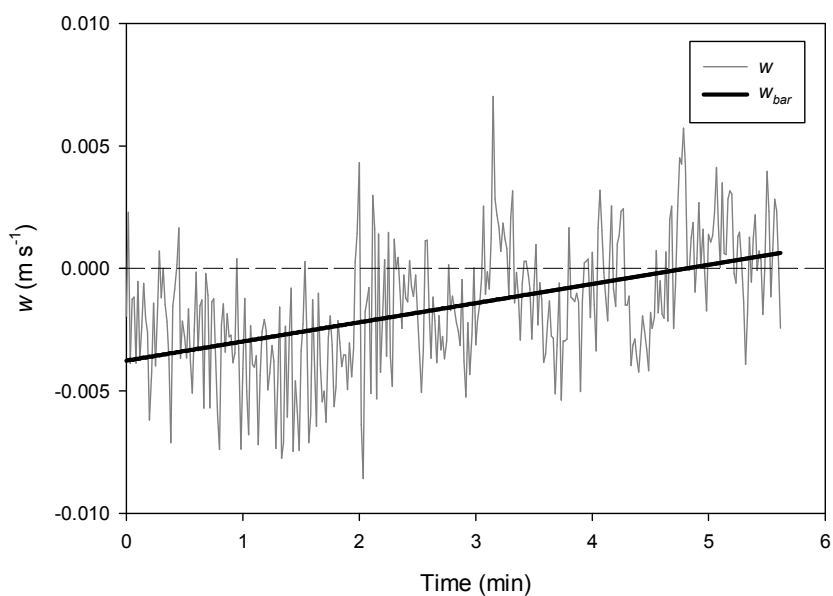


Figure E.67. Vertical velocity and corresponding linear trend for Kittery tidal ebb burst, block 133740-136436 (filtered to 1 Hz for clarity).

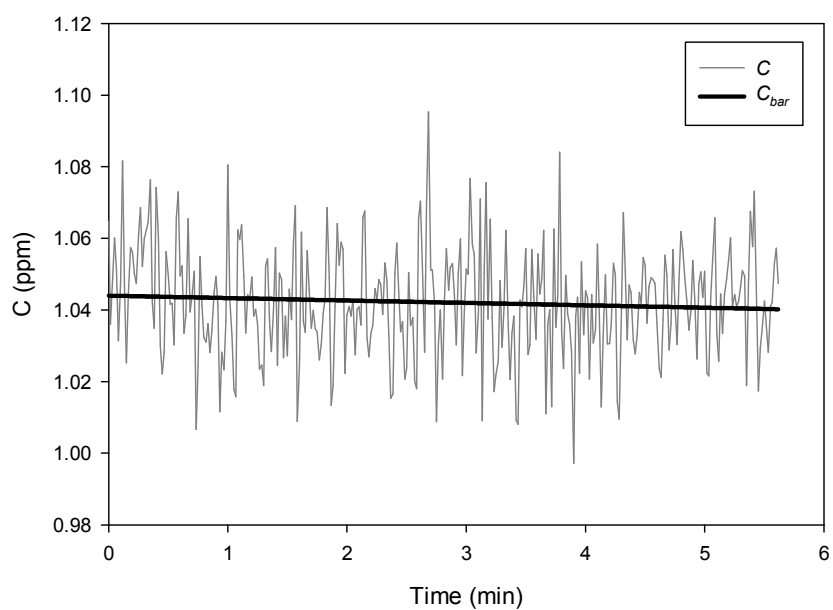


Figure E.68. DOC concentration and corresponding linear trend for Kittery tidal ebb burst, block 133740-136436 (filtered to 1 Hz for clarity).

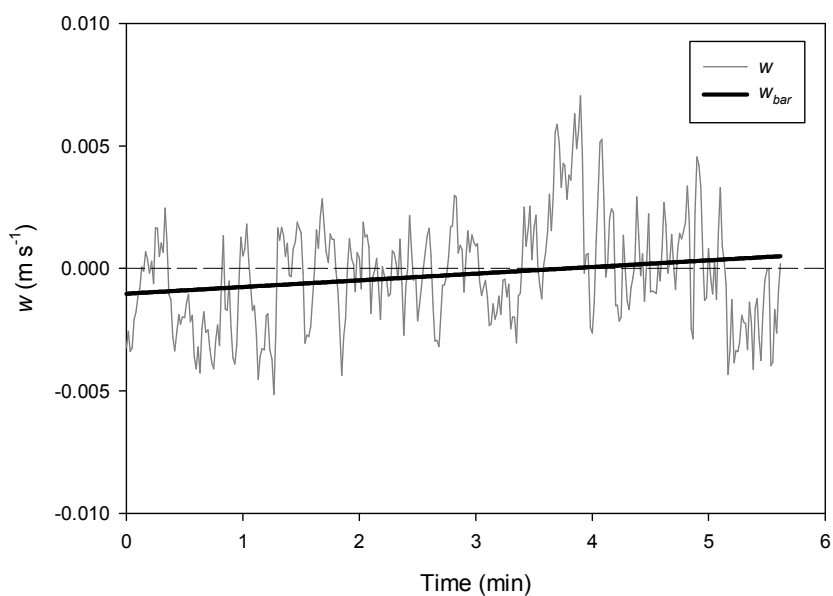


Figure E.69. Vertical velocity and corresponding linear trend for Kittery tidal ebb burst, block 136436-139132 (filtered to 1 Hz for clarity).

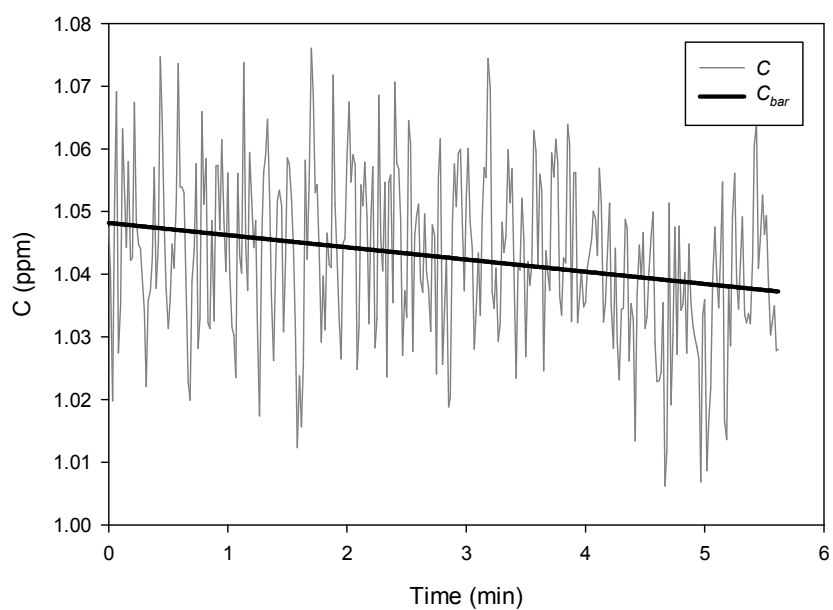


Figure E.70. DOC concentration and corresponding linear trend for Kittery tidal ebb burst, block 136436-139132 (filtered to 1 Hz for clarity).

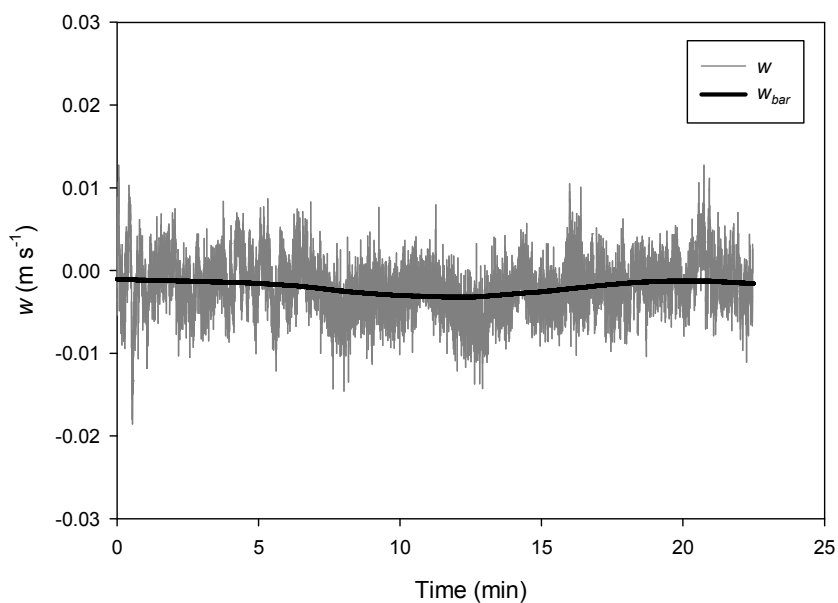


Figure E.71. Vertical velocity and corresponding moving average trend for Kittery tidal ebb burst.

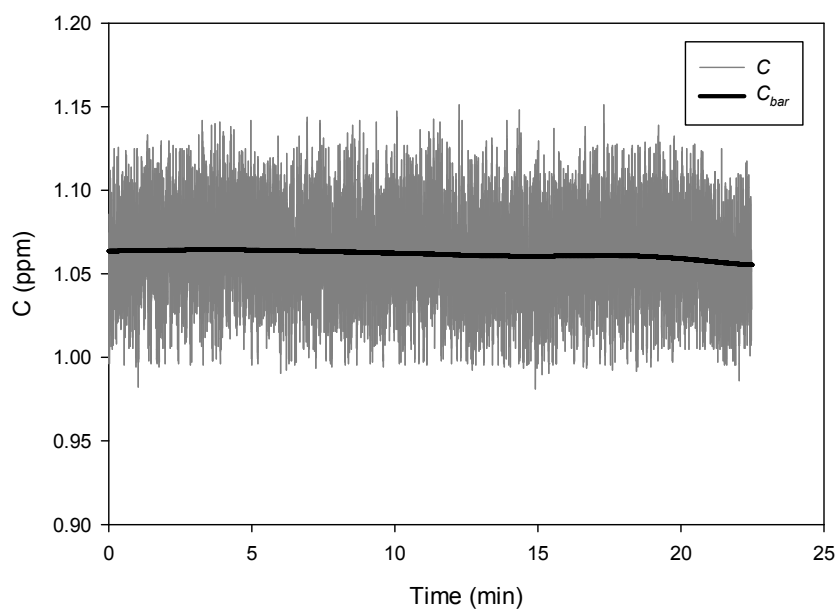
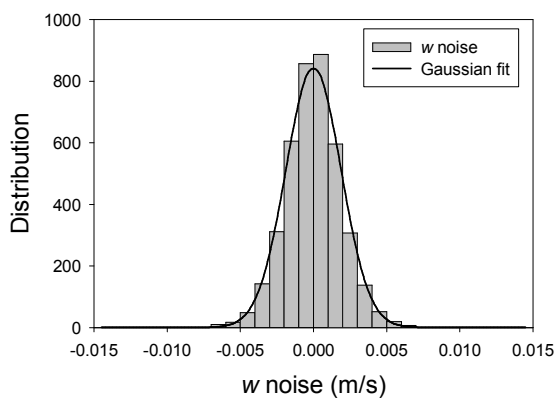


Figure E.72. DOC concentration and corresponding moving average trend for Kittery tidal ebb burst.

Appendix F: Noise distributions

a.



b.

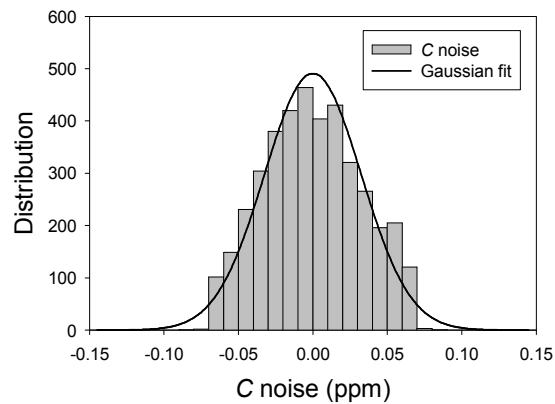
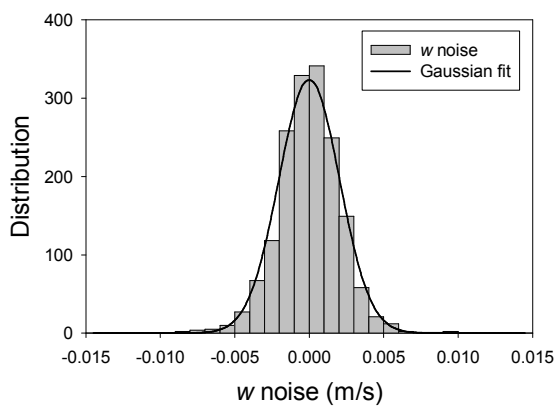


Figure F.1. Frankfort burst 1 noise distributions for (a.) w and (b.) C .

a.



b.

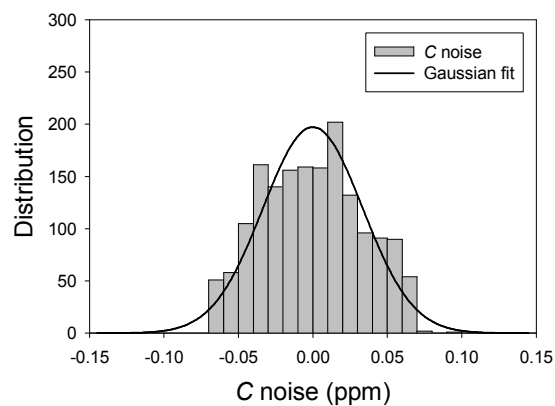
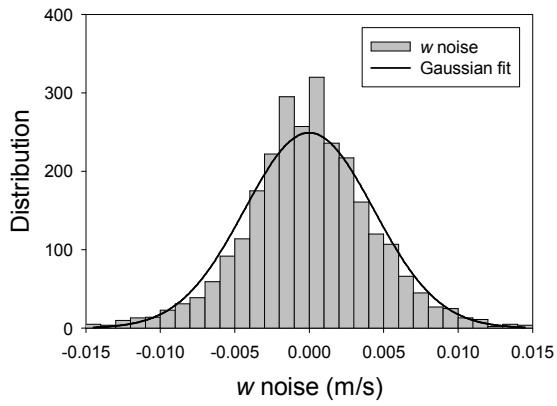


Figure F.2. Frankfort burst 2 noise distributions for (a.) w and (b.) C .

a.



b.

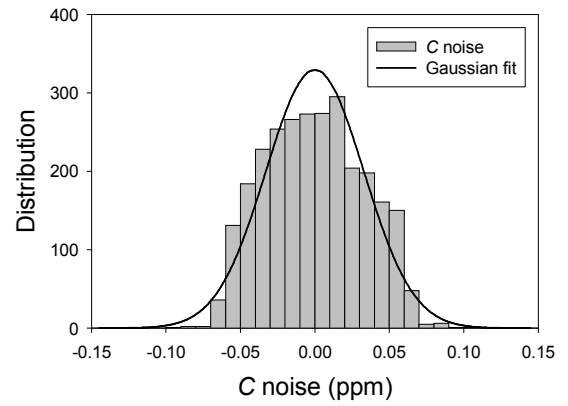


Figure F.3. Squamscott burst noise distributions for (a.) w and (b.) C .

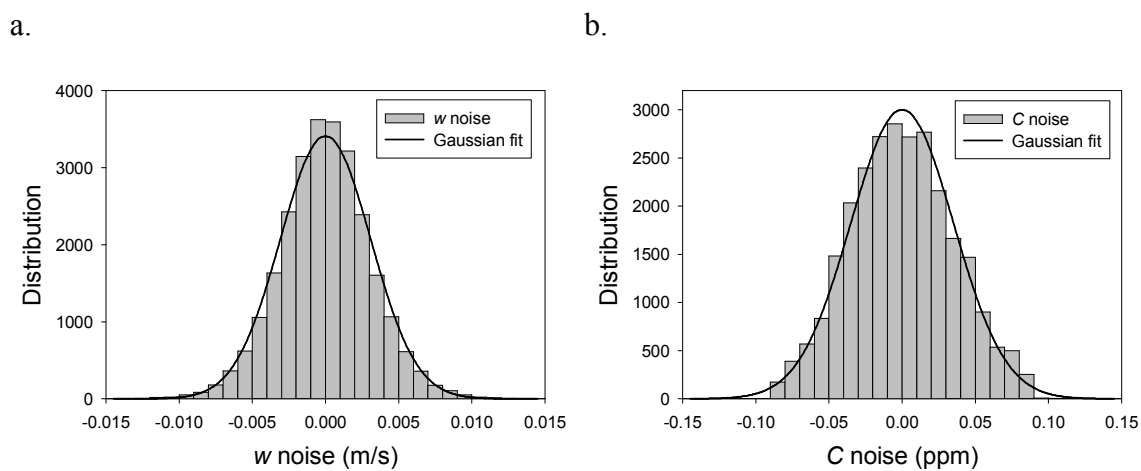


Figure F.4. Kittery tidal flow period noise distributions for (a.) w and (b.) C .

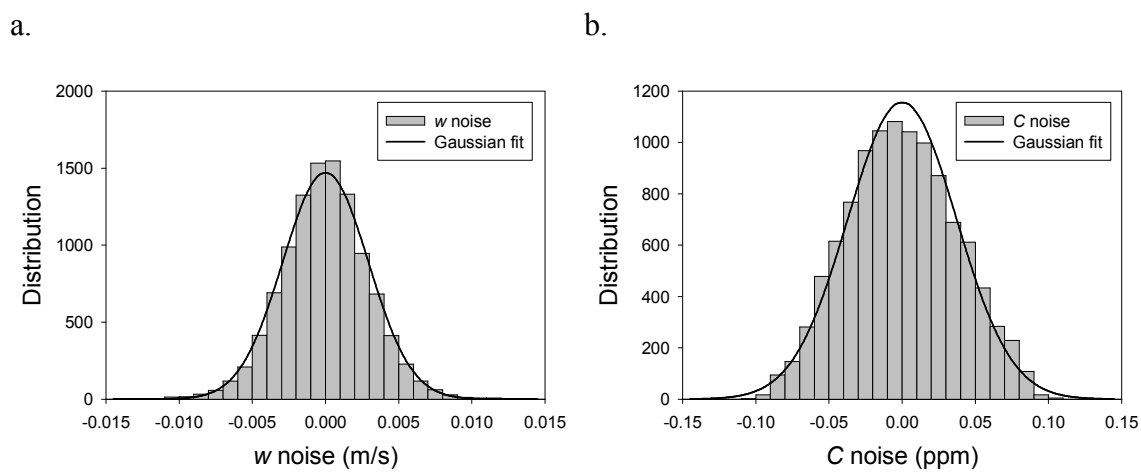


Figure F.5. Kittery tidal ebb period noise distributions for (a.) w and (b.) C .

**Appendix G: Normalized cumulative cospectra of fluctuations of vertical velocity
and concentration at 1 Hz**

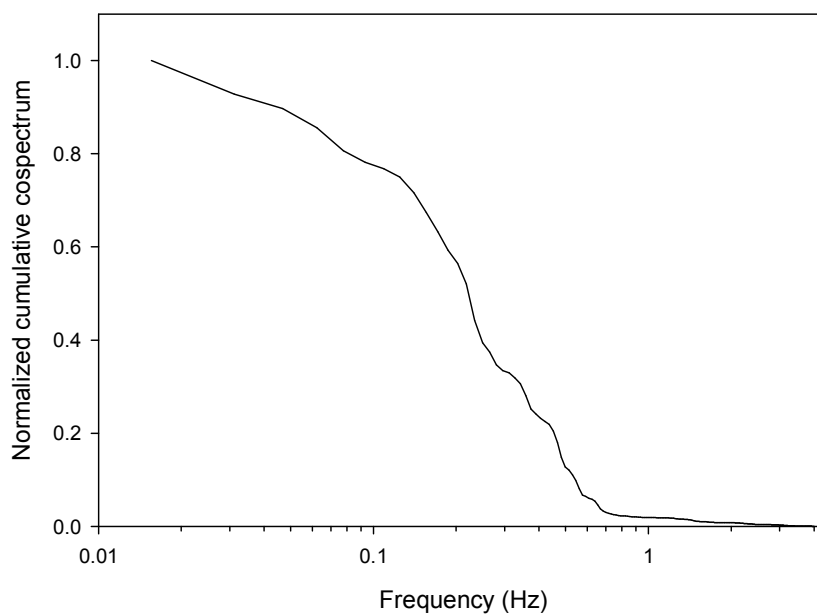


Figure G.1. Normalized cumulative cospectrum of w' and C' for Frankfort burst 1, block 77300-78100.

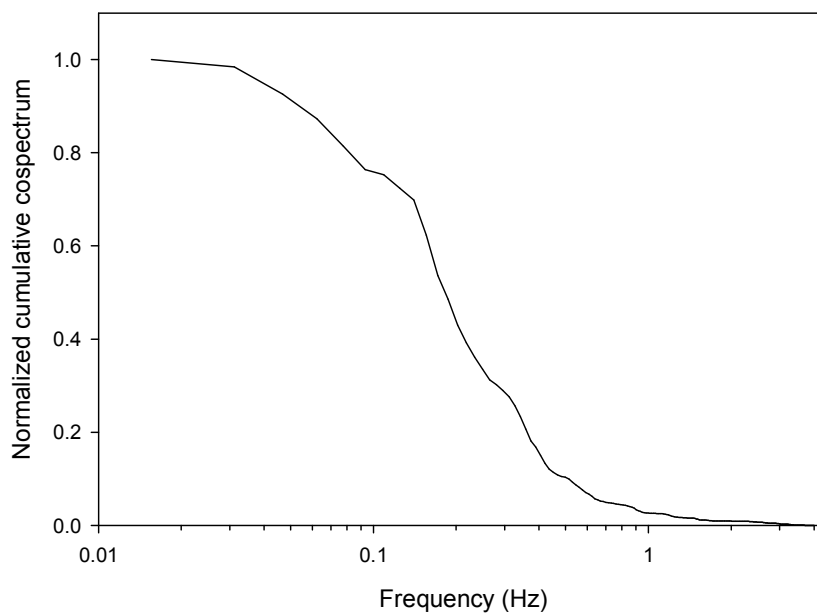


Figure G.2. Normalized cumulative cospectrum of w' and C' for Frankfort burst 1, block 78100-78900.

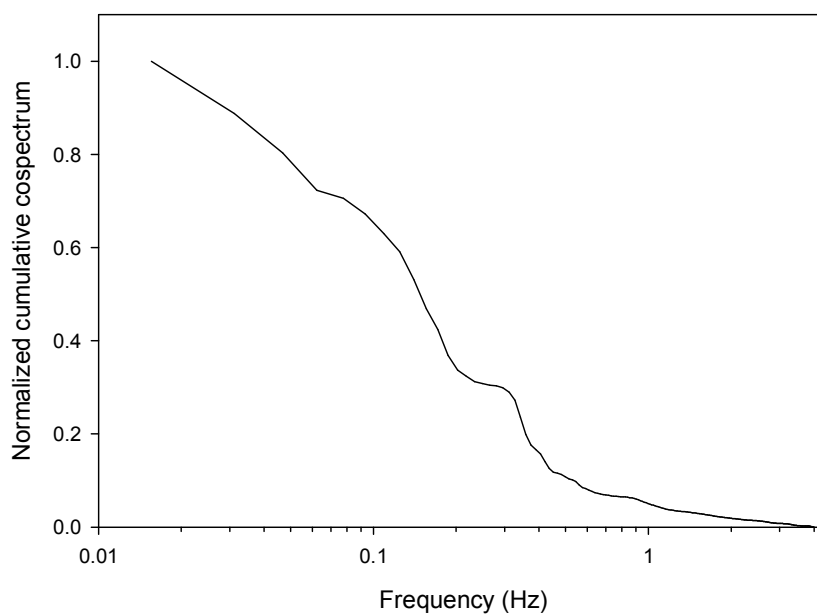


Figure G.3. Normalized cumulative cospectrum of w' and C' for Frankfort burst 1, block 78900-79700.

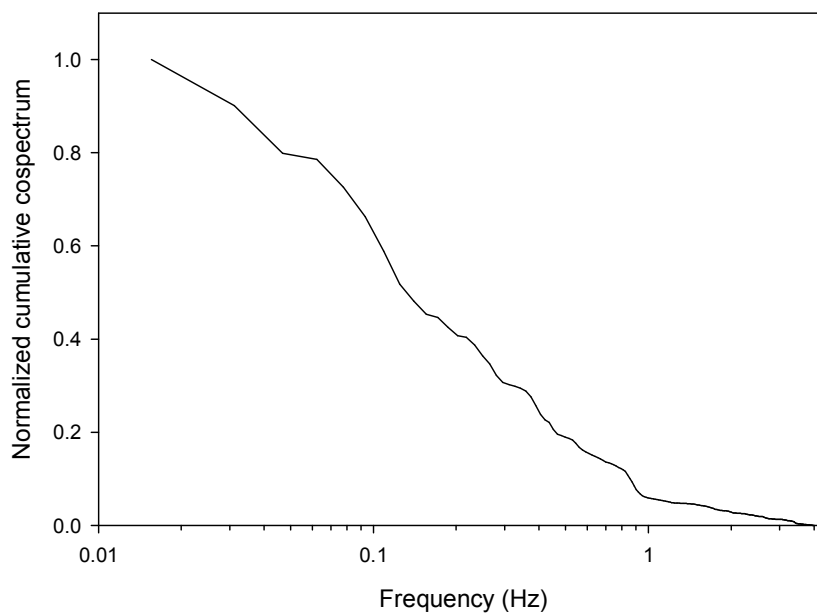


Figure G.4. Normalized cumulative cospectrum of w' and C' for Frankfort burst 1, block 79700-80500.

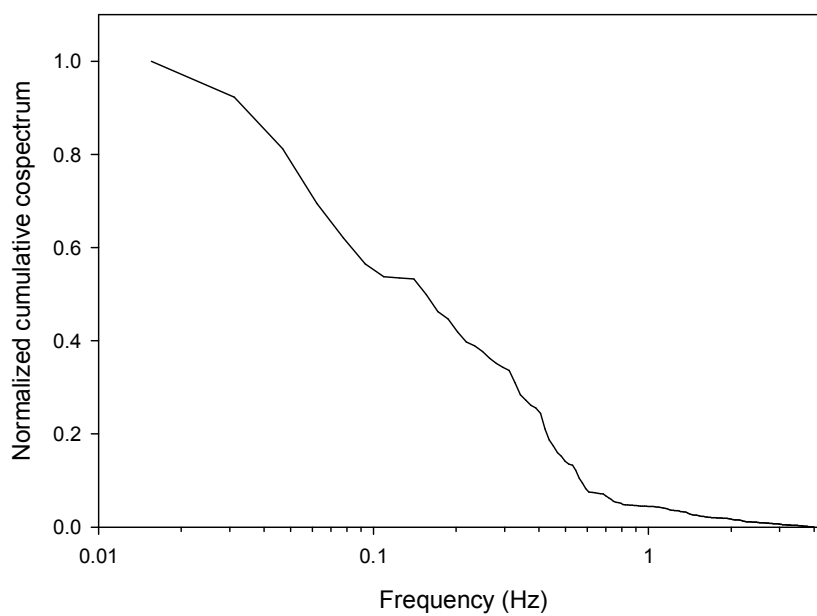


Figure G.5. Normalized cumulative cospectrum of w' and C' for Frankfort burst 1, block 80500-81300.

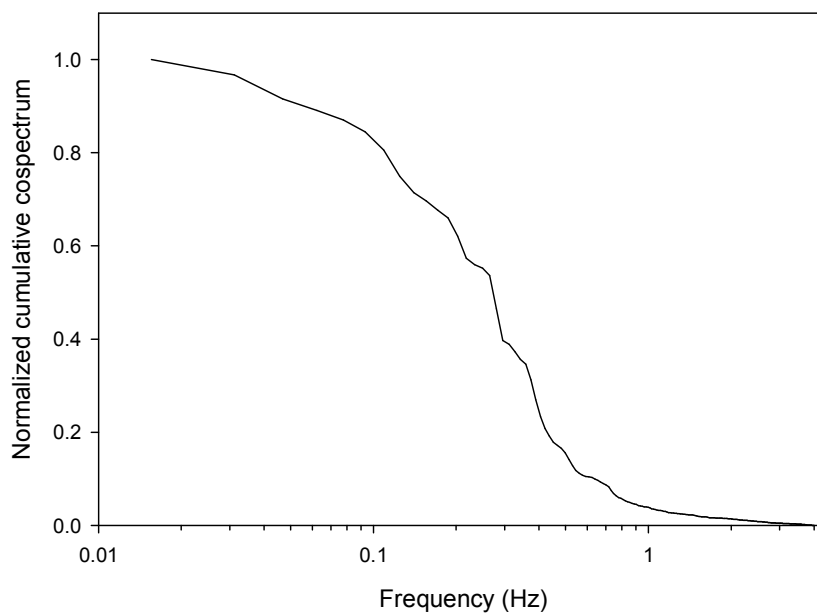


Figure G.6. Normalized cumulative cospectrum of w' and C' for Frankfort burst 2, block 88828-90484.

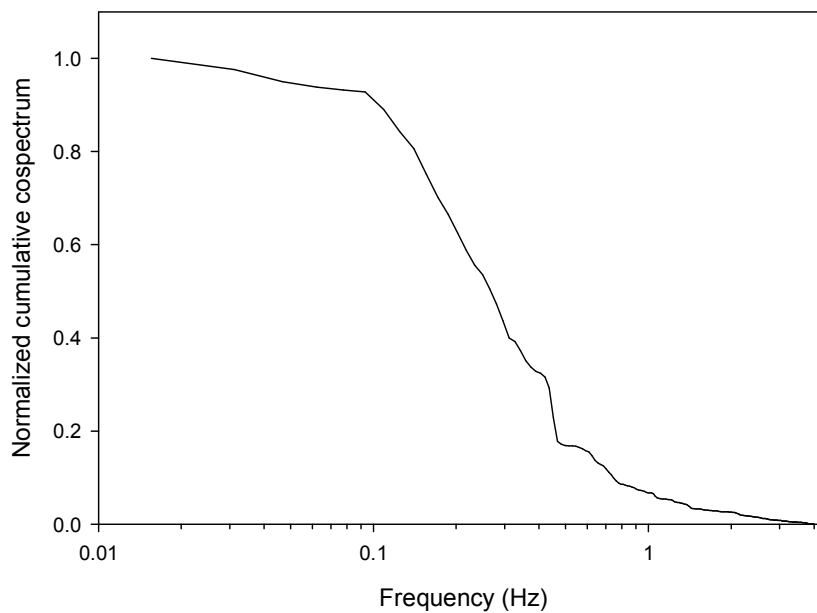


Figure G.7. Normalized cumulative cospectrum of w' and C' for Squamscott burst, block 103680-105040.

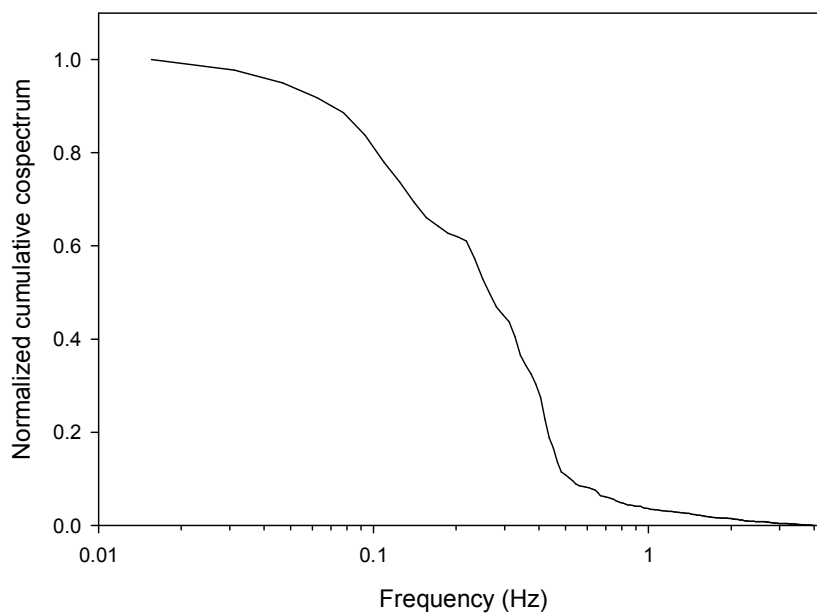


Figure G.8. Normalized cumulative cospectrum of w' and C' for Squamscott burst, block 105040-106400.

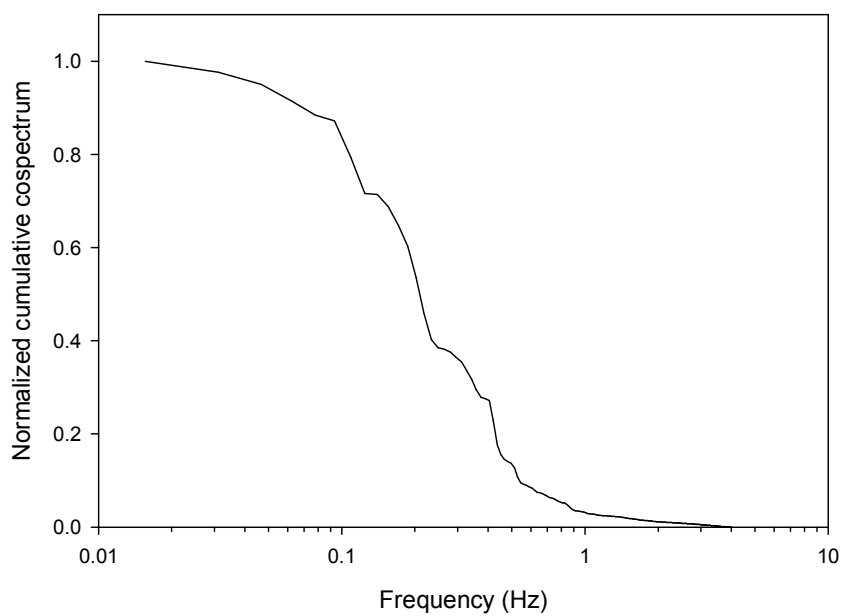


Figure G.9. Normalized cumulative cospectrum of w' and C' for Kittery tidal flow burst, block 9396-10788.

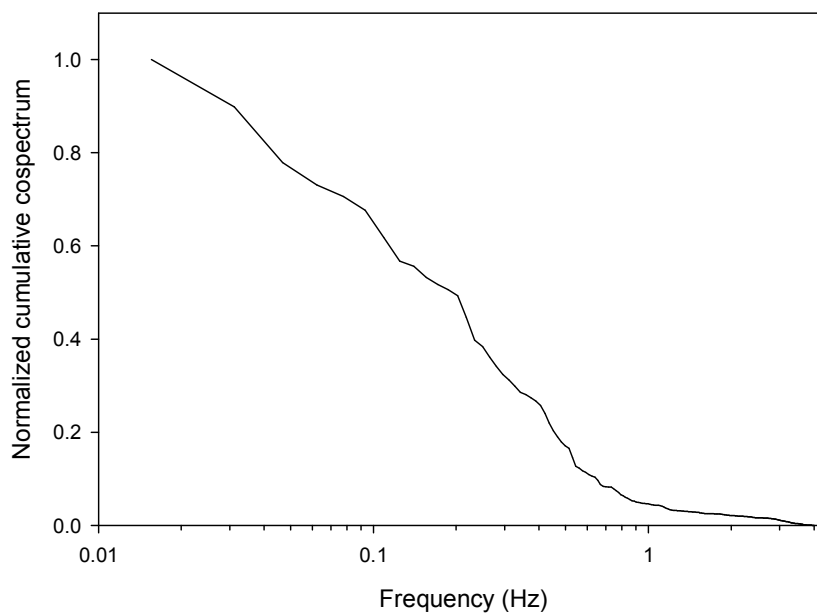


Figure G.10. Normalized cumulative cospectrum of w' and C' for Kittery tidal flow burst, block 10788-12180.

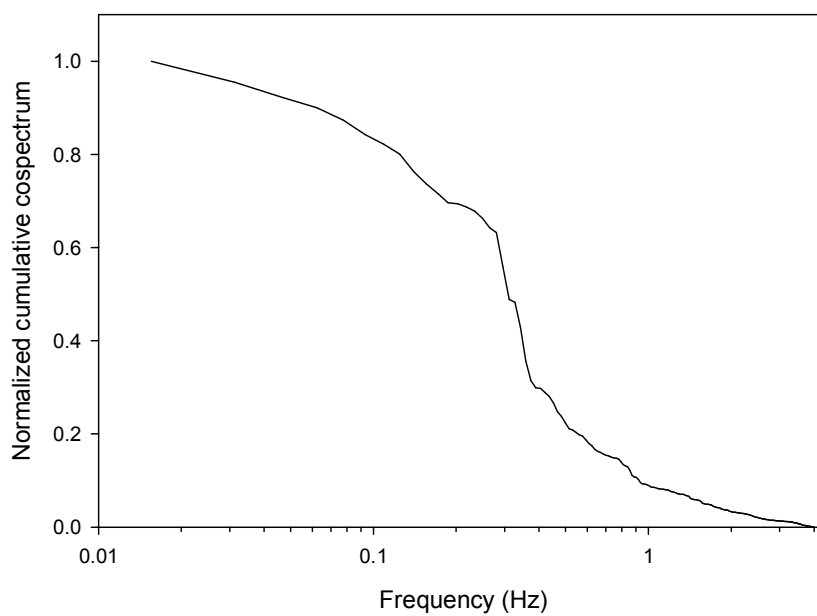


Figure G.11. Normalized cumulative cospectrum of w' and C' for Kittery tidal flow burst, block 12180-13572.

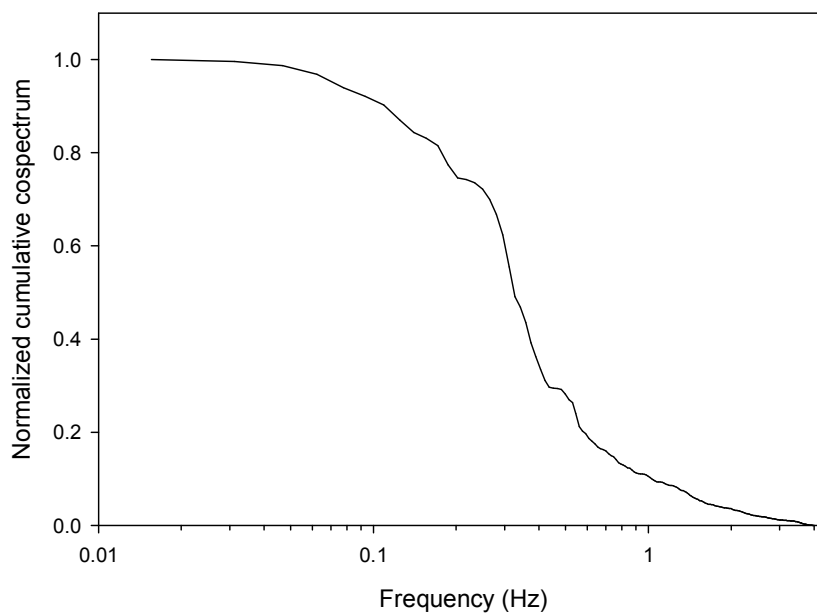


Figure G.12. Normalized cumulative cospectrum of w' and C' for Kittery tidal flow burst, block 13572-14964.

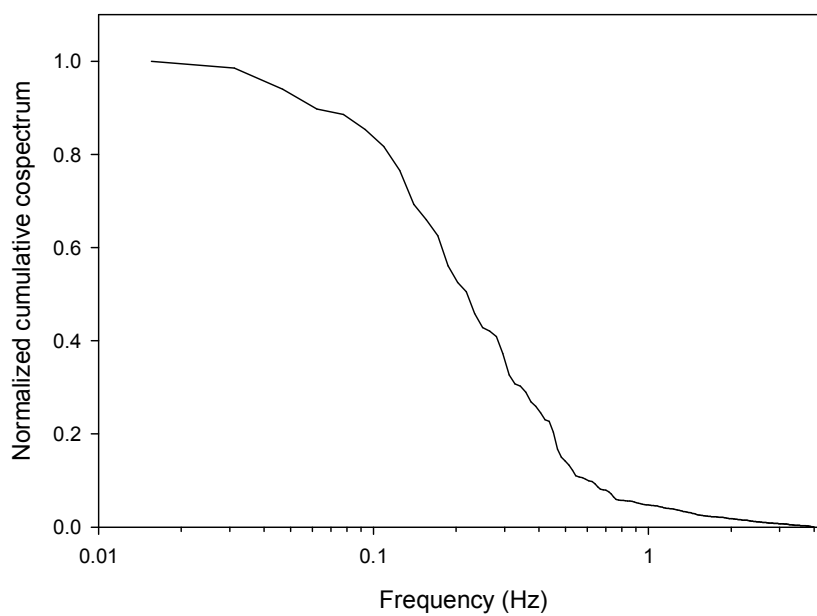


Figure G.13. Normalized cumulative cospectrum of w' and C' for Kittery tidal flow burst, block 14964-16356.

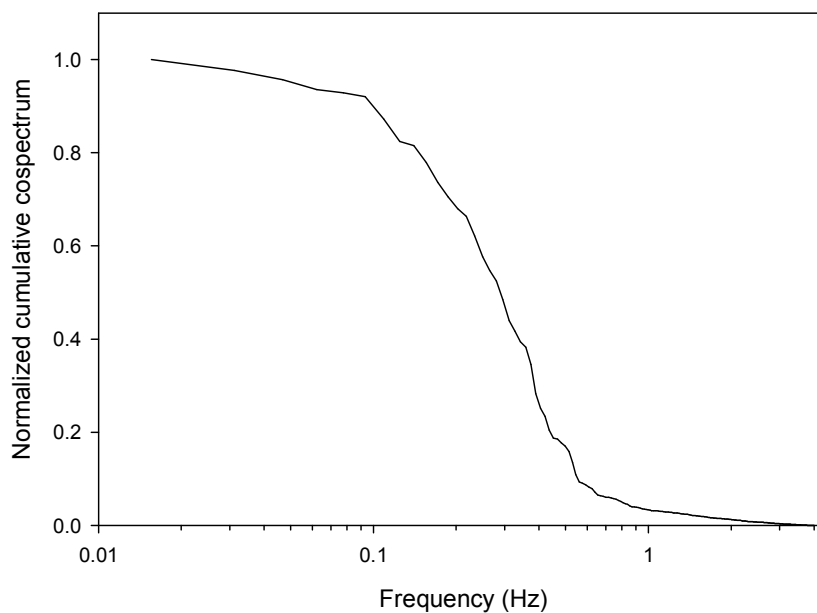


Figure G.14. Normalized cumulative cospectrum of w' and C' for Kittery tidal flow burst, block 16356-17748.

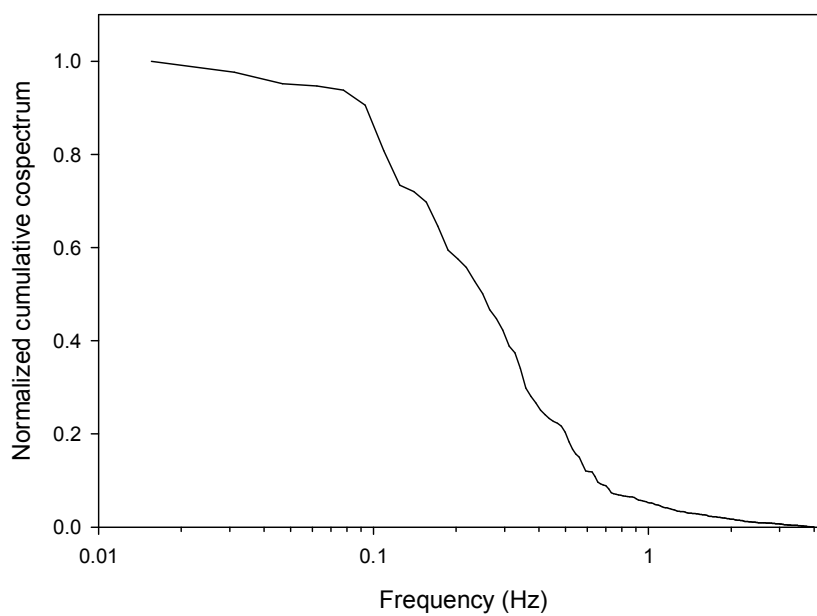


Figure G.15. Normalized cumulative cospectrum of w' and C' for Kittery tidal flow burst, block 17748-19140.

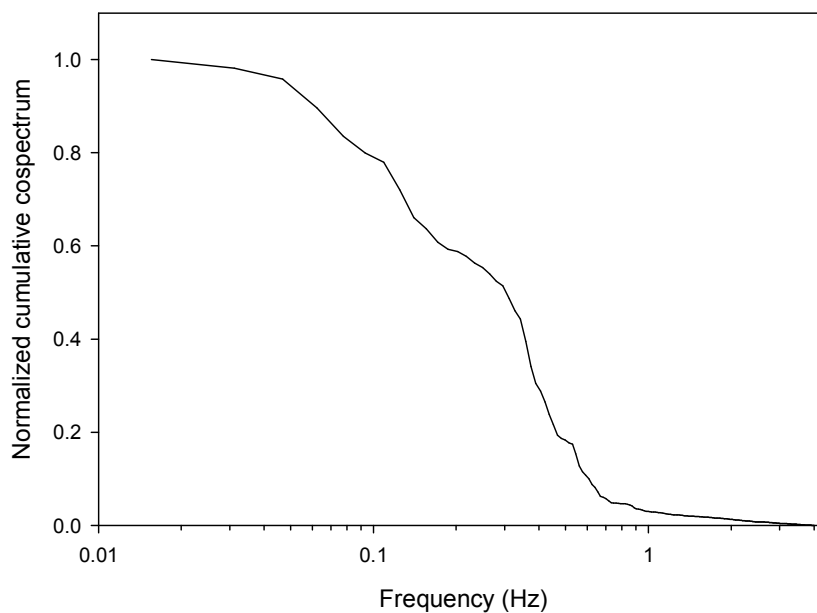


Figure G.16. Normalized cumulative cospectrum of w' and C' for Kittery tidal flow burst, block 19140-20532.

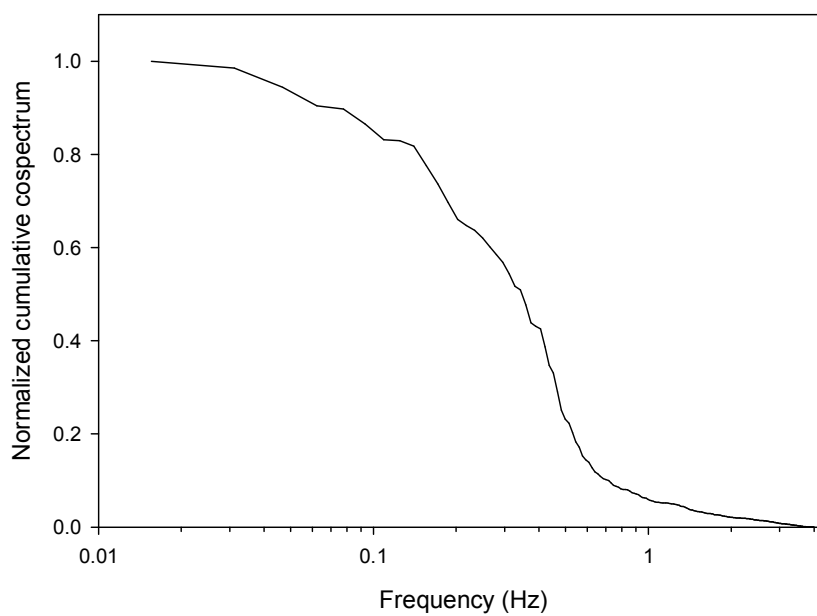


Figure G.17. Normalized cumulative cospectrum of w' and C' for Kittery tidal flow burst, block 20532-21924.

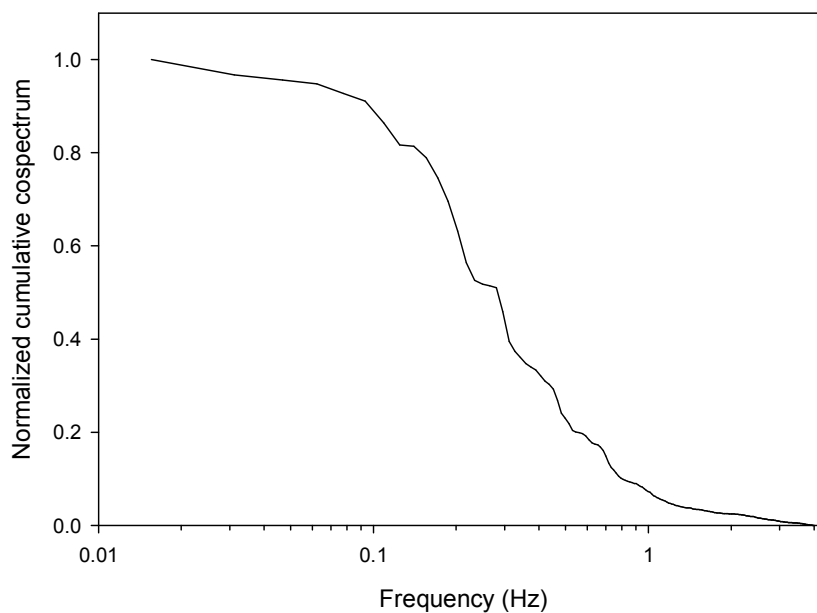


Figure G.18. Normalized cumulative cospectrum of w' and C' for Kittery tidal flow burst, block 21924-23316.

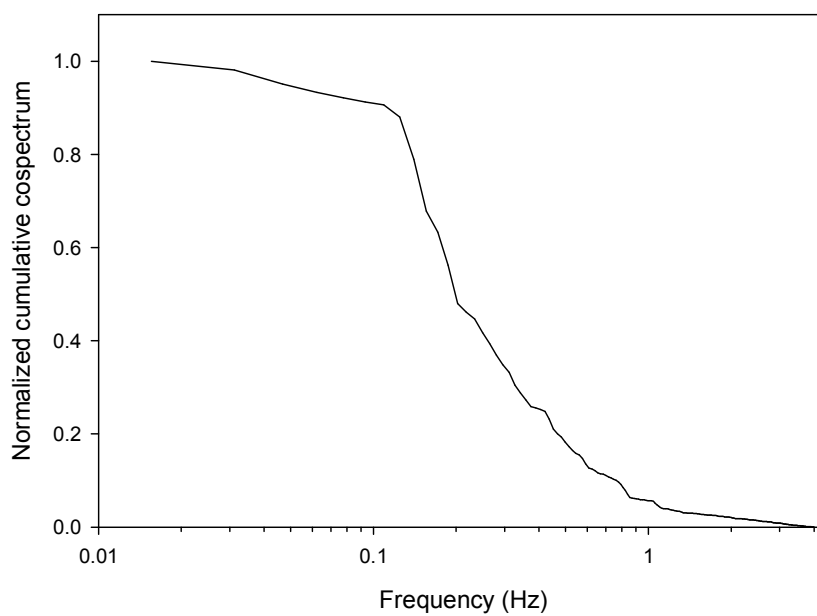


Figure G.19. Normalized cumulative cospectrum of w' and C' for Kittery tidal flow burst, block 23316-24708.

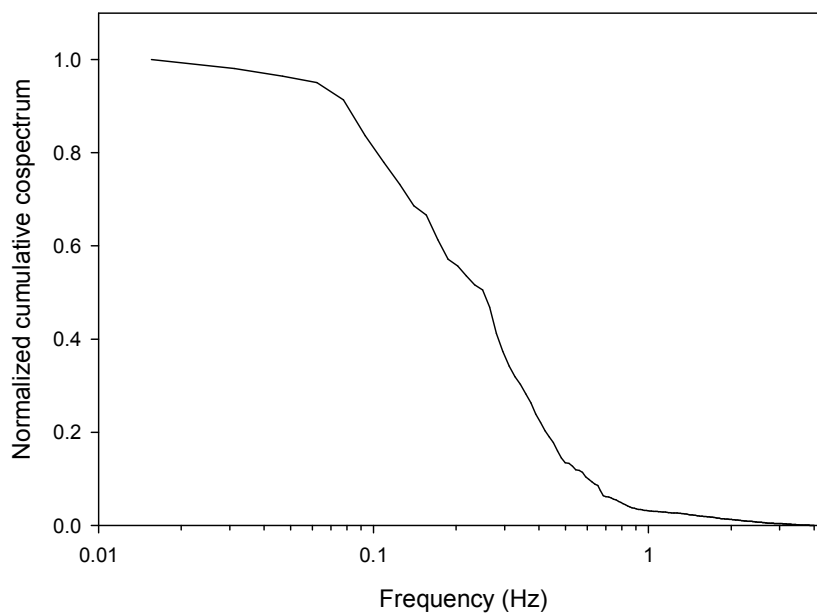


Figure G.20. Normalized cumulative cospectrum of w' and C' for Kittery tidal flow burst, block 24708-26100.

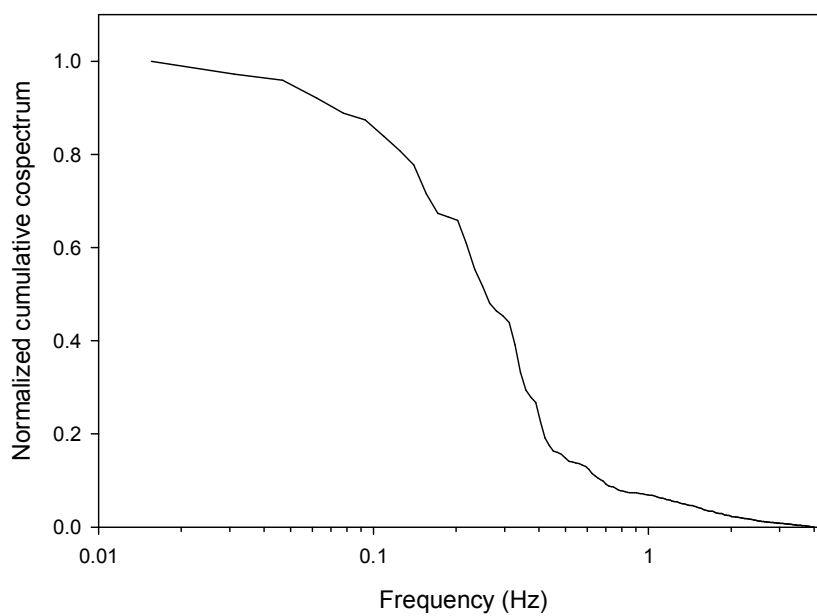


Figure G.21. Normalized cumulative cospectrum of w' and C' for Kittery tidal flow burst, block 26100-27492.

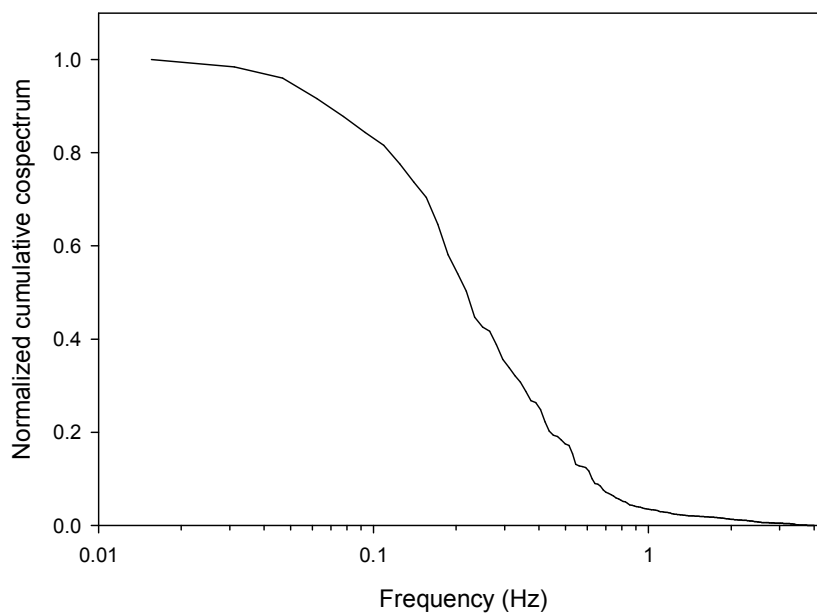


Figure G.22. Normalized cumulative cospectrum of w' and C' for Kittery tidal flow burst, block 27492-28884.

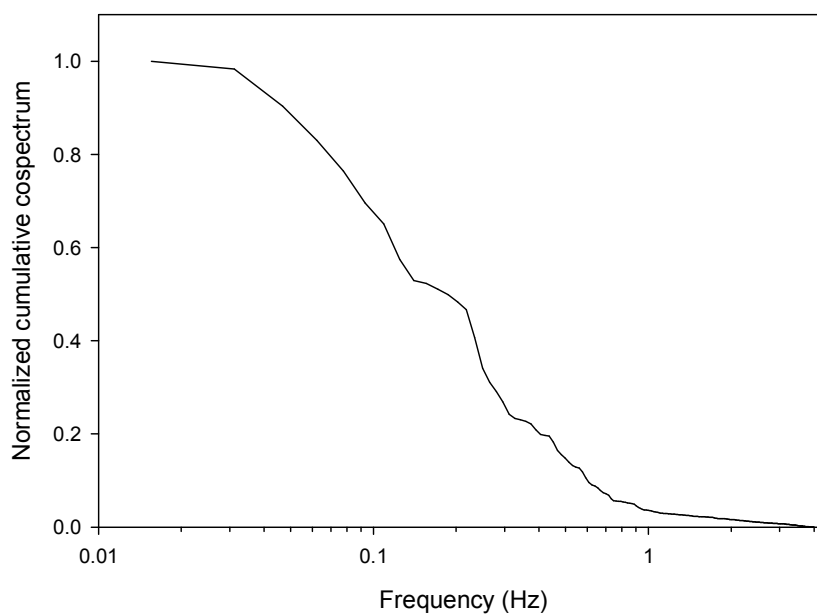


Figure G.23. Normalized cumulative cospectrum of w' and C' for Kittery tidal flow burst, block 28884-30276.

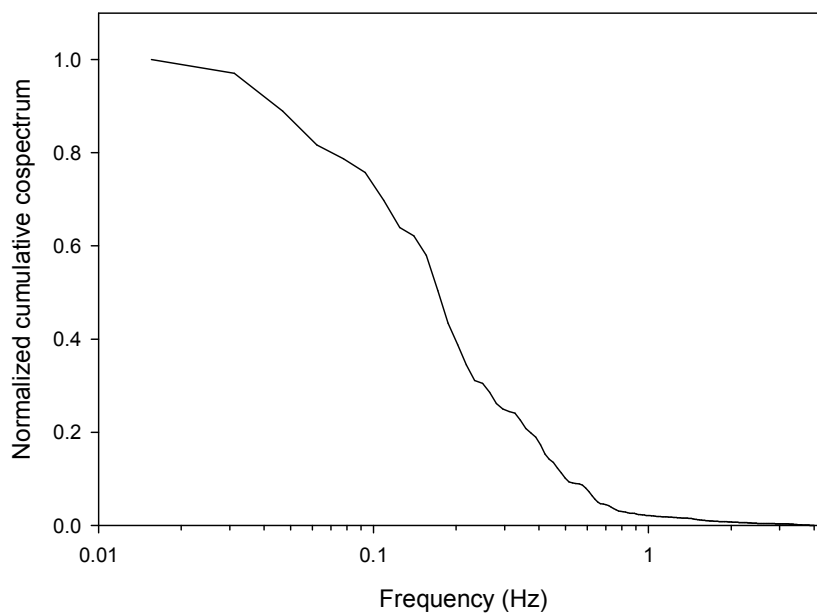


Figure G.24. Normalized cumulative cospectrum of w' and C' for Kittery tidal flow burst, block 30276-31668.

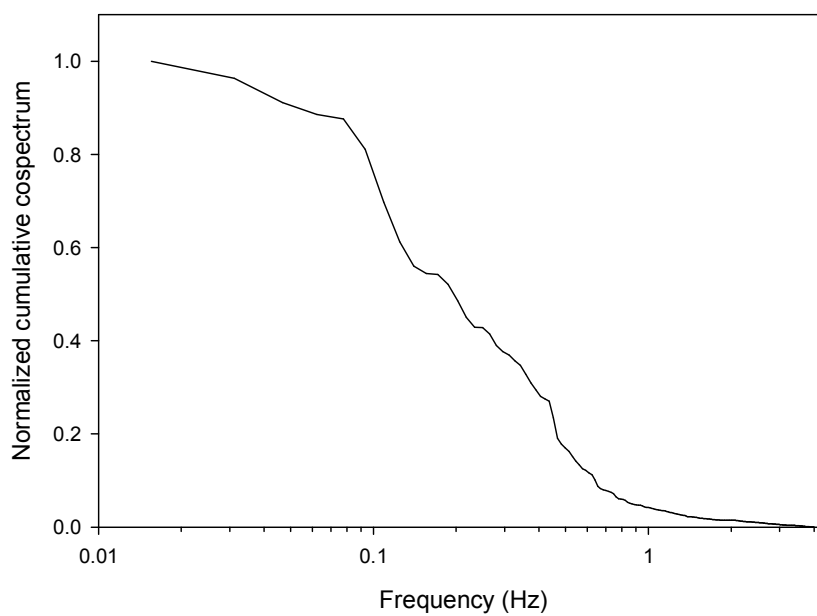


Figure G.25. Normalized cumulative cospectrum of w' and C' for Kittery tidal flow burst, block 31688-33060.

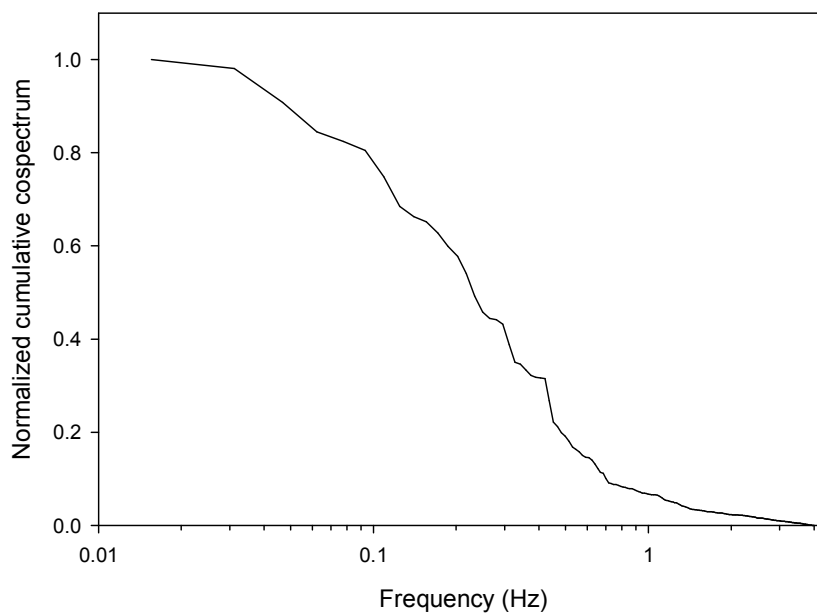


Figure G.26. Normalized cumulative cospectrum of w' and C' for Kittery tidal flow burst, block 33060-34452.

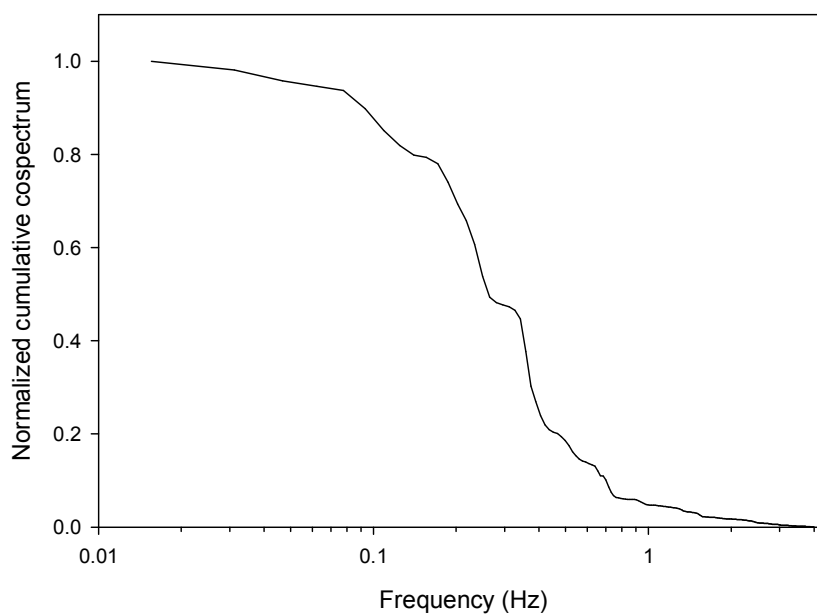


Figure G.27. Normalized cumulative cospectrum of w' and C' for Kittery tidal flow burst, block 34452-35844.

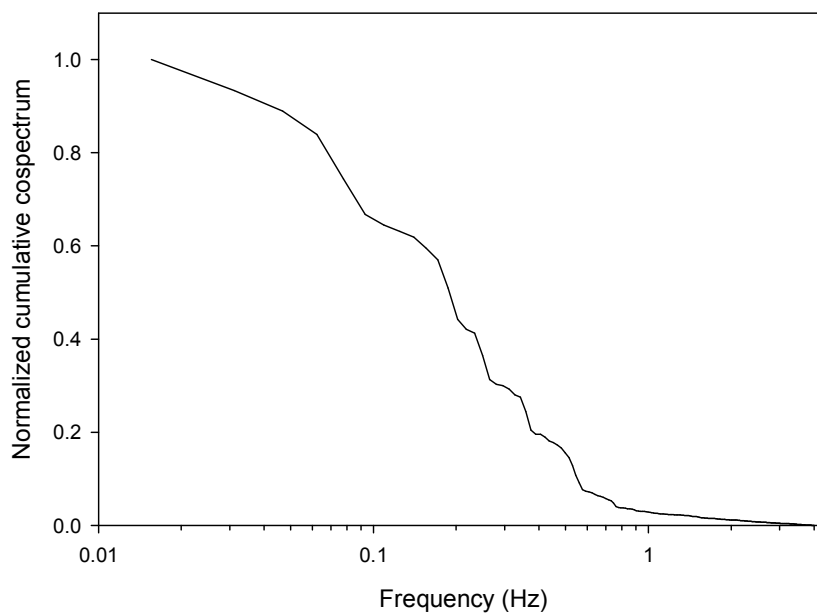


Figure G.28. Normalized cumulative cospectrum of w' and C' for Kittery tidal ebb burst, block 128348-131044.

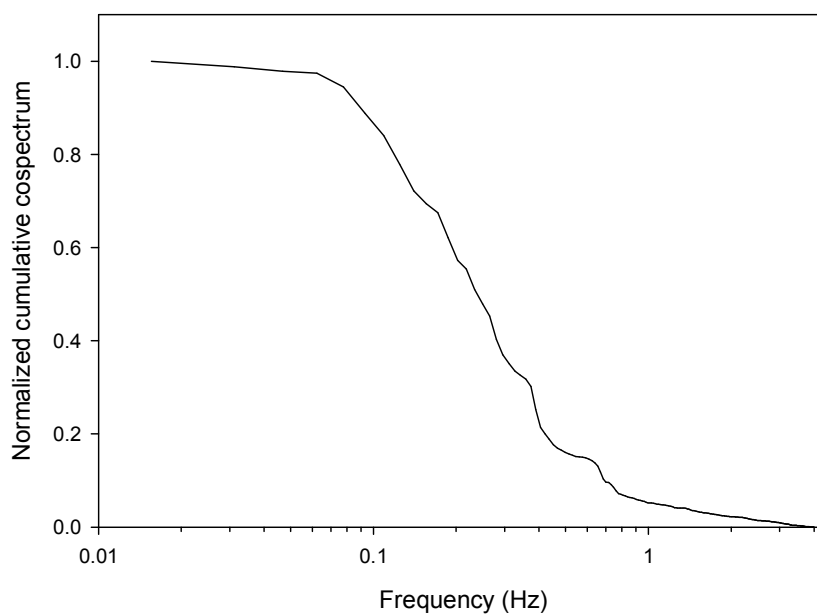


Figure G.29. Normalized cumulative cospectrum of w' and C' for Kittery tidal ebb burst, block 131044-133740.

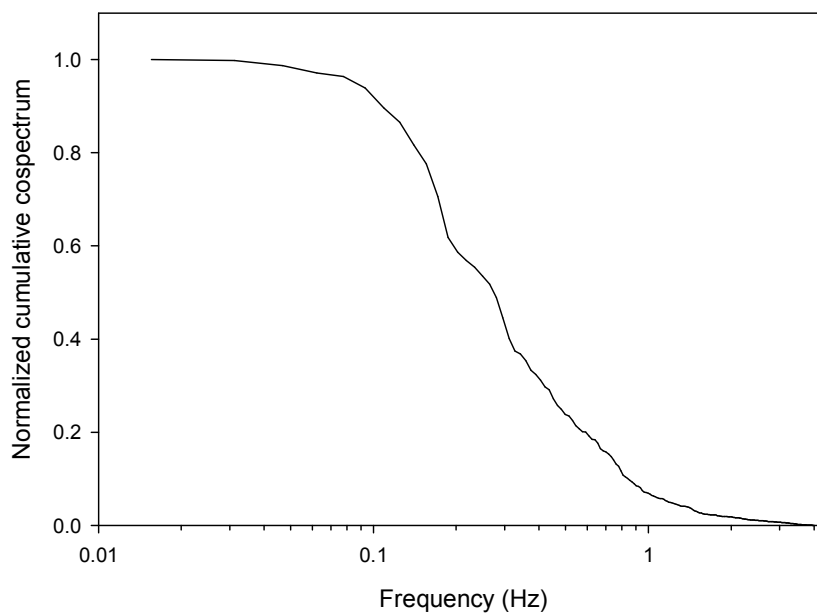


Figure G.30. Normalized cumulative cospectrum of w' and C' for Kittery tidal ebb burst, block 133740-136436.

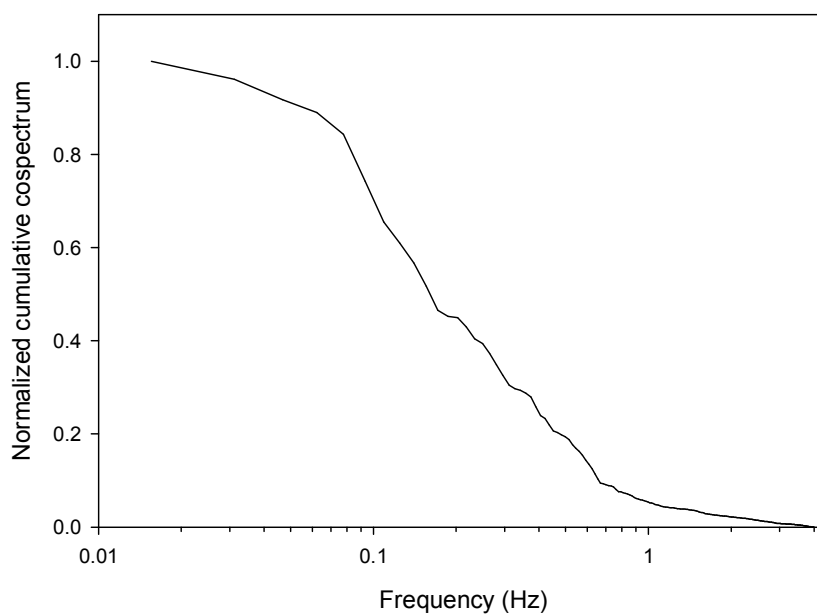


Figure G.31. Normalized cumulative cospectrum of w' and C' for Kittery tidal ebb burst, block 136436-139132.

BIOGRAPHY OF THE AUTHOR

Michael Swett was born in Bangor, Maine on August 26, 1986. He was raised in Old Town and graduated from Old Town High School in 2004. He attended The University of Maine and graduated in 2008 with a Bachelor of Science degree in Civil Engineering. Following completion of his undergraduate education, Michael enrolled in graduate studies in Civil Engineering at The University of Maine, with a focus in environmental engineering.

In May, 2010, Michael will begin work as a consulting engineer for Wright-Pierce in their Topsham, Maine office. Michael is a candidate for the Master of Science degree in Civil Engineering from The University of Maine in May, 2010.